August 2019

Sedimentological and Geochemical Analysis of Deep-Water Deposits in the Mojón De Hierro Formation at Arroyo Garrido, Tepuel-Genoa Basin, Patagonia, Argentina

Natalie Beatrice McNall
University of Wisconsin-Milwaukee

SEDIMENTOLOGICAL AND GEOCHEMICAL ANALYSIS OF DEEP-WATER DEPOSITS IN THE MOJÓN DE HIERRO FORMATION AT ARROYO GARRIDO, TEPUEL-GENOA BASIN, PATAGONIA, ARGENTINA

by

Natalie Beatrice McNall

A Thesis Submitted in

Partial Fulfillment of the

Requirements for the Degree of

Master of Science

in Geosciences

at

The University of Wisconsin-Milwaukee

August 2019

ABSTRACT

SEDIMENTOLOGICAL AND GEOCHEMICAL ANALYSIS OF DEEP-WATER DEPOSITS IN THE MOJÓN DE HIERRO FORMATION AT ARROYO GARRIDO, TEPUEL-GENOA BASIN, PATAGONIA, ARGENTINA

by

Natalie Beatrice McNall

The University of Wisconsin-Milwaukee, 2019
Under the Supervision of Professor Dr. John Isbell

The Earth has had multiple Phanerozoic glacial intervals but the Late Paleozoic Ice Age (LPIA) was its longest and most extensive, lasting from the Late Devonian (~372 Ma) until the Late Permian (~254 Ma). The LPIA is the last complete climate shift from a greenhouse to icehouse and back to a greenhouse state and the only one to occur on a biologically complex Earth. Therefore, it provides perspectives on deep-time climatic transitions, the parameters controlling them, and the Earth's physical, chemical and biological responses to such climate changes. Research on mid to high-latitude deposits in Gondwana provides evidence that the LPIA had a highly dynamic climate, with multiple ice sheets and ice caps, that fluctuated asynchronously and diachronously across the supercontinent as it drifted across the paleo South Pole. Numerous questions remain on the spatial and temporal extent of the ice centers, the timing of expansion and contraction of the ice sheets and the distribution of ice across Gondwana through time. The Tepuel-Genoa Basin, in Patagonia, Argentina, was situated within the paleo South Polar Circle as part of Gondwana and contains a nearly continuous sedimentary succession of Carboniferous to Lower Permian strata. The Mojón de Hierro Formation has been described as both non-glacial and glacial

in origin. This study investigates a unit within the Mojón de Hierro Formation which was used in a detrital zircon analysis which implies a large ice sheet covered the basin at the time of deposition, which extended from an ice center in the Ellsworth Mountains all the way to the Panthalassan Margin in west-central Gondwana. These strata contain mudrocks, some with outsized clasts, diamictites and sandstones. Five stratigraphic sections were measured at Arroyo Garrido and the strata were categorized into five lithofacies associations; 1) laminated mudrock, 2) laminated mudrock with dispersed clasts, 3) graded rhythmites, 4) laminated and bedded diamictites, and 5) deformed bedded sandstones. The strata were deposited in a basinal slope environment from suspension settling, ice rafted debris, sediment gravity flows and mass transport complexes. The mass transport complexes were deposited on a lower slope and formed deep-water topography that resulted in a ponded mini basin behind the sand blocks. Paleo-flow is indicated as flowing to the northwest. The Chemical Index of Alteration (CIA) indicates average marine shale values and that muds are of temperate terrestrial sediment sources. A glacial source could not be substantiated using CIA values. Vanadium/chromium ratios indicate dysoxic values in samples between the mass transport sand blocks and oxic values in samples above the filled ponded mini basin. The detailed facies analysis and geochemistry data do not indicate the Arroyo Garrido strata to be of glacial origin. However, facies analysis data suggest that icebergs from a distant source transited the basin during emplacement of the mass transport and sediment gravity flow deposits.

To

my great grandparents, Alice & Webster McNall

my grandparents, Michael & Carolyn McNall

my parents, Michael & Janet McNall

and my sister, Alyssa McNall

TABLE OF CONTENTS

LIST OF FIGURES

LIST OF TABLES

ACKNOWLEDGMENTS

I owe my deepest gratitude to my advisor, Dr. John Isbell, for his infinite support, guidance and encouragement. This research and thesis would not have been possible without his help. It is hard for me to put into words how grateful I am for the help and time he invested in me. He continuously motivated me as an undergraduate and graduate student and taught me to aim high and never give up. He has inspired me that in taking the road less traveled by, all the difference is made. I thank him for creating the scientist within me today. I would also like to thank my committee members, Dr. Mark Harris and Dr. Lindsay McHenry, for their knowledge, suggestions, support and time.

I would like to express gratitude to the UW-Milwaukee Graduate School for offering me the Advanced Opportunity Program Fellowship which provided the opportunity and funding to receive my Master's degree. I would also like to thank the UWM Geosciences Department for their educational support and an extra thanks to Dr. Lindsay McHenry for allowing me to use her geochemistry lab in the department, making this project possible. Thank you to Kate, Kodi and Chase for their help with the department's equipment and result interpretations, and Libby and Scott for help in the field.

Thank you to our many Argentine colleagues, the Museum of Paleontology Egidio Feruglio (MEF) and especially Dr. Alejandra Pagani, for their time, guidance, knowledge, support and for making the Patagonian terrane accessible. A special thanks is in debt to Dr. Arturo Taboada for finding the research site, Arroyo Garrido, on his bicycle all those many eons ago. I would also like to thank Carina, Cesar and Christian for their knowledge of Patagonia, helping me practice my Spanish and for the great memories made in Argentina.

Finally, I would like to thank my great grandparents, Alice and Web, for igniting my life long creative and geologic passions through turquoise jewelry and little tumbled stones. Thank you, grandma and grandpa, Carol and Mike, for setting the best example of how hard work, diligence and being humble pays off and for providing me every mean necessary to strive academically and in life. You two have taught me more than you know. Also thank you, mom and dad, Janet and Mike, for loving, supporting and creating me. And thank you to my sister and life-long best friend, Alyssa, for always inspiring me to be more creative, for being by my side when I collect rocks on our adventures and helping me grow to become the person I am today.

This work was supported by grants from the National Science Foundation (1443557, 1559231, and 1729219), and a grant from the Nelson-Cherkauer-Lasca Legacy Summer Research Fellowship administered through the Department of Geosciences at the University of Wisconsin-Milwaukee. Support and field equipment was accessible through the Museum of Paleontology Egidio Feruglio (MEF) and National University of Patagonia San Juan Bosco (UNPSJB) prepared and managed by Alejandra Pagani and Arturo Taboada.

"For a billion years the patient Earth amassed documents and inscribed them with signs and pictures which lay unnoticed and unused. Today, at last, they are waking up, because man [and woman] has come to rouse them. Stones have begun to speak, because an ear is there to hear them. Layers become history and, released from the enchanted sleep of eternity, life's motley, never-ending dance rises out of the black depths of the past into the light of the present."

-Hans Cloos

1. INTRODUCTION

Multiple glacial intervals have occurred throughout the Phanerozoic, however, the Late Paleozoic Ice Age (LPIA) and the current Cenozoic Ice Age are arguably the most significant. The LPIA was Earth's longest and most extensive, lasting from Late Devonian to Late Permian (~372 Ma to ~254 Ma). It was also the last complete climate shift from a greenhouse to icehouse and back to greenhouse state and the only example on a biologically complex Earth, providing a deep-time perspective on climatic transitions. Studying it can lead to a better understanding of the parameters controlling these transitions and the current transition out of the Cenozoic Icehouse.

Similarities between the LPIA and the Cenozoic Ice Age include; 1) a long duration, 2) that both occur/occurred on a biologically complex Earth, and 3) that both occur/occurred during times of low CO_2 levels in the atmosphere. However, the two also have major differences such as; 1) intensities in solar luminosity, 2) O_2 levels in the atmosphere, 3) different biotas, 4) different continental positioning (the majority of the landmass positioned in the southern hemisphere during the LPIA versus its current, more evenly distributed position around the planet), and 5) ocean circulation patterns. The LPIA cannot be thought of as an exact analogue to present day climatic transitions, but it is the most applicable glacial interval to our current climate state (Gastaldo, 1996; Soreghan, 2004; Isbell et al., 2003, 2008, 2012; Fielding, 2008a; Montañez & Poulsen, 2013), which offers insight on how the Earth's physical, chemical and biological systems respond to climatic transitions.

Traditional interpretations of the LPIA consist of a single massive ice sheet centered near the paleo South Pole covering and spreading out across the majority of the supercontinent Gondwana (Figure 1; A) for over 100 million years, from ~372 Ma to ~254 Ma (Veevers & Powell,

1987; Scotese and Barrett, 1990; Ziegler et al., 1997; Scotese, 1997, 2014). In this scenario, the ice sheet advanced and retreated outward across the polar regions extending across much of the supercontinent during maximum glaciation and nearly disappearing during ice minimal or non-glacial intervals. Such ice volume fluctuations were used to explain hypothetical changes in eustacy of 100-200 m, which were thought to be required for the formation of equatorial cyclothems (Veveers & Powell, 1987; Heckel, 1994). Such glacial- non-glacial intervals were thought to have resulted from changing insolation conditions due to Milankovitch cycles (Wanless & Shepard, 1936; Heckel, 1994).

Recent climate modeling indicates that large scale ice sheets of this size are highly stable and unlikely to fluctuate with orbitally induced changes in solar insolation (Deconto & Pollard, 2003; Horton & Poulsen, 2009). Additionally, recent research in Antarctica, Australia, Southern Africa, India, the Arabian Peninsula and southern South America on mid to high-latitude deposits in Gondwana provide evidence that the LPIA had a highly dynamic climate. These dynamics are characterized by a succession of shorter (~1 to 8 Ma) glacial intervals, occurring at different times, which were separated by non-glacial intervals of the same duration (Caputo & Crowell, 1985; Lopez-Gamundi, 1987, 1994, 1997, 2010; Visser, 1987, 1997; Isbell et al., 2003, 2008, 2012; Caputo et al., 2008; Fielding et al., 2008a, 2008b; Issacson et al., 2008; Montanez & Poulsen, 2013).

These more recent interpretations characterize the LPIA as composed of multiple, smaller ice sheets and ice caps (Figure 1; B), fluctuating asynchronously and diachronously as Gondwana drifted across the late Paleozoic South Pole (Caputo & Crowell, 1985; Crowell & Frakes, 1970; Lopez-Gamundi, 1997; Isbell et al., 2003). Subsequently, these smaller ice sheets represent less ice volume than previously estimated (Fielding et al., 2008; Isbell et al., 2003, 2010, 2012).

Because ice behaves as a Bingham plastic and flows under high stress (>40 m thick weight), it is physically impossible to have thick ice masses with small areal footprints. Therefore, to cover the same area of Gondwana with smaller ice sheets results in less ice volume (Crowley & Baum, 1991; Isbell et al., 2003).

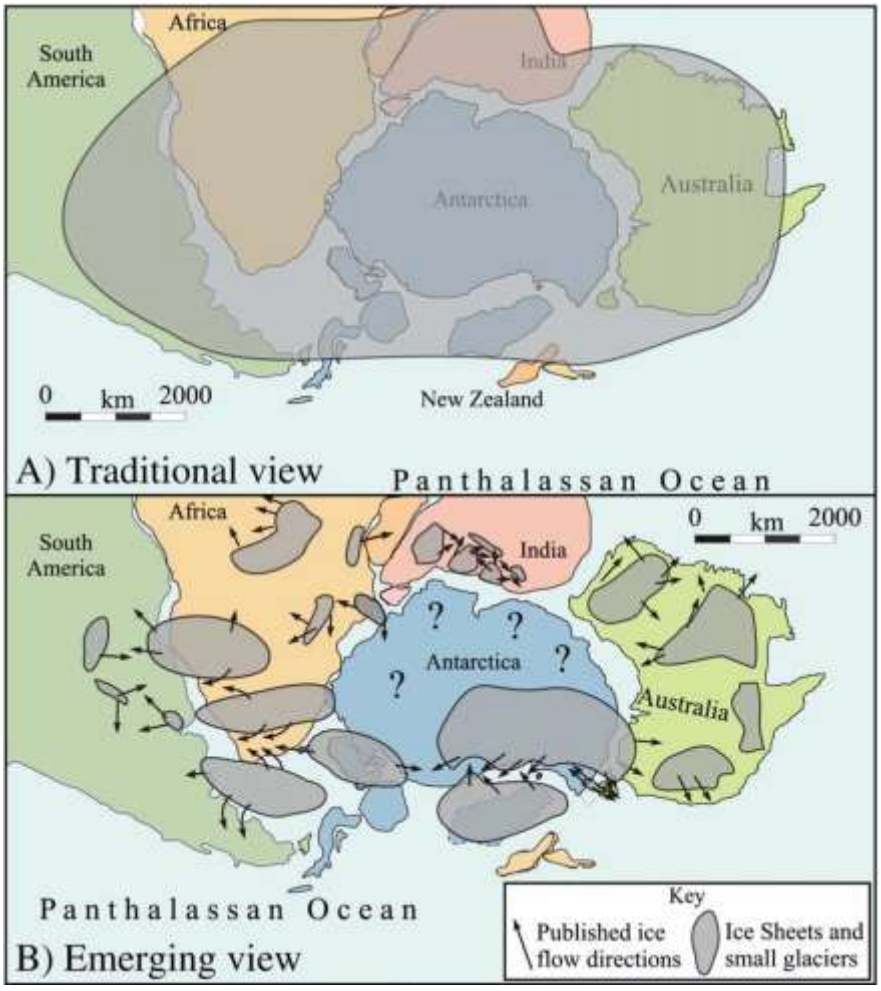

Figure 1 Traditional and recent reconstructions of maximum glaciation during the Late Paleozoic Ice Age. A) Traditional reconstruction showing a massive ice sheet covering much of southern Gondwana. Ice sheets were from Isbell et al. (2012) and modified from Scotese (1997) and Scotese and Barrett (1990). B) Reconstruction of Gondwana during maximum glaciation during the Gzhelian to early Sakmarian (Pennsylvanian–Early Permian) based on recent data and ice flow directions. Ice flow directions are from Frakes et al. (1975); Hand (1993); Veevers and Tewari (1995); López-Gamundí (1997); Visser (1997a, 1997b); Visser et al. (1997); Fielding et al. (2008a); Isbell et al. (2008c); Mory et al. (2008); Rocha-Campos et al. (2008); & Isbell (2010). Modified from Isbell et al. (2012).

Despite ongoing research efforts using the rock record to better understand LPIA glaciation in Gondwana, numerous questions remain. These include; 1) the number of glacial events, 2) the spatial and temporal extent of ice centers, 3) the timing of ice sheet advances and retreats, 4) the distribution of ice across Gondwana through time, and 5) the controlling mechanisms of the initiation, duration and completion of the glacial intervals. Therefore, more detailed investigations of mid and high-latitude LPIA basins and deposits will help to constrain these questions and provide answers on ice volume and the relationships between glaciation, sea level changes, climate, and depositional systems. Understanding the nature of deep-time environmental change will help scientists to constrain the parameters of how and when the Earth's paleoclimate shifted from icehouse to greenhouse states, which may aid in understanding the parameters of the current Cenozoic climate change since the LPIA is the closest analogue (Gastaldo, 1996; Soreghan, 2004; Fielding, 2008; Isbell et al., 2003, 2008, 2012; Montanez & Poulsen, 2013).

Located within Patagonia, the Tepuel-Genoa Basin (present day Chubut Province, Argentina; Figure 2) was positioned within the paleo South Polar Circle (>66° S) during the Late Carboniferous to Early Permian (Figure 3) (Scotese & Barrett, 1990; Scotese, 1997; Lawver et al., 2008) and documents a thick succession with a nearly continuous marine and glaciomarine stratigraphic record (Pagani, Taboada & Puerta, 2010). Therefore, the deposits document the changing environmental conditions in polar Gondwana during the LPIA and thus record the different glacial intervals as well as the transitions from glacial to non-glacial climatic conditions (arid and semi-arid conditions) during this time in this region (Limarino & Spaletti, 2006; Pagani, et al., 2010).

The Tepuel-Genoa Basin contains diamictites previously interpreted as glacial tills (Suero, 1958; Frakes, 1969; Page et al., 1984; Pagani & Taboada, 2010). The Mojón de Hierro Formation,

one of several formations within the basin, has been interpreted as both non-glacial (Suero, 1958; Page, 1984) and glacial (Pagani & Taboada, 2010; Griffis et al., 2018) in origin. Recently, a paper using detrital zircon analysis on a single sample and single paleocurrent orientation measurement taken from the underlying Pampa de Tepuel Formation (González-Bonorino, 1992; Griffis et al., 2018), concluded that ice streams from an Antarctic ice center fed sediment and ice into the Tepuel-Genoa Basin during deposition of the Mojón de Hierro Formation (Figure 4) and infers that ice extended to the Panthalassan Margin in west-central Gondwana during the Early Permian. All of these conflicting studies provide sweeping interpretations of the climatic history of Patagonia and a portion of Polar Gondwana without a single detailed sedimentological analysis of these strata. Therefore, clarification and an in-depth analysis provided by this thesis will test these diametrically opposed interpretations within this important sedimentary basin.

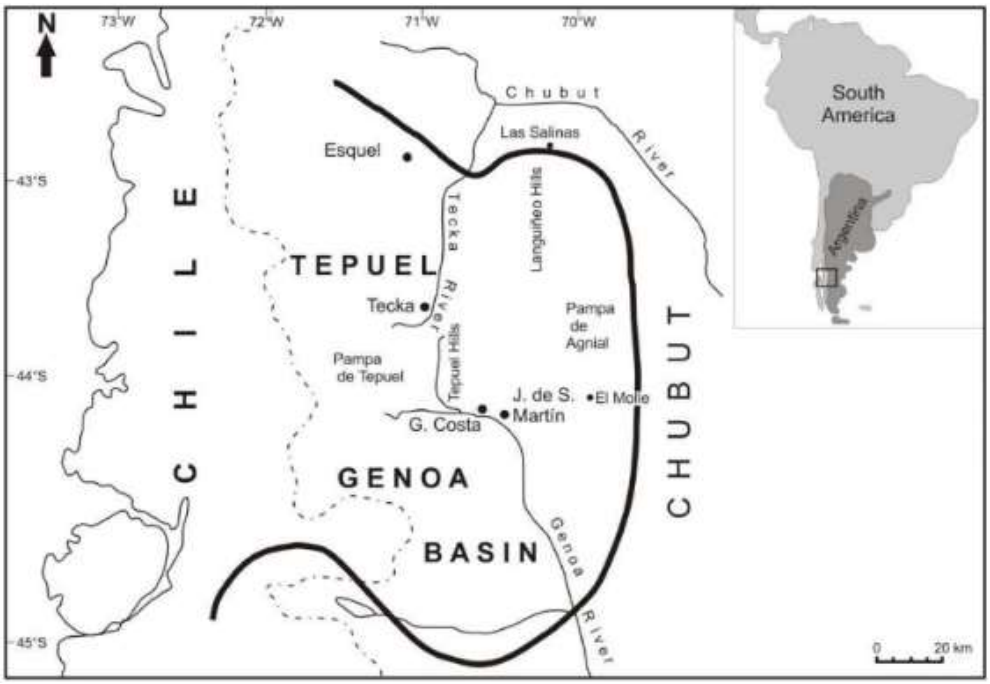

Figure 2 The present-day location of the Tepuel-Genoa Basin within southern Argentina (image modified from Gonzalez, 1997).

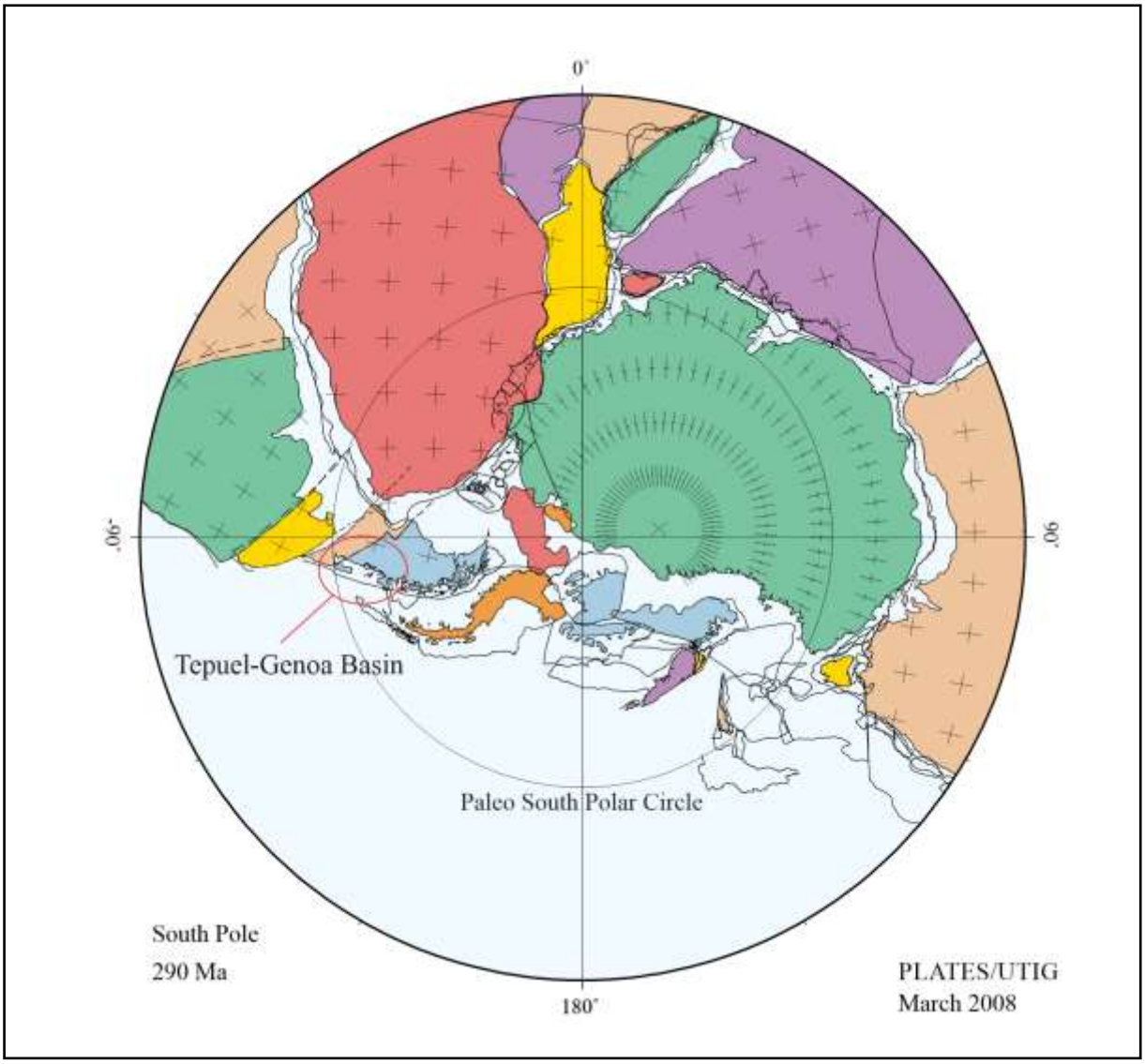

Figure 3 The paleo-continental positioning of the southern hemisphere during ~290 Ma and location of the Tepuel-Genoa Basin (circled in red) located in Patagonia within the paleo South Polar Circle (modified from Lawver et al., 2008, UTIG plates Project).

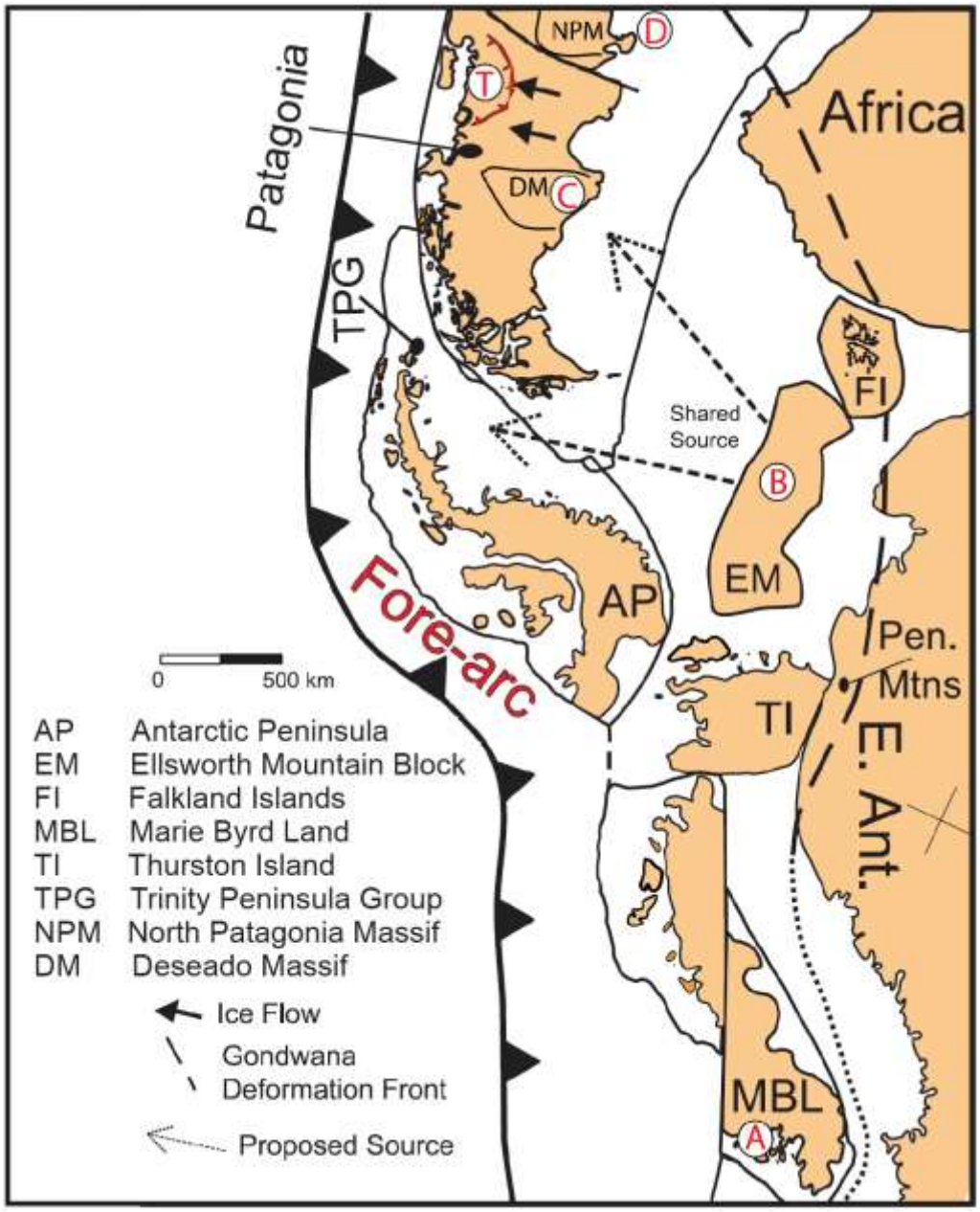

Figure 4 Hypothesized source terrain of Griffis et al. (2018) for the Mojón de Hierro Formation, proposing that recycled Ellsworth Mountain sediment provided a source of zircon to the Tepuel (labelled 'T' on figure) and Trinity Peninsula groups (TPG) based on similar age distributions and highly evolved Hf isotopic compositions (Griffis et al., 2018). Solid black arrows interpreted ice-flow direction (González-Bonorino, 1992). On the figure: A-Marie Byrd Land, B-Ellsworth Mountains, C-Deseado Massif, D-North Patagonia Massif, and T- Tepuel-Genoa Basin (modified from Griffis et al., 2018, originally from Elliot et al., 2016).

2. GEOCHEMISTRY BACKGROUND

Various geochemical signatures can serve as proxies for paleoclimatic and paleoenvironmental conditions and changes in the provenance at the time of deposition. Using geochemical analyses and established proxies provides valuable information about depositional conditions that offers additional information above and beyond facies analysis alone. Bulk mineralogy is obtained from X-ray diffraction (XRD) analysis, while elemental data including major, minor and trace element data are obtained from X-ray fluorescence (XRF) spectrometry.

Shales best represent the average crustal composition of the provenance area (McCulloch & Wasserburg, 1978; Lee, 2009) because they are the most dominant detrital sediments in basins (Pettijohhn, 1975). The geochemical composition of shales can provide information on weathering conditions of the source sediment area (Roser & Korsch, 1988; McLennan, 1993; Lee, 2009). The concentration of immobile and mobile elements in shales can help determine the contribution of acidic (felsic) or basic (mafic) sources, due to enrichments and depletions in specific elements (Roser & Korsch, 1988) when compared to Post-Archean Average Shale (PAAS; Taylor & McLennan, 1985) and Upper Continental Crust (UCC; Taylor & McLennan, 1985) (PAAS and UCC data can be seen in Table 4). Geochemical signatures have been used in a number of ways to interpret paleo-depositional conditions (Jones & Manning, 1994; Dobrzinski et al., 2004).

Climate is a major factor in the degree of weathering and the breakdown of rocks. Past climatic conditions, therefore, can be estimated from past weathering products. Reworked siliciclastic materials deposited in marine settings reveal information on weathering conditions and climate (Bahlburg & Dobrzinski, 2011). The Chemical Index of Alteration (CIA) is a well-established and frequently used proxy for determining changing climatic conditions by determining the degree of alteration of feldspars to form clay minerals, because the amount of

mechanical and chemical weathering is different in arid (polar) versus humid (tropical) environments (Nesbitt & Young, 1982). This is because physical weathering just breaks sediment into smaller pieces without changing the composition. Chemical weathering, on the other hand, alters the sediment's composition as weathering occurs. Trace elemental data provided by XRF using the elements vanadium and chromium (V & Cr) are used to estimate paleo-oxygen levels and paleo-redox conditions in the water column.

The Chemical Index of Alteration was first introduced as a sensitive measure of the degree of chemical weathering in clastic sediments. Young and Nesbitt (1982) formulated the equation: CIA = (Al_2O_3/ Al_2O_3 + CaO* + Na_2O + K_2O) x 100 (where CaO* represents the calcium content within silicate minerals). Chemical weathering increases proportionately in humid conditions, with the leaching of alkalis (Na^+ and K^+) and Ca^+ and the concentration of Al and Si in the residue (Ding, 2016). Progressive chemical weathering using CIA is normally measured over a range of values from 1-100, with low CIA values for sediments containing fresh feldspars with little to no chemical weathering and high values for clay produced under tropical conditions. Environments where abrasion and mechanical breakage dominates over chemical weathering in sedimentary rocks, such as arid and glacial settings, have average values for CIA ranging between 50-70 (Goldberg & Humayun, 2010), while shales produced in more humid and tropical settings have CIA values of 80-100. Average values for marine shales range from 70-75 (Taylor & McLennan, 1985; Goldberg & Humayun, 2010). This ultimately represents the aridity/humidity conditions of the rocks exposed in the source area and can thus aid in determining the climatic setting of the drainage basin.

In addition to the CIA, other geochemical parameters have been applied to interpret the paleoenvironment and paleo-oxygenation (Ernst, 1970; Jones & Manning, 1994; Fedo; 1995;

Dobrzinski et al., 2004). These geochemical analyses involve trace elements, particularly vanadium (V) and chromium (Cr), and address the oxygen levels in the water column at the time of deposition. An index for paleo-oxygenation levels can be determined from mudrock by using the ratios of these specific trace elements, V/Cr (Ernst, 1970; Jones & Manning, 1994, Henry et al., 2010). Jones and Manning (1994), explain that chromium is incorporated within the detrital clastic fraction of sediments where it can be substituted for aluminum in clays, absorbed, or occurs as chromite (Patterson et al., 1986). The trace element vanadium can be bound to organic matter (by the incorporation of V^{4+} into porphyrins) and becomes concentrated in sediments under reducing water conditions (Shaw et al., 1990). It can also be physically bound to detrital silicate minerals. V/Cr ratios less than 2 indicate oxygen-rich waters with H_2S present in the bottom waters just above the sediment substrate. Ratios ranging from 2 to 4.25 indicate dysoxic waters, and values greater than 4.25 indicate suboxic and anoxic water conditions (Jones & Manning, 1994).

Regionally, this geochemical data will constrain paleo-weathering in the source area and paleo-oxygentation conditions in the bottom waters during deposition, and they ultimately help reconstruct the paleoenvironment. There are very few bulk mineralogical and geochemical (e.g. XRD and XRF) analyses on LPIA sedimentary rocks in the literature (Scheffler et al., 2003, 2006; Henry et al., 2010, Pauls et al., 2018), despite their usefulness and quantitative approach to analyzing glacial and non-glacial sediments, depositional environments and paleoclimate. Using XRD and XRF on LPIA sediments helps to investigate aspects of the deposits that are unknown or unseen with traditional sedimentological methods that and will ultimately help constrain glacial intervals and localities in deep-time.

3. RESEARCH OBJECTIVES

The objective of this research project is to identify mid to high-latitude depositional environments in the Mojón de Hierro Formation of the Tepuel-Genoa Basin during the Late Paleozoic Ice Age. This study will test the hypotheses of glacial versus non-glacial deposition and develop a picture of the ice age as documented within the rock record and elucidate how influential ice sheets were to deposition in the basin during the Early Permian by providing a detailed sedimentologic analysis of the exposed deposits at Arroyo Garrido. Mineralogy and geochemistry, using X-ray diffraction (XRD) and X-ray fluorescence (XRF) spectrometry will aid in determining the paleoclimatic conditions of the sediment source area and paleo-oxygenation in the water column. Therefore, this study will facilitate reconstruction of depositional settings and climate records within a portion of Polar Gondwana. Specific research objectives include;

1. Reconstructing the depositional environments to test the two conflicting hypotheses on the depositional setting of the Mojón de Hierro Formation in the Tepuel-Genoa Basin. Determine if the setting was glacial versus non-glacial, glacially influenced versus normal marine, and/or shallow versus deep-marine. A detailed sedimentological facies analysis was conducted to determine the depositional setting and to reconstruct the paleoenvironments. In turn, this will aid in determining the climatic conditions in the depositional basin and in this portion of Polar Gondwana.

2. Determine paleo-slope orientation and sediment delivery pathways for sediment deposited at Arroyo Garrido and to test the source terrain hypothesis of an ice sheet delivering sediment to the basin derived from the Ellsworth Mountains, Antarctica (Griffis et al., 2018).

3. Provide a bulk mineralogical and geochemical analysis using X-ray diffraction and X-ray fluorescence spectrometry, and apply the data to paleoclimate/paleo-weathering and paleo-oxygenation proxies. This data will aid in constraining basin conditions and determining the climatic signature within the rocks and help determine if there were potential glaciers nearby.

This research project contributes to addressing glaciation questions on a regional scale during the LPIA. It also contributes to developing an understanding of the LPIA by: enhancing the resolution on the size, timing and location of Gondwanan ice sheets to advance deep-time climate change studies and to improve knowledge on the understanding of the parameters that control and effect icehouse and greenhouse transitions.

4. GEOLOGIC SETTING & STUDY AREA

Two conflicting hypotheses have been proposed for the paleogeography of Patagonia during the late Paleozoic and its relationship to the rest of South America. These two hypotheses are (1) it formed as an autochthonous block connected to South America within Gondwana (Forysthe, 1982; Dalla Salda et al., 1990; Pankurst et al., 2006) while the other hypothesis, (2) suggests that it was an allochthonous crustal block that collided with the southern margin of South America in the late Paleozoic (Figure 5) (Ramos, 1984, 1986, 1988; Ramos et al., 2004). Ramos (2008), proposed the occurrence of two magmatic arcs; a western belt (active from the Devonian to mid-Carboniferous) and a northern belt that was partially coeval (Late Permian; Figure 6) with Patagonia's collision with the southwestern margin of Gondwana. When the Antarctic Peninsula collided with the Patagonian terrane, activity in the western magmatic arc ceased (Ramos, 2008).

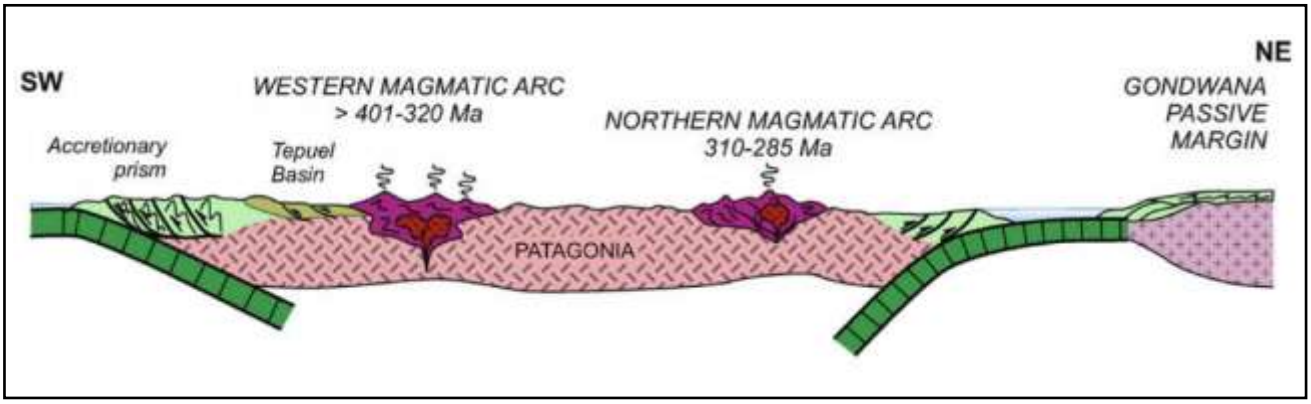

Figure 5 An oblique schematic structural cross section of Patagonia during the late Paleozoic, showing the northern magmatic belt (right; 310-285 Ma) and western magmatic belt (left; >401-320 Ma) under subduction and their relationship to the Tepuel-Genoa Basin (modified from Ramos, 2008). Ramos (2008) presents the basin in this figure as an autochthonous crustal block.

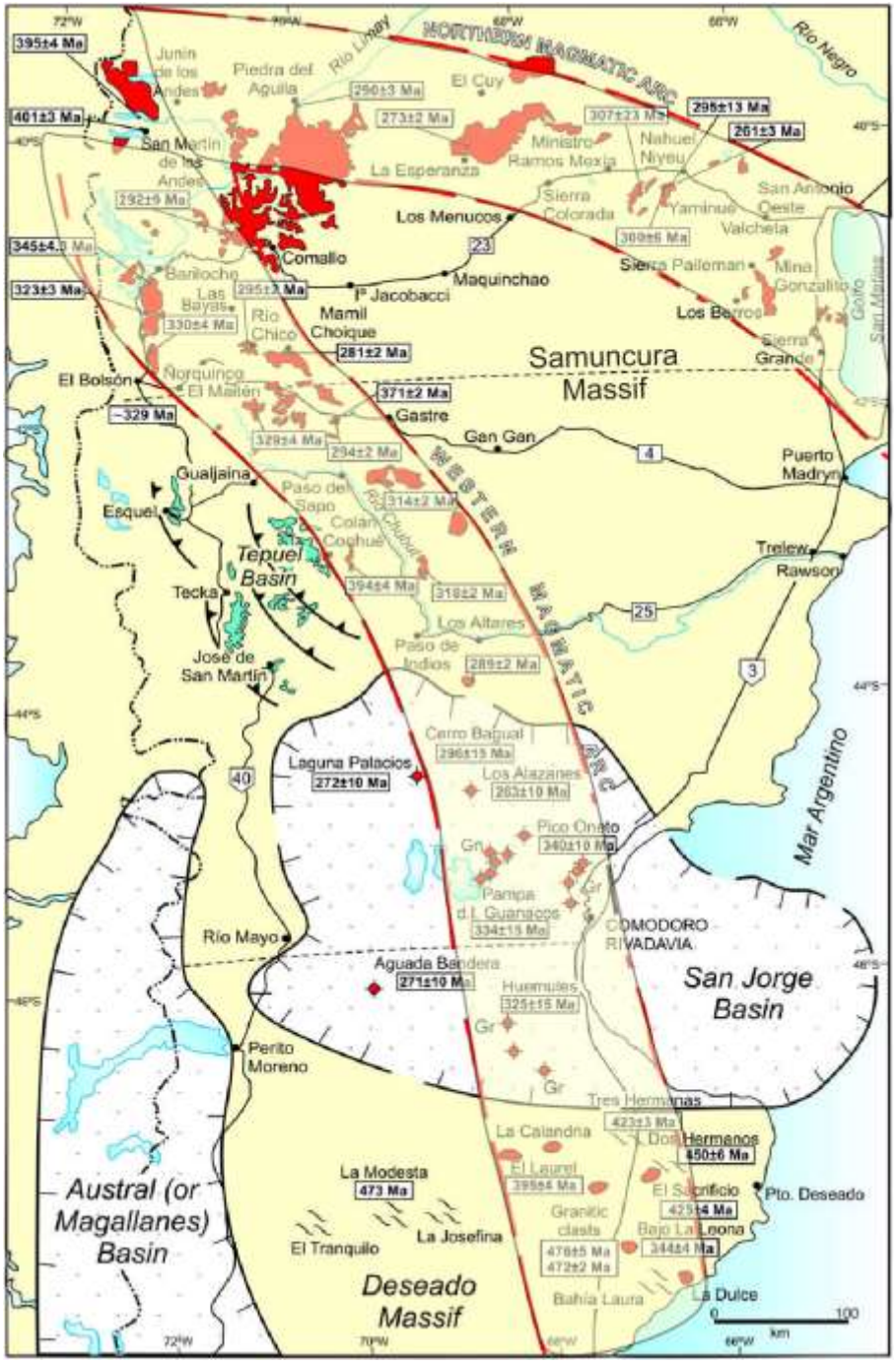

Figure 6 Location of the magmatic arcs in relation to Gondwana Passive Margin (north/northeast of the northern magmatic arc) and the Tepuel-Genoa Basin (southwest of the western magmatic arc). The Samuncura and Deseado massifs are labelled. Diagram also includes younger Cretaceous basins (modified from Ramos, 2008).

Despite the progress on the reconstruction of the tectonic history, debate on the exact timing and number of events that led to the formation of Patagonia is not completely resolved. Nonetheless, the tectonic history of Patagonia was complex during the Paleozoic and shows several episodes of rifting, fragmenting, convergence, accretion, renewed rifting and re-accretion to Gondwana (Ramos, 2008). Regardless, of its origin, two magmatic were in place in Patagonia during the late Paleozoic and may have influenced glaciation in the area. In addition, the Tepuel-Genoa Basin had two adjacent paleo-topographic highs; the Samuncura Massif to the north/east, and the Deseado Massif to the south/east (Leanza, 1958; Harrington, 1962; Limarino & Spalletti; Figure 6 & Figure 7) which could have influenced glaciation in the region.

The Tepuel-Genoa Basin has been interpreted to be a retroarc foreland basin by some (Limarino & Spaletti, 2006; Figure 6) and a forearc basin by others (Ramos, 2008; Ramos & Naipauer, 2014; Figure 5). The debate on the basin's origin (forearc vs. retroarc foreland basin) is problematic because the basin has characteristics of both basin types. Forearc basins are characterized as deep basins with abundant volcaniclastic sediments (Ciccioli et al., 2018). Whereas, retroarc foreland basins are typically shallower basins that often do not contain vast quantities of volcaniclastic sediments (Ingersoll, 1988; Nichols, 2009; Miall, 2010; Einsele, 2013).

The Tepuel-Genoa Basin is a deep basin which lacks abundant volcaniclastic sediments (Ciccioli et al., 2018). Isbell et al. (2011, 2013) and Survis (2015) interpreted strata within the Pampa de Tepuel Formation (stratigraphically older than the Mojón de Hierro Formation) in the basin as containing shelf and deep-water deposits, and Ciccioli et al. (2018) described only minor amounts of volcaniclastic sediment grains within the fill of the basin. Despite the different interpretations on exact basin type and the lack of direct basin classification, the Tepuel-Genoa

Basin is a marine basin deprived of volcaniclastic sediment (Isbell et al., 2011, 2013; Survis, 2015; Ciccioli et al., 2018).

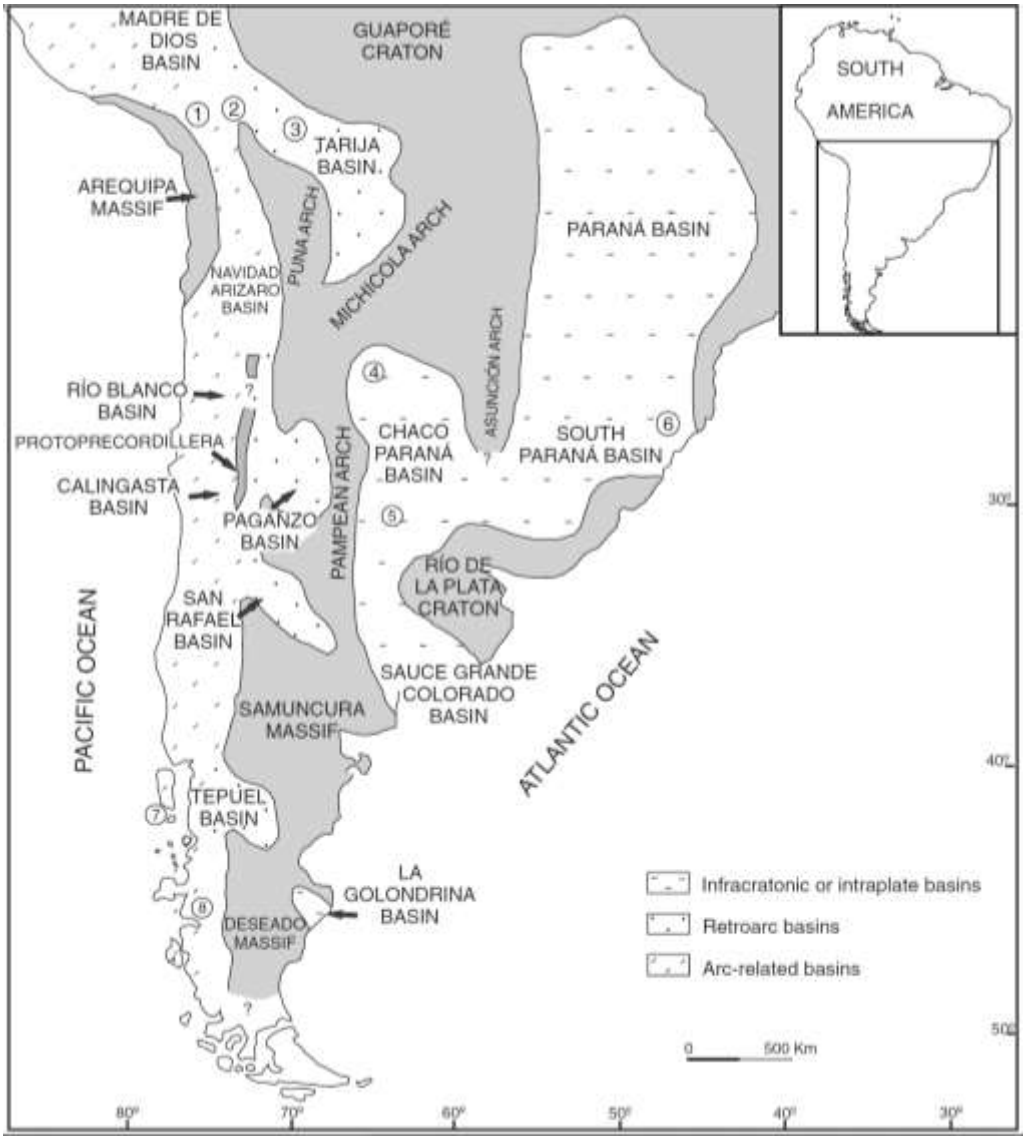

Figure 7 Basin type and location of the Tepuel-Genoa basin, depicted here as a retroarc basin, in relation to paleo-topographic highs, Samuncura Massif to the north/east and the Deseado Massif to the south/east (Limarino & Spaletti, 2006).

From the Late Carboniferous to Permian the Tepuel-Genoa Basin was positioned within the South Polar Circle (Figure 3) and accumulated a nearly continuous succession, comprised of

several formations. The Tepuel Group is composed of the Jaramillo, Pampa de Tepuel and Mojón de Hierro formations (Figure 8) which may total up to 6,000 m in thickness and consist predominately of marine, glaciomarine and glacially influenced marine strata (Frakes et al., 1969; Taboada et al., 2009). The glaciogenic deposits are only reported from the Pampa de Tepuel and the upper part of the Mojón de Hierro formations (Frakes, 1969; Freytes, 1971; Andreis et al., 1987, Taboada et al., 2009). Strata in the Mojón de Hierro Formation have been interpreted from a variety of environmental settings including: 1) shallow marine platform (Taboada et al., 2009; Gonzalez & Saravia, 2010), a glacially-influenced open shelf and slope (Limarino & Spaletti, 2006; Pagani & Taboada, 2010), 2) deep-water mass transport deposits (Isbell et al., 2011, 2013) and 3) deep-water glacially influenced deposits fed by adjacent ice streams (Griffis et al., 2018).

The Mojón de Hierro Formation is the youngest of the Tepuel-Group formations (Figure 8) and is biostratigraphically dated as Sakmarian (Figure 9; ~295 to ~290 Ma; Taboada and Pagani, 2010). These strata contain several marine invertebrate fossiliferous levels (Figure 8; Taboada, Pagani & Puerta, 2009) and a diverse fossil fauna including brachiopods, bivalves, gastropods, cephalopods, bryozoans and echinoderms (Suero, 1948; Riccardi & Sabattini, 1975; Sabattini et al., 1990b, 2006; Taboada, 1993, 1998, 1999, 2001; Pagani et al., 2002; Taboada et al., 2005; Pagani, 2004a, 2004b, 2005, 2006a, 2006b; Azcuy et al., 2007; Taboada and Pagani, 2010; Dineen, 2010). Near the upper part of the formation, there are two plant-bearing horizons that consist of thick shales with yellowish to greenish sandstones and minor intercalated conglomerates and siltstones (Andreís et al., 1987, 1996; Andreís & Cúneo, 1985; Cúneo, 1990) that suggest a possible marine regression. The majority of the exposed rock within the formation is heavily covered with lichen and not well-exposed.

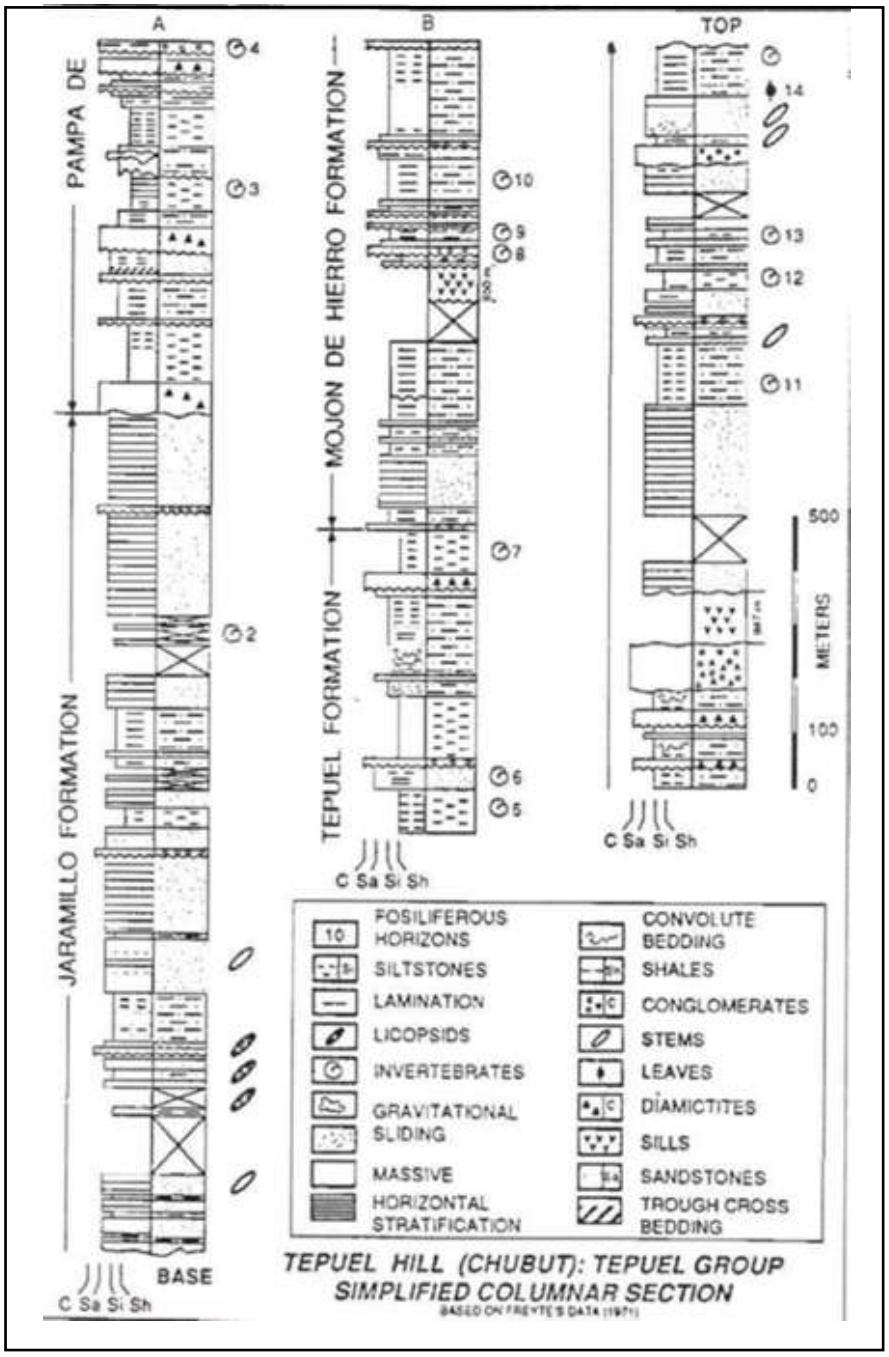

Figure 8 Stratigraphic column of the Tepuel Group; the Jarmillio, Pampa de Tepuel, and Mojón de Hierro formations. Showing their stratigraphic thickness, sedimentology, fossils, and their relationships to one another (from Freytes, 1971).

The lower section of the Mojón de Hierro Formation was interpreted to be a post-glacially deposited interval corresponding to a eustatic sea level rise during the late Assalian-Tastubian (Dickins, 1985; Taboada, 2001, 2008; Pagani & Taboada, 2010). Whereas the upper section of the formation is reported to exhibit a glacially-related interval with diamictites and shales with dropstones (Figure 9; Pagani & Taboada, 2010). The upper part of the formation, which is exposed at Arroyo Garrido, is also considered to represent the youngest evidence for concurrent glaciation (latest Carboniferous to Early Permian) from the Tepuel-Genoa Basin and in South America (Taboada, Pagani & Puerta, 2009; Isbell et al., 2012). Because of their paleogeographic position, deposit thicknesses, and ongoing debate surrounding the origin of the strata, the Arroyo Garrido section is important and its study will aid in understanding mid and high-latitude and regional paleoenvironments and overarching LPIA paleoclimate transitions.

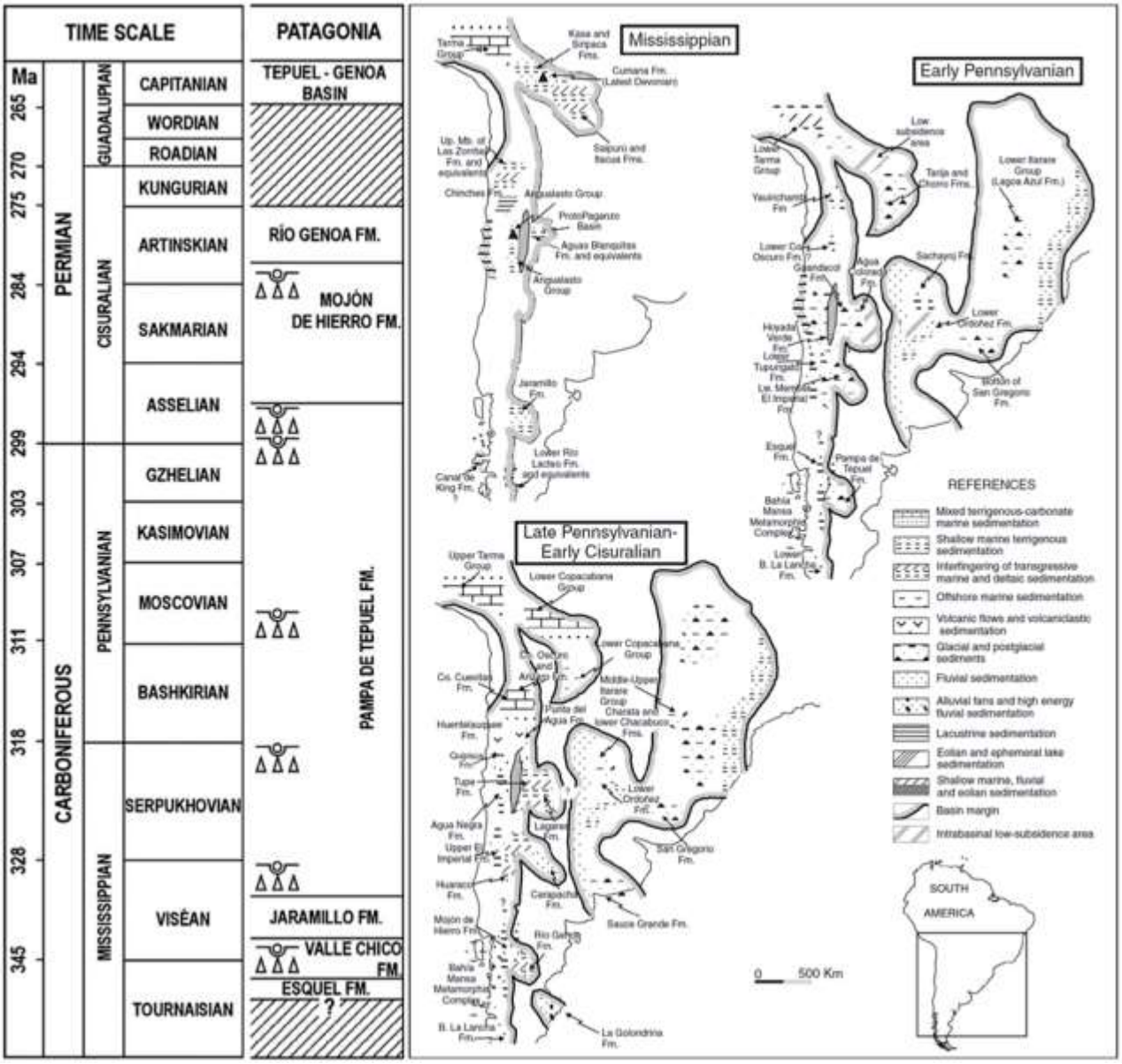

Figure 9 Tepuel-Genoa Basin formations (the Esquel, Valle Chico, Jarmillo, Pampa de Tepuel, Mojón de Hierro and Río Genoa formations) with time scale correlation. Triangles represent diamictites and circles represent dropstones (modified from Taboada, 2010 & Limarino and Spaletti, 2006).

5. METHODS

5.1 Sedimentological Methods

The study area (~ -43.841303°, ~ -70.680596°) for this thesis is located at Arroyo Garrido, Patagonia, in the Chubut Province of Argentina. Field work was conducted in April, 2018. The Mojón de Hierro Formation outcrops approximately 25 km north/northwest of Gobernador Costa (Figure 10). Much of the exposures in the Tepuel-Genoa Basin are covered by a thick lichen cover, however, strata at the study site are well exposed. Strata were examined in detail including describing lithology, grain size, unit thickness, sediment body geometries, sedimentary structures and deformational features. Hand samples were collected throughout the sections for micro-deformational features, mineralogical and geochemical analyses.

Five stratigraphic sections were measured laterally from the northwest to the southeast, using standard sedimentological techniques (Abney level, Jacob's staff and Brunton compass). Measured sections (NW to SE; Figure 10) are recorded as AG4, AG1, AG3, AG2 and AG5 with a total thickness of the sections approaching ~150 m (Figure 11). The strata dip at an average of 24° toward an azimuth of 100°.

The lithology of the strata was analyzed, logged in detail and photographed to aid in the interpretation of individual facies (individual stratigraphic columns are in Appendix A). To obtain the paleo-slope and paleo-flow directions, deformational features such as thrust faults/glide planes were measured and recorded. The thrust faults/glide planes that were measured are not the result of tectonic faulting but were caused by sliding/shearing that resulted from downslope movement of mass transport deposits prior to lithification. Paleo-slope direction can be predicted by the relationship of slope attitude and the orientation of resulting slump structures (Woodcock, 1979;

Strachan & Alsop, 2006). Sediment transport direction is opposite to that dipping thrust/glide plane (down slope direction) as a vergence direction.

There are many methods to obtain a paleo-slope orientation of mass transport deposits (Martinsen et al., 1994; Sharman et al., 2015) but the mean fault orientation method established from Farrell (1984) & Martinsen & Bakken (1990) was used in this study. Dip direction and dip angle measurements were taken from the thrust faults/glide planes. These recorded measurements were corrected for structural reorientation by rotating the data back to horizontal and then correcting for magnetic declination (addition of 7°47.22'; https://geomag.nrcan.gc.ca/calc/mdcal-en.php, field measurements are Appendix B) to obtain the dip of the paleo-slope. The dip direction is opposite (180°) of the vergence which is the slide direction.

The measurements create a series of points on a stereonet and a rose diagram can be generated to show the shortening direction representing the vergence/slide direction. The corrected measurements were then plotted using the computer program Stereonet (Almendinger et al., 2011) to obtain a stereonet and rose diagram, which determined the vergence of paleo-slope and paleo-flow directions. This data were compared to other published studies (Gonzalez-Bonorino, 1992) including their orientation of paleogeographic reconstructions. This data was also used to determine if the paleo-slope supports sediment sources located in the Ellsworth Mountains of Antarctica, testing the hypothesis of Griffis et al. (2018). The results and discussion of the paleo-flow determinations are in Section 7. Paleo-slope & Paleo-flow Results & Discussion.

The lithofacies interpretations combined with the paleo-slope and paleo-flow directions were used to reconstruct the paleoenvironment in the basin during at the time of deposition (Figure 12).

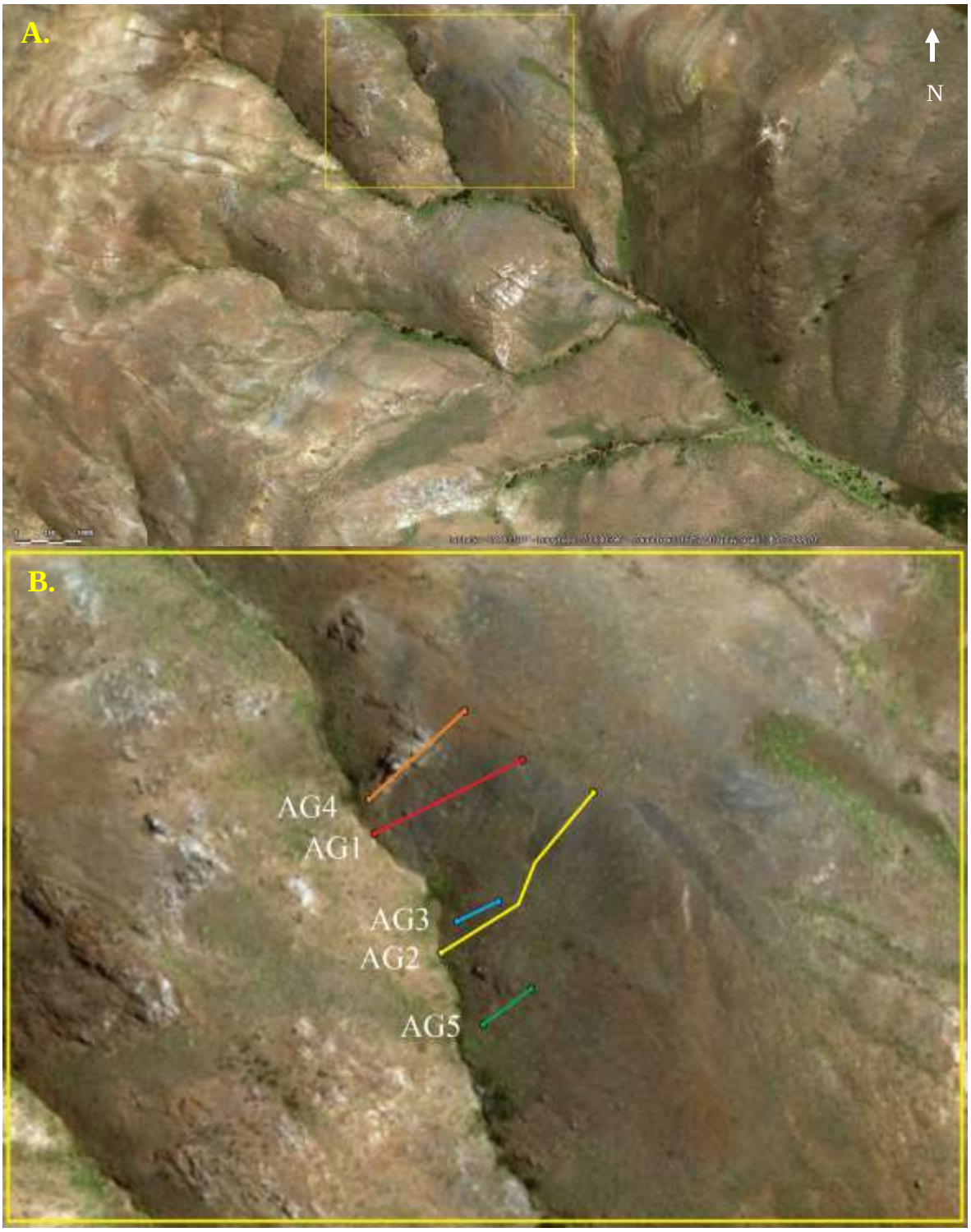

Figure 10 A) Aerial view of the study area, Arroyo Garrido, and scale (bottom left corner). Outlined area highlights location of B. North is upward. B) Close up aerial view from A showing the location of the five measured stratigraphic columns; AG4, AG1, AG3, AG2 and AG5.

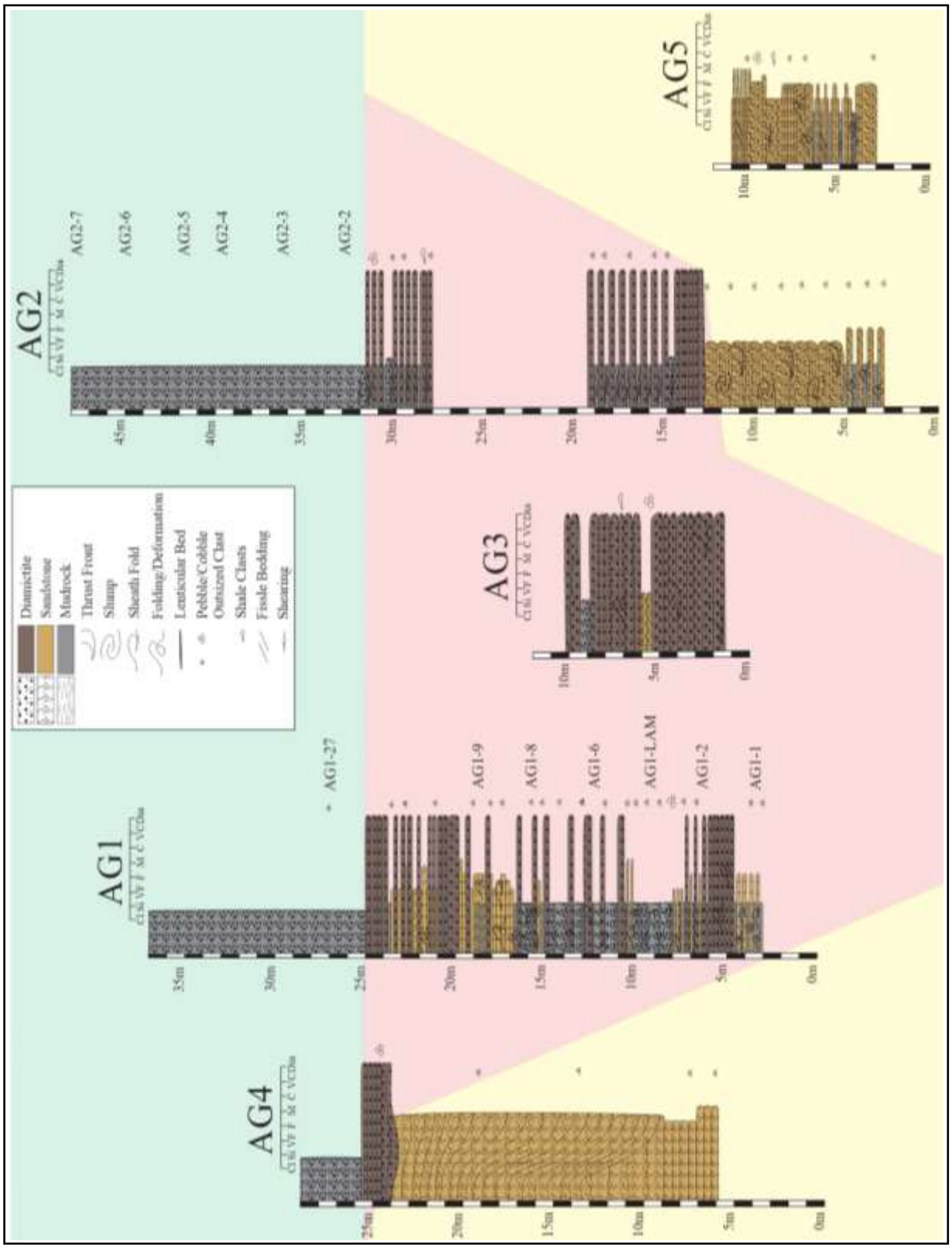

Figure 11 The measured stratigraphic columns. Geochemistry sample locations are labeled to the right of their respected column (AG1 & AG2). Green= Facies A; Red= Facies B, C & D; Yellow= Facies E.

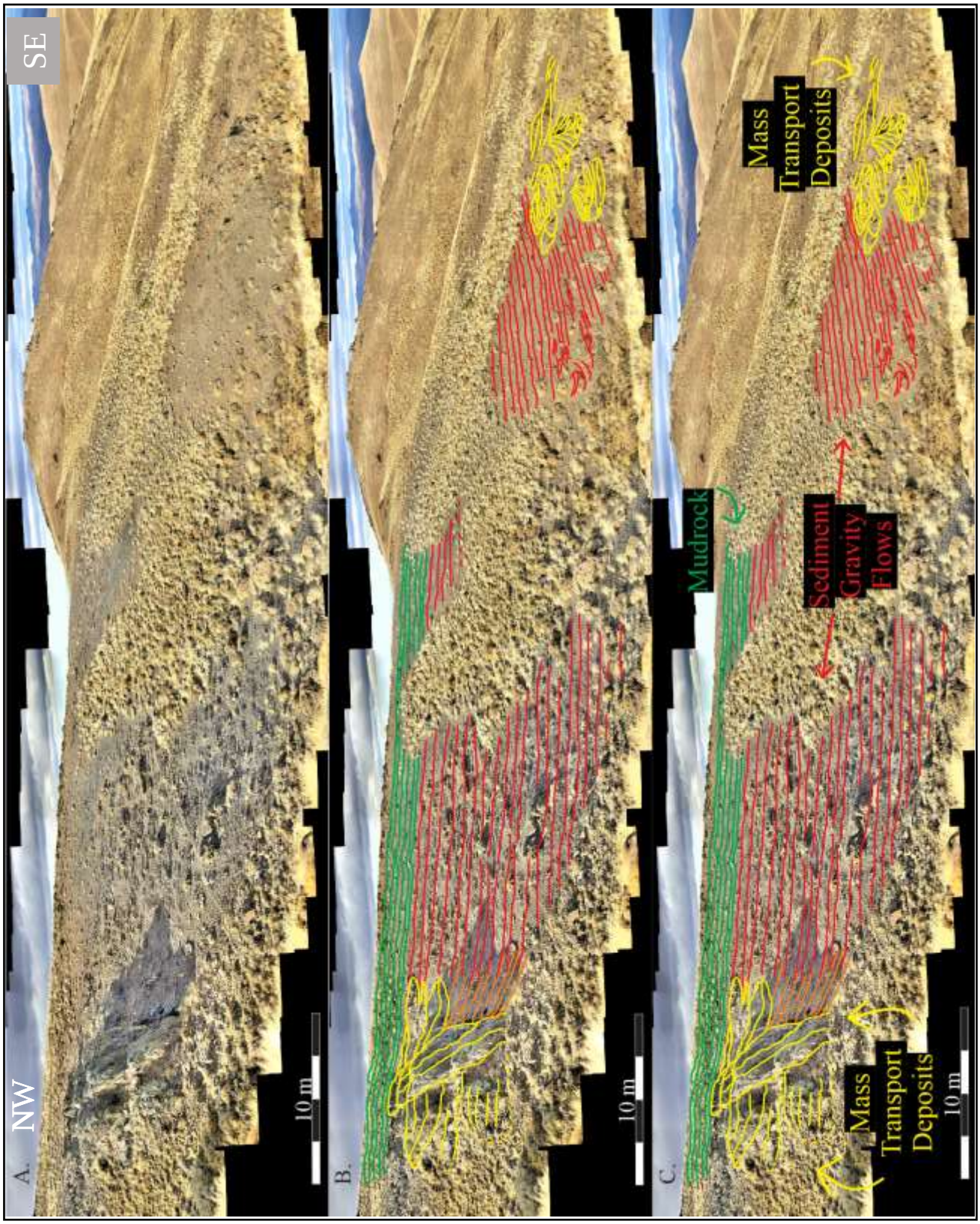

Figure 12 A.) An unannotated photo mosaic, B.) an annotated photo mosaic and C.) labeled photo mosaic of Arroyo Garrido (looking toward the East).

5.2. MINERALOGY & GEOCHEMISTRY METHODS

Bulk mineralogical and geochemical analysis of mudrocks from Arroyo Garrido was conducted using X-ray diffraction (XRD) and X-ray fluorescence (XRF) spectrometry. This was completed by collecting samples and obtaining bulk mineralogical (XRD) and elemental (XRF) concentrations. A total of thirteen hand samples were used for the geochemical analysis and were collected from two sections, AG1 and AG2, throughout a height of 48 meters (sample locations are labeled next to their stratigraphic column; Figure 11).

Samples for both XRD and XRF were prepared by first obtaining unweathered surfaces. Roughly 10 grams of the fresh rock were placed in a tungsten carbide shatterbox (~1 minute). Then the shattered sample was further powdered by hand using an agate mortar and pestle and acetone until an even particle size of ~ 63 μm was obtained. Samples were dried overnight in an oven at 105° C to expel any moisture.

XRD METHODS: XRD analysis was conducted on three (AG1-3, AG1-27, and AG2-7) of the thirteen samples, to determine the mineralogy of the bottom (AG1-3), middle (AG1-27) and top (AG2-7) of the measured strata. Each of the three samples was mounted as a random powder and analyzed using a Bruker D8 Focus XRD (Cu tube, 0.02° 2θ step size, 2-60° 2θ, 1 s/step) following methods from McHenry (2009) & McHenry et al. (2017). Minerals were identified using the Bruker EVA software which uses the International Centre for Diffraction Data Powder Diffraction Files (ICDD PDF) 2 database for comparison. The software matches the diffraction pattern measured by the machine (peak positions and relative peak heights) with the patterns

derived from mineral phases for which structural information is available in the database, and suggests likely mineral matches which can be assessed by the user (McHenry et al., 2017).

XRF METHODS: From each of the thirteen samples, one gram of powdered sample was heated to 1050º C in a muffle furnace to calculate the loss on ignition (LOI, %). Next, one gram of each powdered sample was mixed with 1.000 gram of oxidizer (ammonium nitrate) and 10.000 grams of a 50:50 lithium metaborate: tetraborate flux containing 0.5% LiBr integrated as a non-wetting agent. This mixture was fused at 1050ºC in a Claisse M4 programmable fusions system, creating a fused "bead". The fused beads were analyzed with a Bruker AXS, Inc. Pioneer S4 WD-XRF instrument to obtain major, minor and trace elemental data. This elemental data was processed by computer software which uses a calibration derived from eleven USGS rock standards (methodology and more details reported in McHenry, 2009; Beyers et al., 2016). Concentration values that approach or are just below the LLD are noted with a symbol (*) in section 9. Mineralogical & Geochemical Analysis Table 4. This XRD and XRF study was completed at the University of Wisconsin- Milwaukee, Geosciences Department.

The Chemical Index of Alteration (CIA) was calculated according to the equation;

$$CIA = [(Al_2O_3)/(CaO^*) + Na_2O + K_2O + Al_2O_3)] \times 100$$

(where CaO* represents the calcium content within silicate minerals; Young & Nesbitt, 1982). Values were compared to known CIA values of arid/glacial and other settings, 50-70 (Goldberg & Humayun, 2010). Trace elements vanadium and chromium are considered detectable if they have concentration levels (PPM) greater than or equal to double the Lower Limit of Detection (LLD) values and analytical error of less than 12%.

Detectable values for trace elements V and Cr were ratioed and compared to obtain information on oxygenation levels in the water column when sediment was deposited, a proxy used to determine paleo-oxygenation (Ernst, 1970; Jones & Manning, 1994). V/Cr concentration ratios were calculated using concentrations in PPM (parts per million) and were plotted against their stratigraphic height on separate graphs (see Section 9. Mineralogical & Geochemical Analysis).

6. FACIES ANALYSIS

Strata of the Mojón de Hierro Formation exposed at Arroyo Garrido were analyzed and categorized into five lithofacies associations; A) laminated mudrock, B) laminated mudrock with dispersed clasts, C) graded rhythmites, D) laminated and bedded diamictites and E) deformed bedded sandstones. These five lithofacies are summarized in Table 1 and described and interpreted in detail below. The classification of poorly sorted lithologies was made according to Hambrey & Glasser (2003), which is revised from Moncrieff's (1989) sediment sorting classification scheme. Facies codes are from Benn & Evans (2010) and are listed and defined in Table 2.

The distribution of various facies are presented in as the 'backwash' colors in the stratigraphic columns (Figure 11) and the line color within the photo mosaic (Figure 12). Facies A (laminated mudrock) is represented in green and is laterally continuous across the top of the measured outcrop. Facies A drapes over pre-existing relief (Figure 12). Facies B, C, and D (laminated mudrock with dispersed outsized clasts, graded rhythmites and laminated and bedded diamictites) are represented in red and occur beneath Facies A (Figure 12). Facies B, C and D are interstratified and lap onto Facies E. Facies E (deformed bedded sandstones) is represented in yellow and occur as massive blocks of sandstone on the sides of the measured outcrop (Figure 12).

Table 1 Summarized lithofacies descriptions, interpretations and depositional environments.

Facies	Lithologies	Sedimentary Structures	Bed Thickness	Interpreted Mechanisms	Depositional Environment
A. Laminated Mudrock	Mudrock containing clay & silt.	Horizontal laminations. No wave generated structures & no outsized clasts.	Laminations: 0.5-1 cm	Background sedimentation-settling from suspension.	Normal deep-marine to lower slope below storm wave base. No glacial influence.
B. Laminated Mudrock with Dispersed Clasts	Mudrock containing clay & silt. Some clasts present ranging in size from coarse sand to granules. Interstratified with Facies C, D & E.	Horizontal laminations. No wave generated structures. Outsized clasts.	Laminations: 0.5-1 cm	Background sedimentation settling from suspension. Ice rafted debris.	Basinal to lower slope below storm wave base. Glacially influenced.
C. Graded Rhythmites	Very fine- to medium- grained sandstone grading into mudstone, siltstone or very fine- grained sandstone. Interstratified with Facies B & D. Contains pebble to cobble outsized clasts.	Normal graded, horizontal laminations & beds. No wave generated structures. Outsized clasts.	Laminations: 0.5-1 cm Beds: 1-10 cm	Sediment gravity flows depositing turbidites. Suspension settling & ice rafted debris.	Basinal to lower slope below storm wave base near an unstable slope. Glacially influenced.
D. Laminated & Bedded Diamictites	Sandy to intermediate diamictites with clasts ranging in size from granules to pebbles, with rare cobbles. Interstratified with Facies B & C.	Internally massive & stacked. No wave generated structures. Outsized clasts.	Laminations: 0.5-1 cm Thin beds: 1-5 cm Thick beds: 5-150 cm	Sediment gravity flows (debris flows). Suspension settling & ice rafted debris.	Basinal to lower slope below storm wave base near an unstable shelf edge. Glacially influenced.
E. Deformed Bedded Sandstones	Fine- to medium-grained sandstone with outsized clasts ranging in size from granules to pebbles.	Internally massive, bedded sands, with outsized clasts. Some beds show deformation.	Beds: 5-50 cm Blocks: ~9 m x ~9 m	Mass transport deposits; Slides- no internal deformation. Slumps- internal deformation.	Basinal to lower slope near an unstable shelf edge. Glacially influenced.

Table 2 Facies codes, their descriptions and the facies with which they are associated. Facies codes and descriptions are from Benn & Evans (2010).

Facies Code	Description	Associated Facies
fm	Silts & clays internally massive	Facies A
fml	Silts & clays internally massive laminations	Facies A
fmld	Silts & clays internally massive laminations with dropstones	Facies B
fmd	Silts & clays internally massive with dropstones	Facies B
suf	Sands, upward fining	Facies C
sufd	Sands, upward fining with dropstones	Facies C
flv	Silts & clays laminations with rhythmites or varves	Facies C
flvd	Silts & clays laminations with rhythmites or varves and dropstones	Facies C
dml	Diamictons, matrix-supported laminated	Facies D
dms	Diamictons, matrix-supported stratified	Facies D
shd	Sands, horizontally bedded with dropstones	Facies E
shdd	Sands, horizontally bedded with dropstones and deformed	Facies E

6.A Facies A: Laminated Mudrock

6.A.1. DESCRIPTION: The laminated mudrock (fm/fml) facies is up to +10 m thick and laterally continuous across the outcrop surface at Arroyo Garrido (Figure 11 & Figure 12). This facies is typically in sharp contact with adjacent facies and occurs at the top of the studied succession (Figure 12). Mudrock also laps on to the top and drapes over the deformed bedded sandstone of Facies E (Figure 12) that dominates section AG4. Facies A is characterized by dark to light grey, horizontally laminated mudrock (0.5 to 1 cm thick) without outsized clasts (Figure 13). However, one outsized clast did occur at the base of this facies in section AG1. Symmetrical ripples and hummocky cross stratification does not occur within this facies. Fossils were not observed in the measured sections. However, similar mudrocks in the area contain a diverse fossil fauna that consists of brachiopods, bivalves, gastropods, cephalopods, bryozoans, and echinoderms (Suero, 1948; Riccardi & Sabattini, 1975; Sabattini et al., 1990b, 2006; Taboada, 1993, 1998, 1999, 2001; Pagani et al., 2002; Taboada et al., 2005; Pagani, 2004a, 2004b, 2005, 2006a, 2006b; Azcuy et al., 2007; Taboada and Pagani, 2010; Dineen, 2010). Mudrock extends for 10's of meters beyond the measured section but outcrops poorly. Elsewhere, at Arroyo Garrido and within the Tepuel-Genoa Basin, the Mojón de Hierro Formation is dominated by mudrocks with thickness of individual units exceeding 200 m.

Figure 13 Facies A: characterized by dark to light grey, horizontally laminated mudrock with laminations 0.5 to 1 cm thick.

6.A.2 INTREPRETATION: The presence of marine invertebrate fossils within laminated mudrocks in the Mojón de Hierro Formation indicate deposition in a marine environment (Suero, 1948; Riccardi & Sabattini, 1975; Sabattini et al., 1990b, 2006; Taboada, 1993, 1998, 1999, 2001; Pagani et al., 2002; Taboada et al., 2005; Pagani, 2004a, 2004b, 2005, 2006a, 2006b; Azcuy et al., 2007; Taboada and Pagani, 2010; Dineen, 2010). The absence of wave generated sedimentary structures (e.g., symmetrical ripples and hummocky cross-stratification) indicate that deposition from settling from suspension occurred in deep-water below storm wave base. Due to the dominance of mudrock within the Mojón de Hierro Formation (Freytes, 1971; Taboada & Pagani, 2010), this unit is interpreted to represent background basin sedimentation, which drapes preexisting topography on the basin floor as seen by Facies A onlapping and draping underlying topography across Facies E (Figure 12). Elsewhere, poorly exposed mudrock units within the formation are up to several hundred meters thick (Figure 12; Freytes, 1971). The absence of sandstones within this facies indicates long intervals when the basin was starved of coarse clastics,

and deposition in deep water far from points of clastic influx to the basin. Such thick mudrock successions typically occur within marine slope environments when sands are trapped in nearshore environments on the shelf, such as during relative sea-level highstands (Catuneanu, 2006; Miall, 1997). The absence of dropstones in this facies indicate an absence of glaciomarine influences in the basin at the time Facies A was deposited. The mineralogical and bulk geochemistry data also (see Geochemistry sections 8-10) indicate normal marine conditions.

6.B Facies B: Laminated Mudrock with Dispersed Clasts

6.B.1 DESCRIPTION: The laminated mudrock with dispersed clasts facies (fmld/fmd) range from 0.01 to 2 m in thickness. Facies B occurs in sections AG1, AG2, AG3 and AG5 and is commonly interstratified with graded rhythmites (Facies C) and laminated and bedded diamictites (Facies D) (Figure 12& Figure 14). This unit is characterized by dark to light grey horizontally laminated (0.5 to 1 cm thick) mudrock (Figure 15) with dispersed clasts. Clasts range in size from coarse sand to pebbles. Composition of the clasts vary between greywacke, sandstone, quartz and feldspar. Roundness of clasts ranges from subangular to rounded. No symmetrical ripples, hummocky cross stratification, or fossils were observed within the measured sections. This facies is similar to Facies A, but unlike Facies A, this facies contains dispersed outsized clasts.

Figure 14 Facies B, the laminated mudrock with dispersed outsized clasts.

Figure 15 Facies B showing its dark to light grey horizontally laminated (0.5-1 cm thick) mudrock characteristics.

6.B.2 INTERPRETATION: The absence of sedimentary structures, especially structures produced by wave activity indicates deposition occurred in a deep-water, marine environment (Freytes, 1971; Taboada & Pagani, 2010) below storm wave base. This facies varies from Facies A in that these mudrocks have dispersed coarse clastics (clasts) contained within the facies. Although the dispersed clasts do not distinctively appear to bend or penetrate the underlying laminations, deformed laminations beneath clasts are frequent in the graded rhythmites facies (see Facies C) and are present in the laminated and bedded diamictites facies (Facies D). The dispersed clasts are interpreted to be deposited as ice rafted debris dropped in from icebergs floating over deep-water, indicating a distal glacial influence on sedimentation within the basin. Even though icebergs are known to drift thousands of kilometers away from glaciomarine ice fronts, the presence of dropstones in Facies B suggest that ice was in contact with marine waters and that icebergs were able to traverse the basin.

6.C Facies C: Graded Rhythmites

6.C.1 DESCRIPTION: The graded rhythmite facies (suf/sufd & flv/flvd) ranges from 0.01 to 2.5 m in thickness and is commonly interstratified with laminated mudrock with dispersed clasts (Facies B) and laminated and bedded diamictites facies (Facies D) (Figure 12). Facies C occurs throughout sections AG1, AG2 and AG5 (Figure 11). Units are not laterally continuous across the outcrop sections, but occur as discontinuous beds tens of meters in length. The basal and upper contacts of these units are horizontal and sharp on a macroscale, but erosional on a mm-scale (Figure 16). The graded rhythmite facies is characterized by horizontal laminations (0.25 to 1 cm thick) or beds (1 to 10 cm thick) of very fine- to medium- grained sandstone that grades upward into mudstone, siltstone or very fine- grained sandstone (Figure 16 & Figure 17).

Soft-sediment deformation is common on both a small-scale (cm) (Figure 18, Figure 19 & Figure 20) and large-scale (m) (Figure 21, Figure 22 & Figure 23) within Facies C. Small-scale soft-sediment deformation includes recumbent folds, sheath folds, Z folds, S folds, listric faults and thrust faults. Some deformed layers display discontinuous folded stratification (Figure 21). Large-scale soft-sediment deformation includes stacked sheath folds and listric and thrust faults (Figure 21). Outsized clasts are frequent in this facies and penetrate and/or bend the underlying stratification (Figure 16, Figure 18 & Figure 23). Clasts are subangular to round and range in size from granules to pebbles with rare cobbles, and are composed of greywacke, sandstone, quartz and feldspar. Fossils, symmetrical ripples and hummocky cross stratification are absent from Facies C.

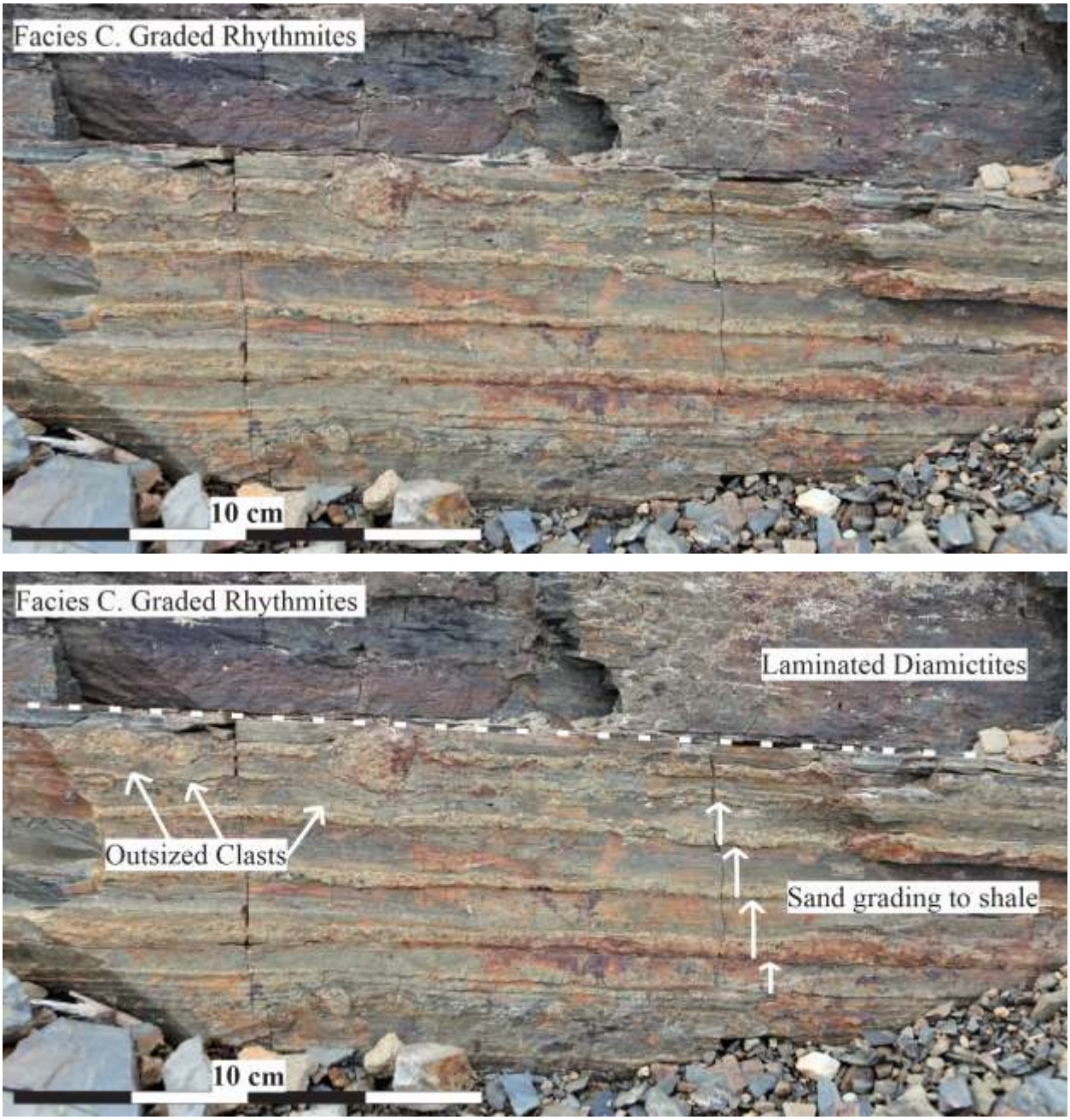

Figure 16 Normal grading in the rhythmites showing the upper contacts of Facies C characterized by horizontal and sharp but erosional on mm-scale.

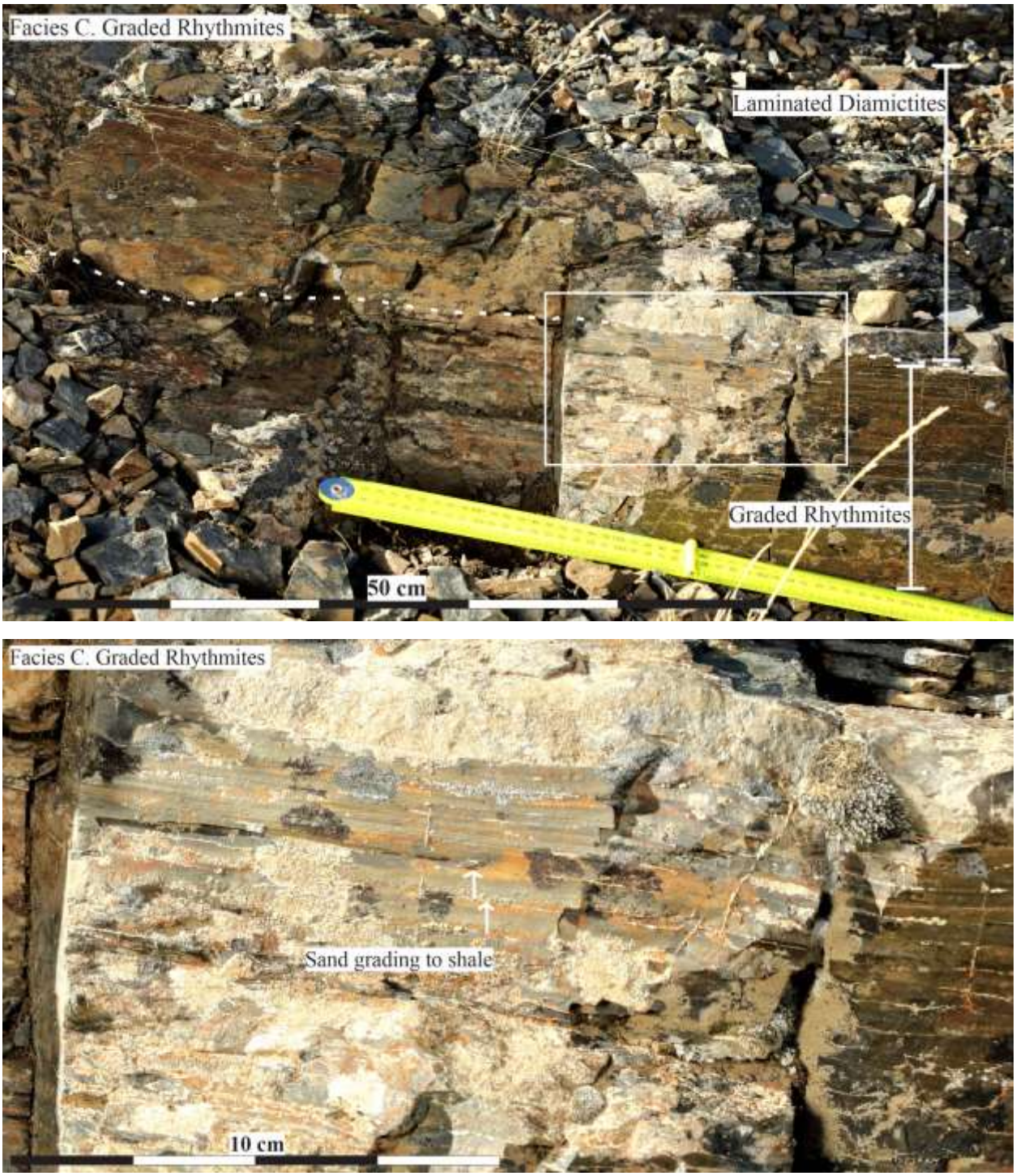

Figure 17 Graded rhythmite facies, showing its characteristic horizontal laminations (0.25 to 1 cm). These graded laminations are fine-grained sandstone that grades into silt.

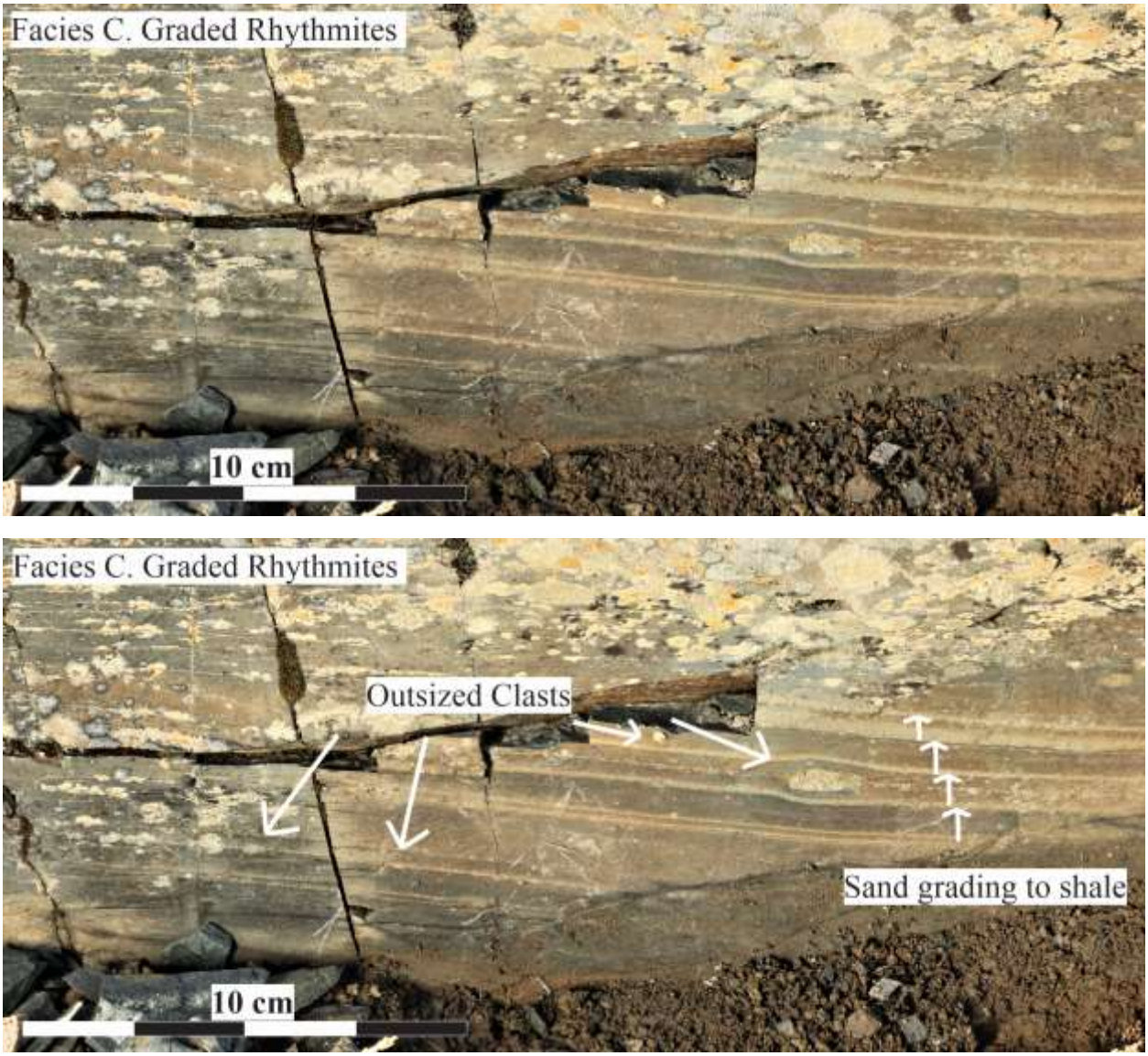

Figure 18 Graded rhythmite facies showing it characteristic (1 to 10 cm) of fine- to medium-grained sandstone grading into siltstone with outsized clasts that bend the underlying stratification.

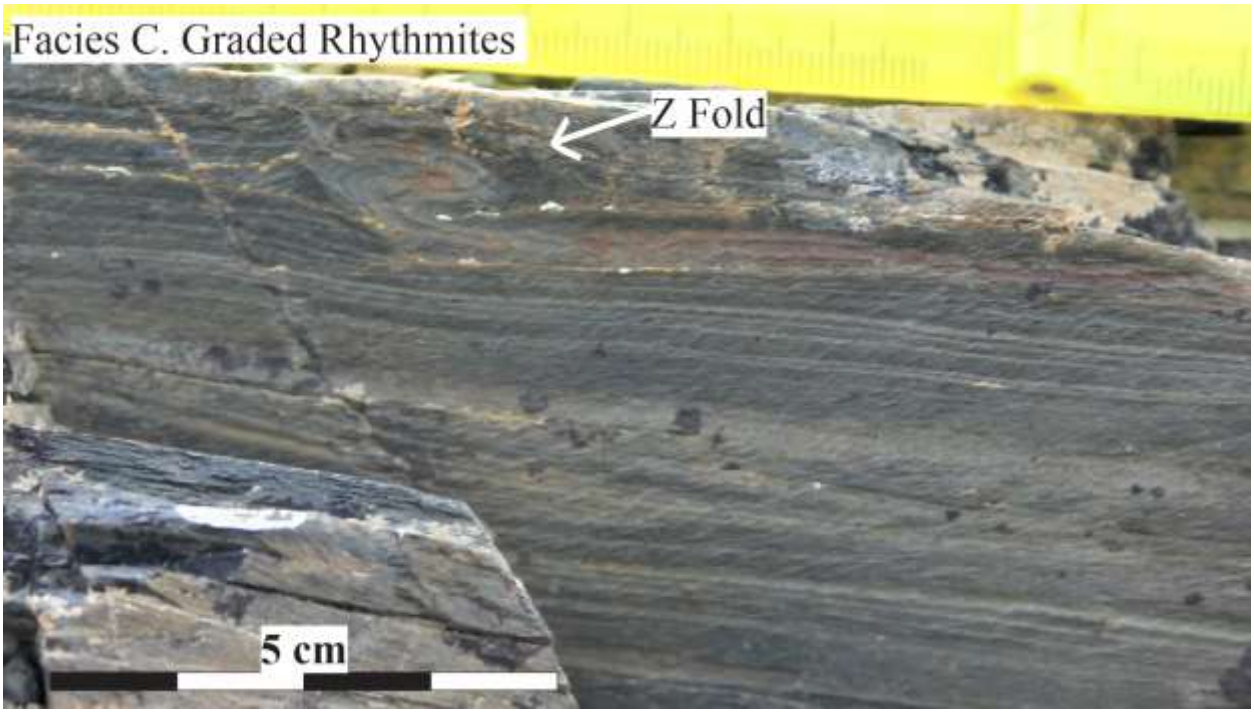

Figure 19 Facies C, graded rhythmites, thin horizontal laminations very fine- grained sandstone that grades into siltstone. Small-scale (cm) soft-sediment deformation is present and can be seen in the graded rhythmites, in the form of an overturned (Z) fold.

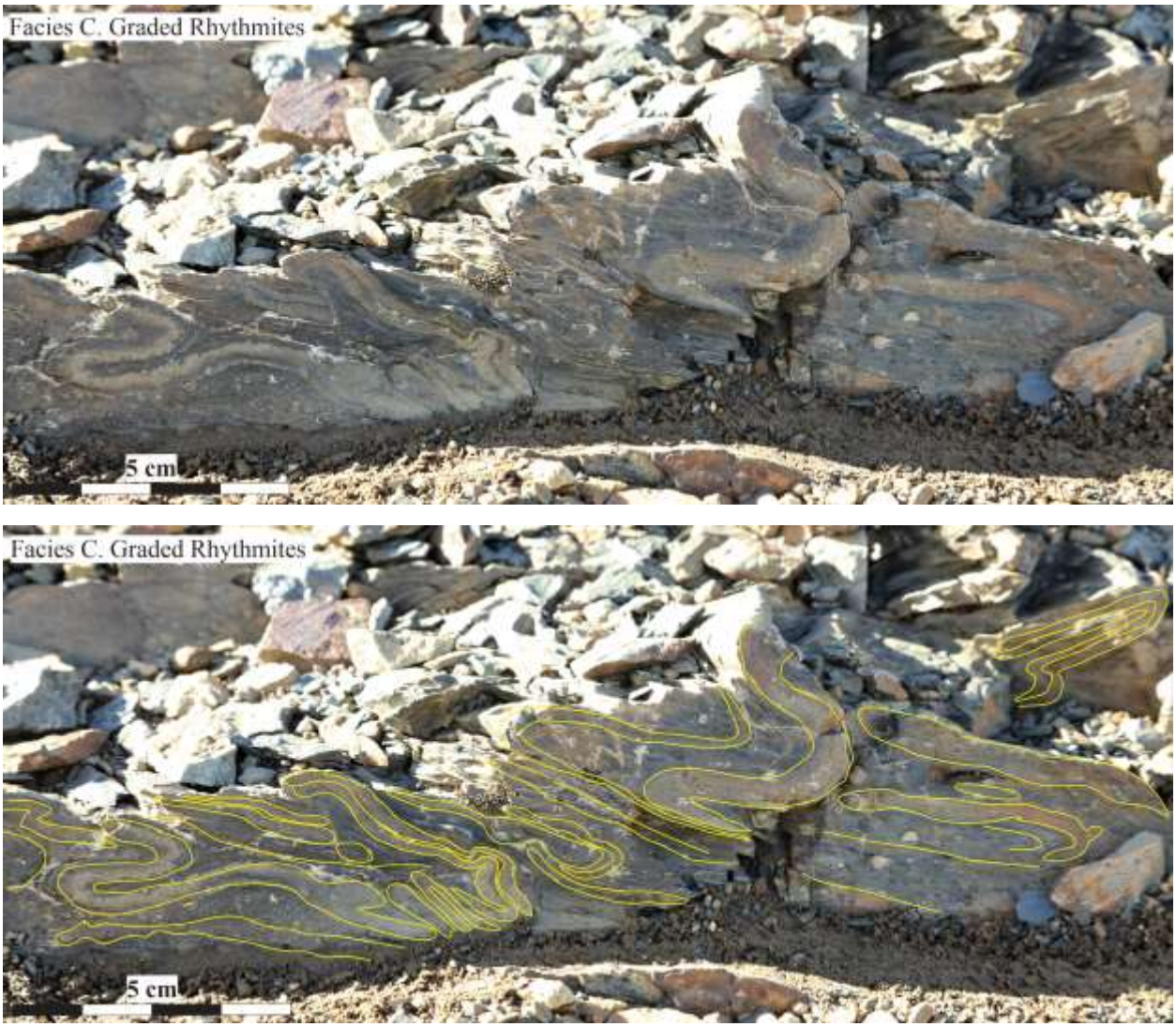

Figure 20 Small-scale (mm) soft-sediment deformation is present and can be seen in the graded rhythmites.

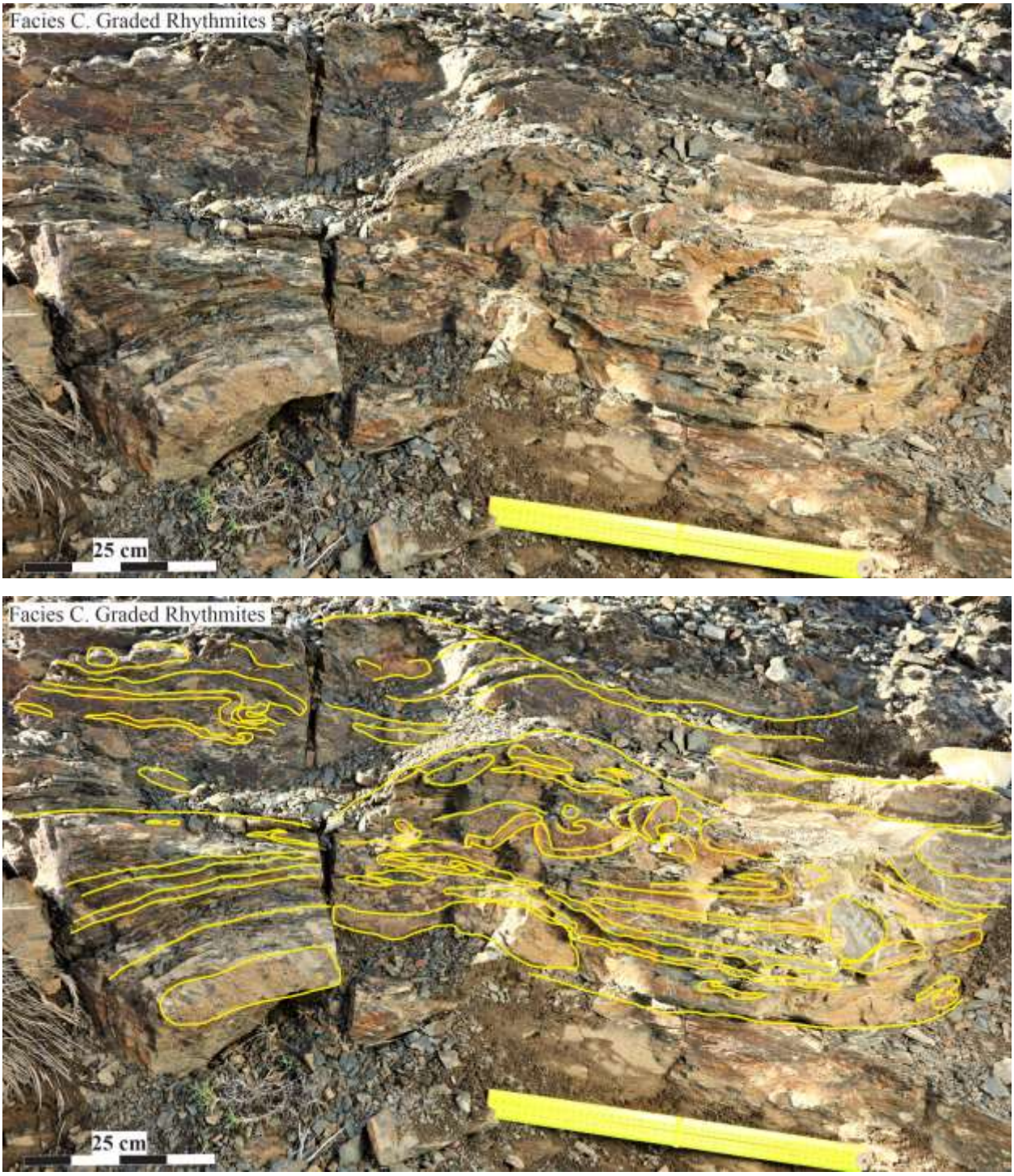

Figure 21 A) Unannotated photograph of large-scale deformation B) Annotated photograph of large-scale deformation, deformed rhythmite layers display discontinuous folded stratification.

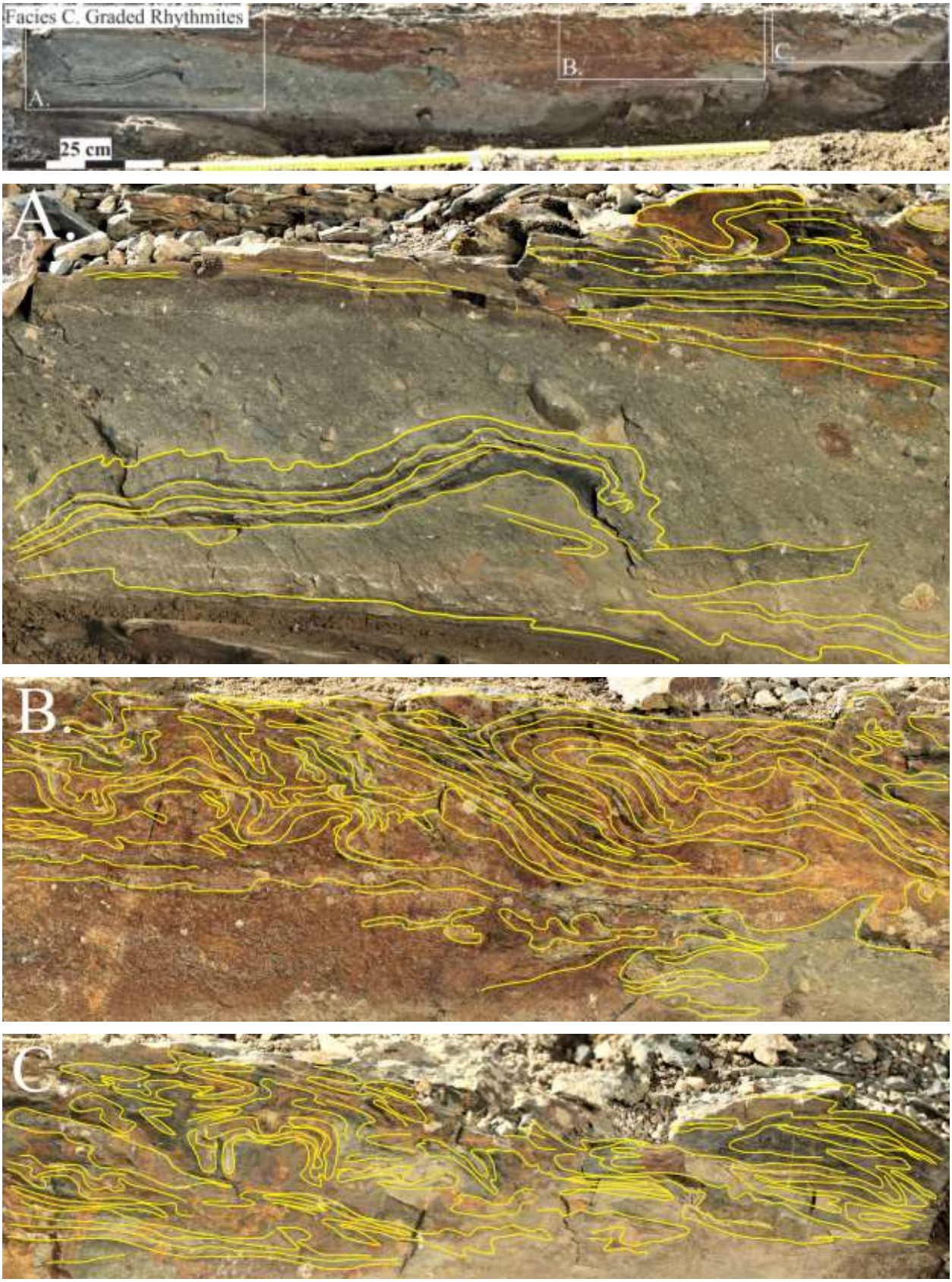

Figure 22 Small-scale deformation seen in the rhythmites and interbedded diamictites.

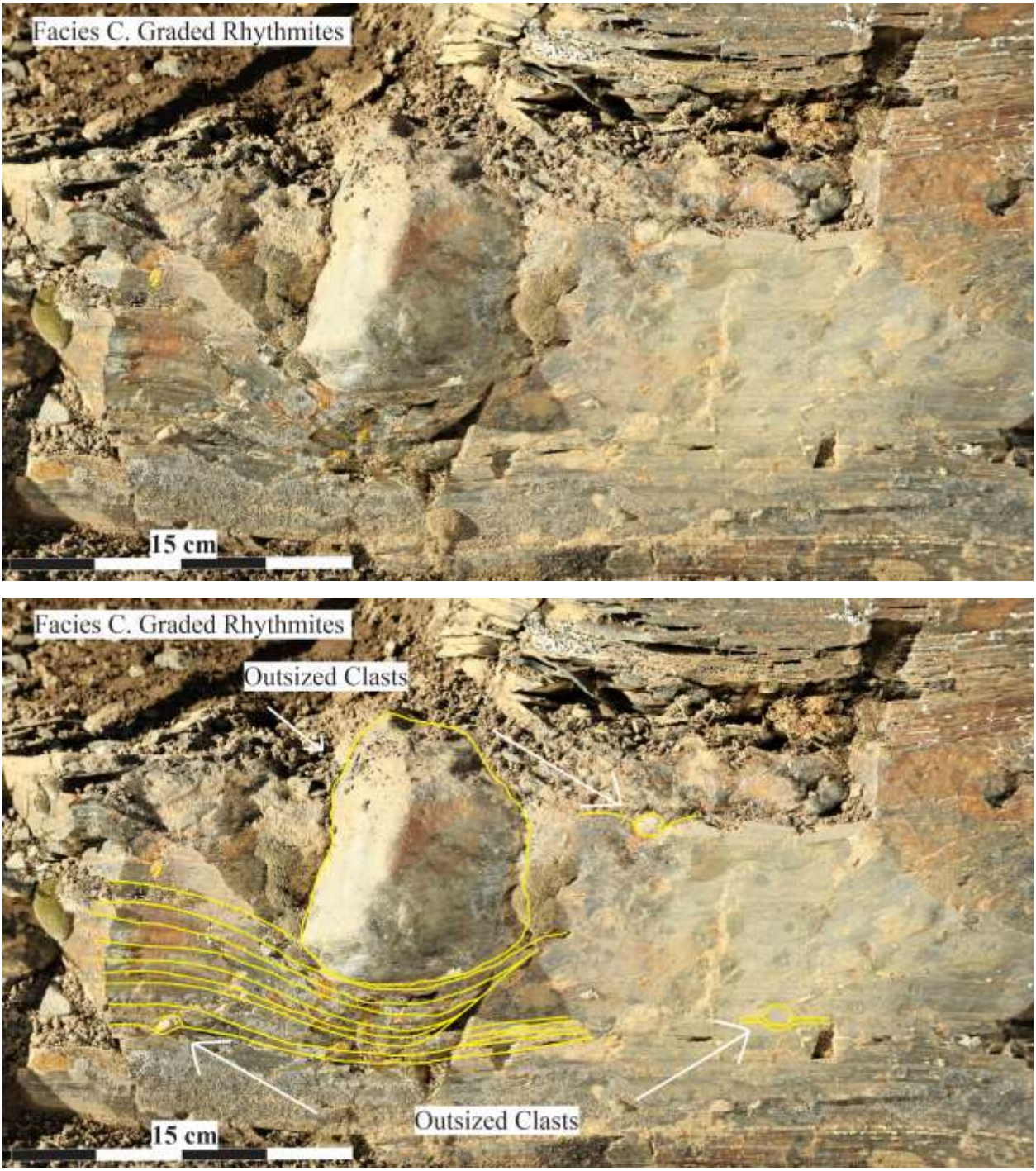

Figure 23 Large cobble sized outsized clasts penetrating and bending the underlying stratification. Clasts are subangular to round and range in size from granules to pebbles.

6.C.2 INTERPRETATION: The graded rhythmites facies were deposited by episodic subaqueous density currents, in the form of turbidity currents as suggested by the presence of graded beds (cf. (Hampton, 1972; Mulder & Alexander, 2001; Talling et al., 2012; Pickering, 2016). These units were deposited in deep water below storm wave base as indicated by an absence of wave generated structures. Turbidity currents are driven by density differences between the currents and ambient marine waters under the influence of gravity (Mulder & Alexander, 2001; Pickering & Hiscott, 2016). Gravity causes the turbidity current to flow down a slope depositing sediment from a turbulent medium. However, deposition could have also been from a concentrated density flow with flow due to a combination of grain collisions and turbulence followed by fine grained sediment settling from suspension (Pickering & Hiscott, 2016). In this fashion, coarser material is deposited first followed by subsequent finer grains as the velocity wanes, which produces normally graded beds (Nichols, 2009).

Small-scale soft-sediment deformation in these units is interpreted to be due to either the retention of pore pressure, fluid escape of pore waters, sediment creep down a slope, or from the shocking of the water saturated sediment by subsequent flows (Posamentier, 2006). Larger-scale deformation suggests mass movement and downslope movement of the entire rhythmite mass (Posamentier & Walker, 2006; Strachan, 2008). The stacking of the large-scale deformation suggests sedimentation and deformation was occurring from repeated episodic events. Outsized clasts which penetrate/bend the underlying strata are interpreted as dropstones, deposited by ice rafted debris dropped in from icebergs as they melt or overturn (Thomas & Connell, 1985; Gilbert, 1990; Woodward, Lynas & Dowdeswell, 1994; Powell & Domack, 2002).

6.D Facies D: Laminated and Bedded Diamictites

6.D.1 DESCRIPTION: The diamictites facies occurs as laminated (dml) to bedded (dms, thin and thick) units reaching up to 4 m in thickness and occurring in sections AG1, AG2, AG3 and AG4, but absent in AG5 (Figure 11). Laminated diamictites units range in thickness from 0.2 to 3 m and occur in sections AG1 and AG3, and are laterally discontinuous throughout the exposed outcrop (Figure 11). The bedded diamictites units range in thickness from 0.1 to 4 m thick and occur in sections AG1, AG2, AG3 and AG4. The diamictites are commonly interstratified with laminated mudrock with dispersed clasts (Facies B) and graded rhythmites (Facies C; Figure 24). This facies underlies the laterally continuous laminated mudrock (Facies A) at the top of sections AG1, AG2 and AG4 (Figure 11). Facies D has basal and upper contacts that are predominately erosional to slightly deformed (Figure 25) and the basal diamictites in this facies often fill existing relief and topography developed on underlying sediment bodies, most noticeably over deformed bedded sandstones (Facies E; Figure 11) in sections AG2 and AG4. Facies D laterally interfingers with Facies E between sections AG4 and AG1 (Figure 12), which are the two most northly measured sections. The laminated and bedded diamictites are commonly interstratified with Facies B and Facies C, and were deposited as undulating laminations (0.5 to 1 cm thick) (Figure 24 & Figure 25), thin beds (1 to 5 cm) and thick beds (5 to 100 cm) beds. Stratification is occasionally weak or poor and can display individual, discontinuous, thin, lens-like bodies of diamictites commonly pinching out or truncated laterally.

The laminated and bedded diamictites facies are characterized by dark to light grey, internally massive, clast-poor (<5% clasts) to clast-rich (>5% clasts) sandy to intermediate diamictite with a predominately siltstone matrix (Figure 26). Clasts are sub-rounded to well-rounded and range in size from granules to pebbles to and occasional cobbles. The matrix of the

laminated and bedded diamictites displays subtle fluctuations in the abundance of clay, silt content, as well as the abundance of clasts and sand. Within this facies there are outsized clasts that are thicker than individual laminations and that bend the underlying laminations (Figure 27). The composition of the clasts vary between greywacke, sandstone, quartz and feldspar, as well as, shale rip-up clasts. Soft sediment deformation is common in this facies on the cm- to m- scale and occurs as folded (Figure 25), almost exclusively as thrust folds and fold noses (some exhibiting stacking with sheared interstratified mudrock of Facies B). Clasts penetrating underlaying stratification also occur (Figure 27). The interstratified mudrock with dispersed clasts (Facies B) regularly displays evidence of shearing on its upper surface below the diamictites and in some places has narrow laterally restricted grooved surfaces.

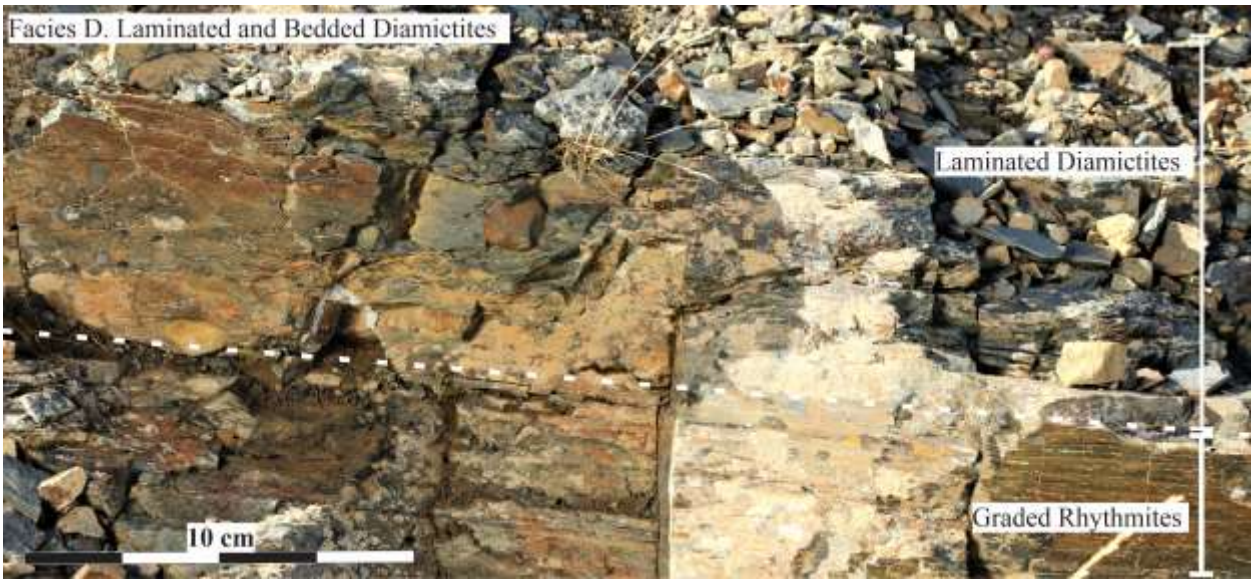

Figure 24 Laminated and bedded diamictites facies (Facies D) interstratified with the graded rhythmites (Facies C). The contact is sharp but erosional on mm scale.

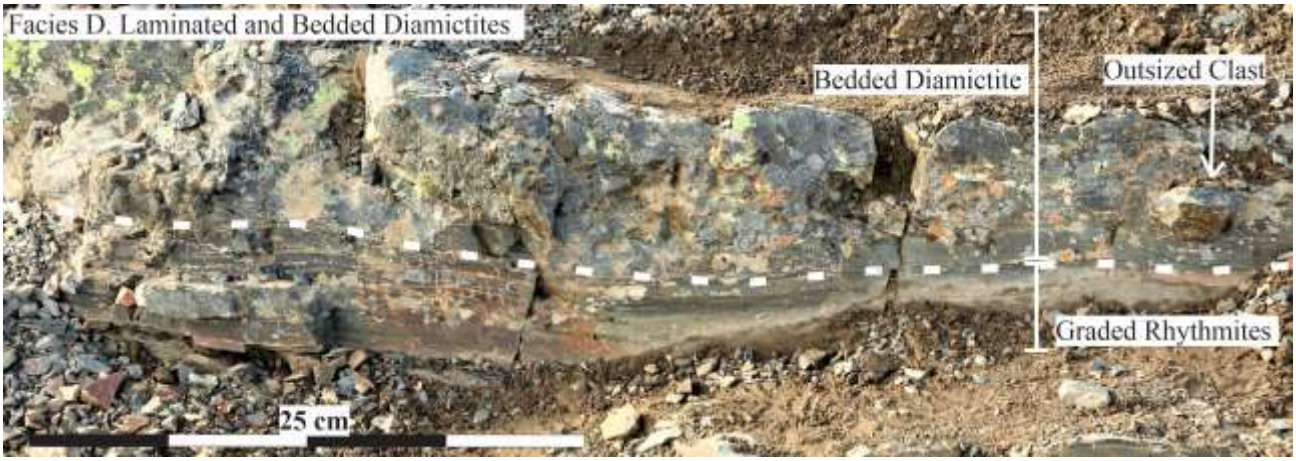

Figure 25 The contacts of Facies D, erosional to slightly deformational and filling existing relief and topography from underlying stratification.

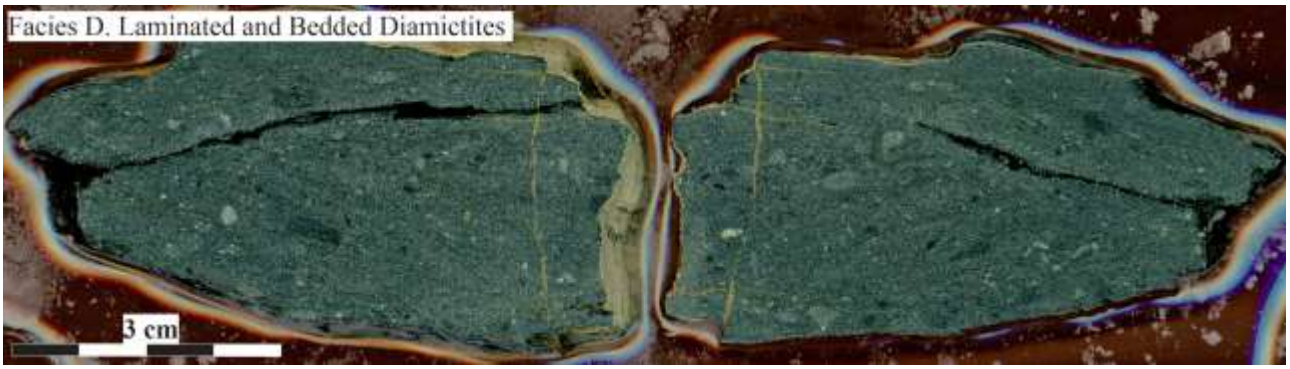

Figure 26 Hand sample of the laminated and bedded diamictites facies cut in half. The sandy to intermediate diamictite characteristics are observed.

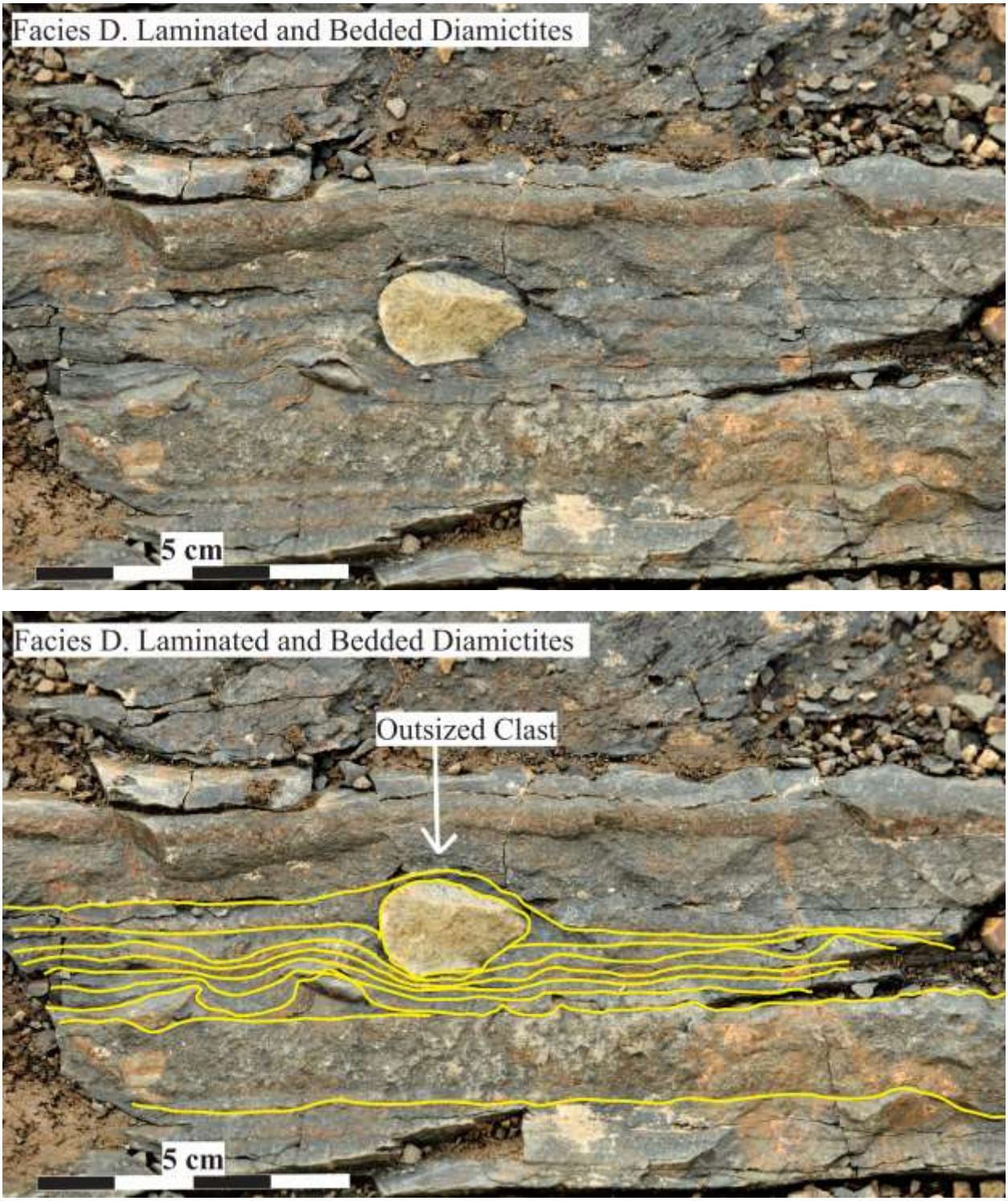

Figure 27 Laminated diamictites, Facies D, deposited as horizontally undulating laminations (0.5 to 1 cm thick), rounded and sub-rounded outsized clasts that penetrate underlying stratification.

6.D.2 INTERPRETATION: The laminated and bedded diamictites facies were deposited in deep-water as indicated by an absence of wave structures within the succession. They were deposited as episodic subaqueous cohesive debris flows (sediment gravity flows) as indicated by their thin and stacked nature. Debris flows are considered Bingham plastic flows, in which clasts are supported by matrix strength, dispersive pressure and buoyant lift (Shanmugan, 1996).

Debris flows commonly originate from sediment in an unstable setting with marine shelf edges and slopes being a common subaqueous source (Hampton; 1972; Lee et al., 2007). Triggers emanate from a number of natural manifestations (including the presence of a temperate glacier or ice sheet nearshore, meltwater, outwash or deltas delivering sediment to the shelf edge, the oversteepening of the shelf edge, seismic activity, storms, and slides and slumps that devolve into debris flows (Hampton, 1972; Strachan & Alsop, 2006), activate unstable sediment resulting in the sediment gravity flow (Posamentier & Walker, 2006; Lee et al., 2007). Due to the thinness of the individual debris flows and the predominately granule and pebble sized clasts, these flows were likely distal in nature (Posamentier & Martinsen, 2011). The stacking of debrites suggest that the diamictites were deposited by episodic sediment gravity flows from an unstable shelf edge.

The soft-sediment deformation occurring as folding within the diamictites occurred from the remobilization of cohesive debris flow deposits, resulting from material sliding downslope and from frictional differences between the base of the bed and substrate as the sediment mass slide over underlying sediment (Martinsen, 1989, 1994; Lopez Gamundi, 1991; Posamentier & Martinsen, 2011). The sub-rounded to well-rounded clasts indicate the clasts were subjected to abrasion, likely due to rounding by turbulent flows sometime in their history (Nichols, 2009). The outsized clasts that are thicker than individual laminations of the diamictites that bend and penetrate the underlying laminations are interpreted as dropstones deposited from icebergs

(Thomas & Connell, 1985; Gilbert, 1990; Woodward, Lynas & Dowdeswell, 1994; Powell & Domack, 2002).

6.E Facies E: Deformed Bedded Sandstones

6.E.1 DESCRIPTION: The deformed bedded sandstone facies (shd/shdd) displays two different deformational styles; 1) stacked blocks of sandstone that are internally undeformed (Facies Ea) and 2) stacked bodies of sandstone with internal deformation (Facies Eb).

The deformed bedded sandstones that occur as internally undeformed stacked blocks of sandstone (Facies Ea; Figure 28) reach up to 15 m in thickness and are exclusive to section AG4, the northern-most section. This unit is laterally adjacent to other sandstones of Facies C and diamictites of Facies D (Figure 11, Figure 12 & Figure 29). Basal contacts display deformational truncation and shearing of underlying units while the upper contacts are undulating creating a concave-like depression that is filled by bedded diamictites (Facies D) (Figure 11). The deformed bedded sandstones are thick bedded (10 to 50 cm) (Figure 29 & Figure 30) internally massive, fine to medium grained sandstones with outsized clasts. Stratification of the beds of sand is present in some of these deformed blocks (Figure 30). Clasts occur and range in size from coarse sands to cobble sized particles, and clast composition varies between feldspar, sandstone, greywacke and abundant quartz. Soft-sediment deformation occurs in this facies as the large folded and imbricated stacked blocks of sandstone throughout section AG4 (Figure 28 & Figure 30).

The second deformation style for Facies E occurs, as internally deformed stacked bodies (Facies Eb), found in sections AG2 and AG5, the two southern most measured sections (Figure 11 & Figure 12). This unit reaches up to 8 m in thickness and occurs laterally adjacent to other

sandstones (Facies C) and diamictites (Facies D) (Figure 12). These sandstone bodies are separated by low angle listric shaped thrust faults, or glide planes (Figure 31, Figure 32 & Figure 33). The planes are cm to dm thick and are characterized by fissile and boudinaged sandstones and shales. Facies Eb is commonly interstratified with Facies B. Basal contacts are deformational (listric-shaped surfaces) and the upper contacts are undulating and erosional and the units are laterally discontinuous.

In section AG2, the internally deformed stacked bodies of Facies Eb display undulating upper contacts with depositional relief filled in by bedded diamictites facies (Facies D). The bodies of Facies Eb were deposited as very fine to medium-grained sandstones with outsized clasts. Internal stratification is present but poorly preserved and highly deformed (Figure 31 & Figure 32). Clasts range in size from sand to cobble and composition on the individual clasts range from feldspar, sandstone, greywacke and abundant quartz. Rip-up shale clasts are also present. Internal soft-sediment deformation in this facies includes folding (Figure 34). Sandstone bodies display upturned edges, are truncated by overlying blocks or display various geometries of folding, which occur as asymmetric overturned, recumbent and isoclinal geometries (Figure 31 & Figure 32) (Benn & Evans, 1998).

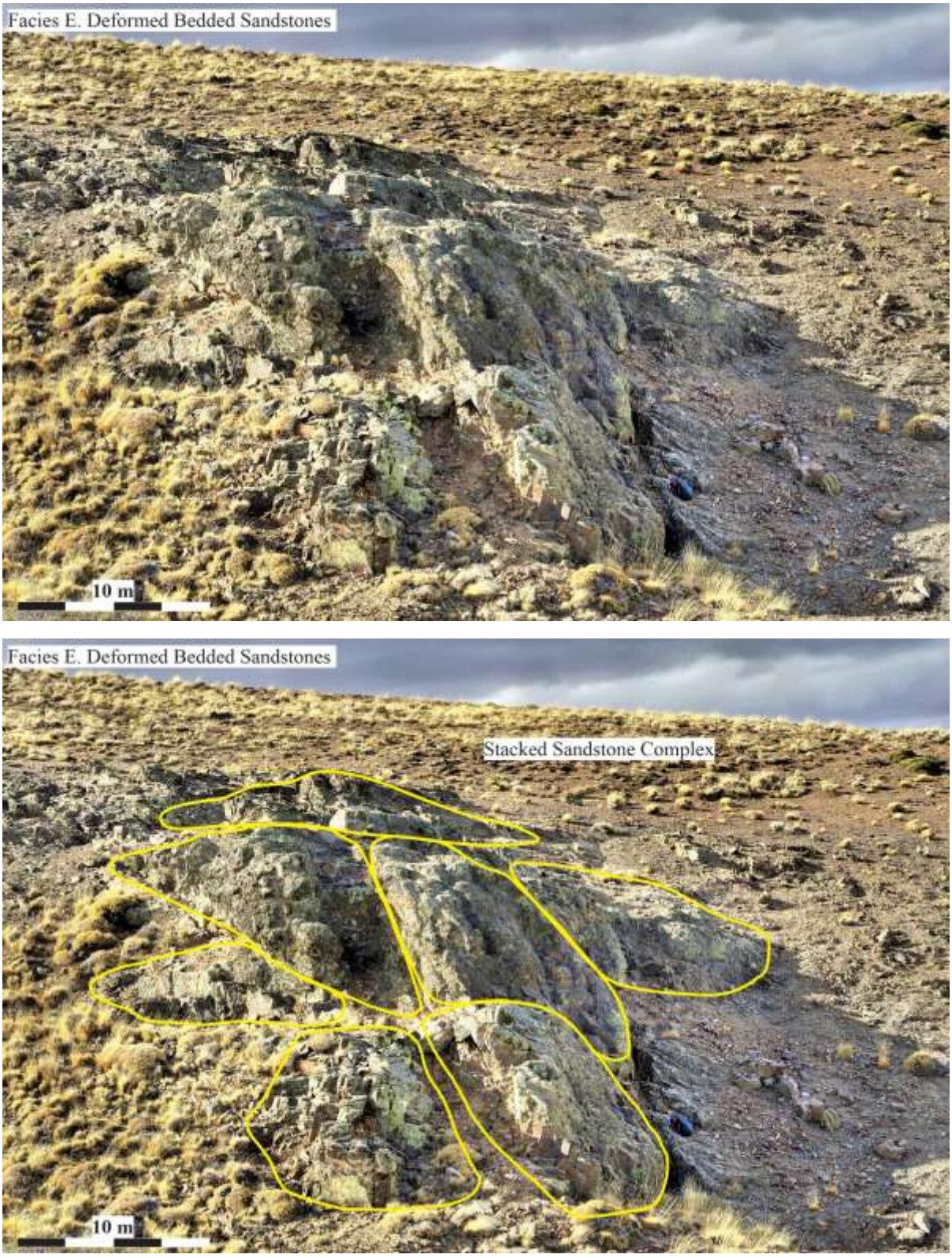

Figure 28 Facies Ea showing deformed bedded sandstones occurring as stacked blocks with minimal internal deformation. Foreground scale is shown, blocks in the background reach heights of ~9m. Individual blocks reach up to ~9m x ~9m.

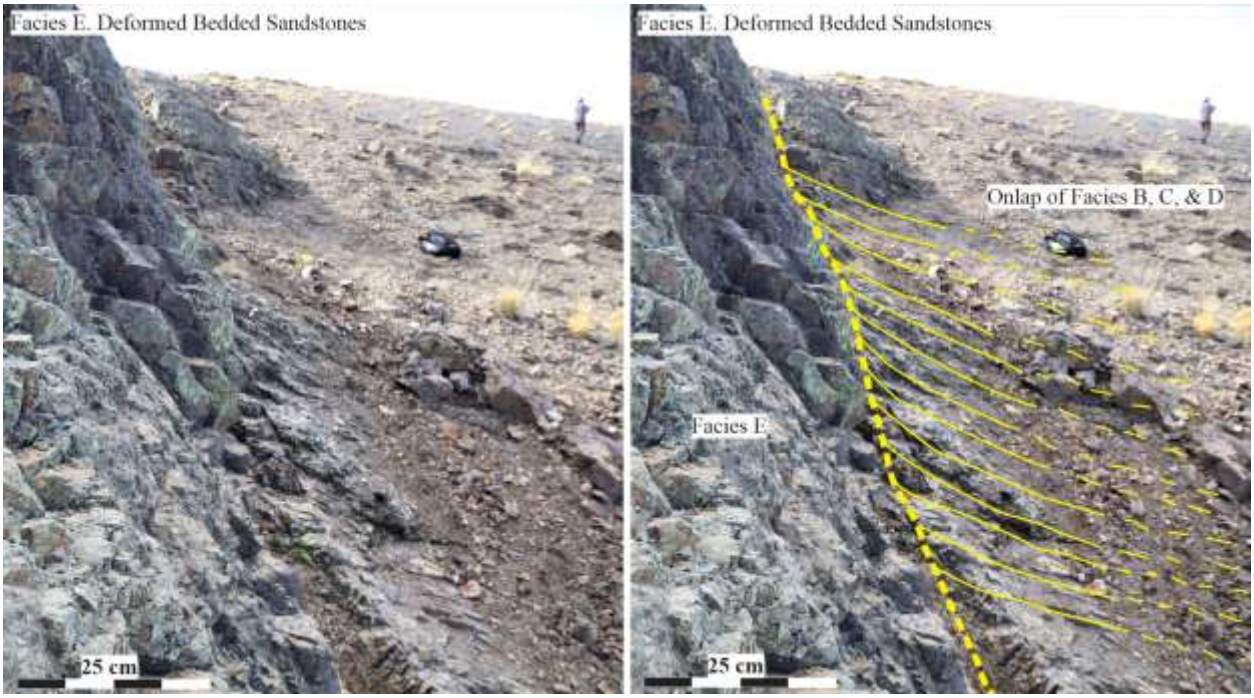

Figure 29 Facies Ea showing horizontal bedding of the sandstones (left) and their interfingering relationship with Facies C and Facies D (right) that lap onto Facies Ea. Scale is for the photo's foreground, person for scale in the background.

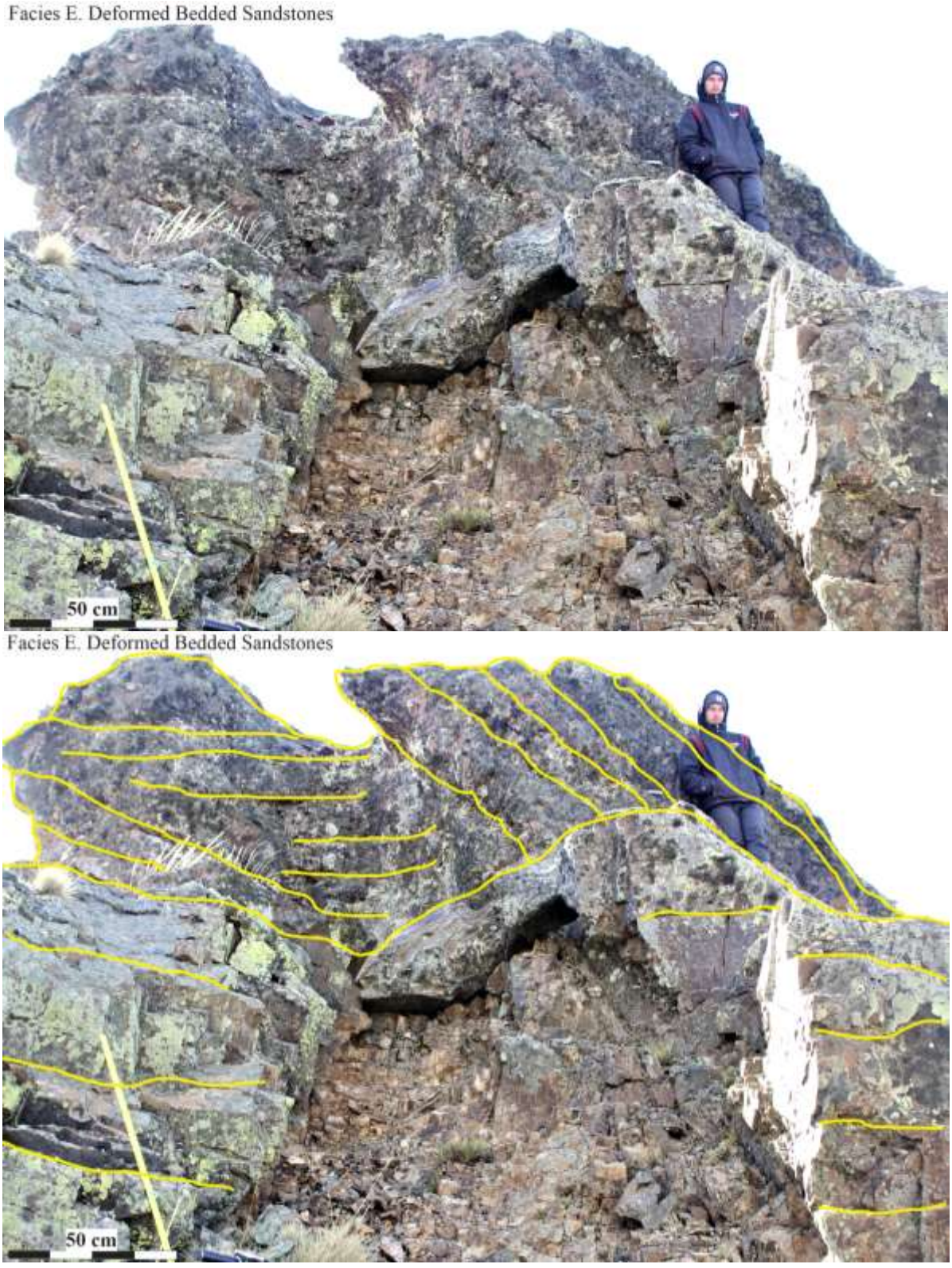

Figure 30 Facies Ea showing stacked blocks of sandstone, occurring in section AG4. The bedding of the massive sands (10-50 cm thick) is present here.

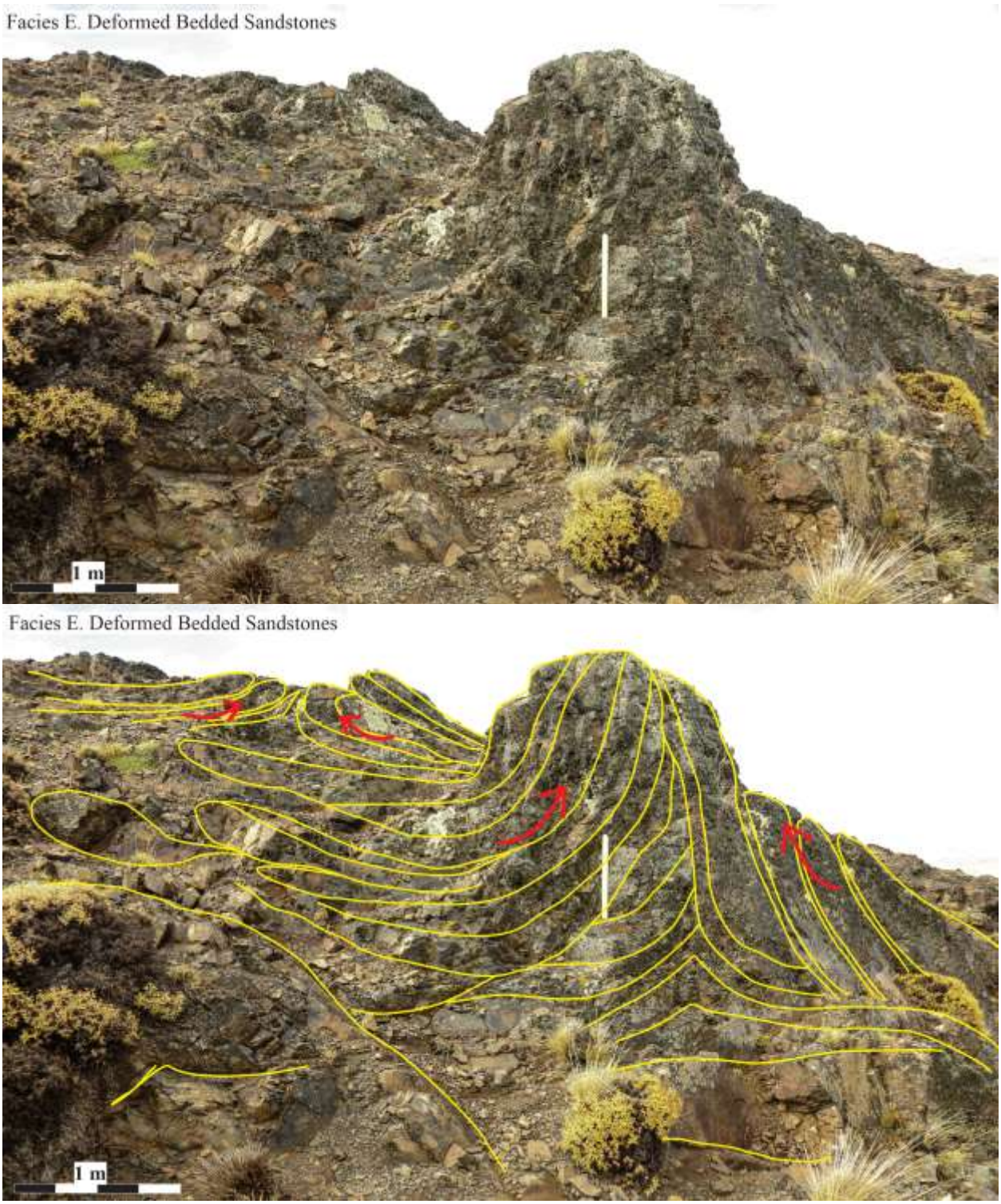

Figure 31 Facies Eb showing the upturned edges of the deformed bodies of sandstone and the poorly preserved internal bedding.

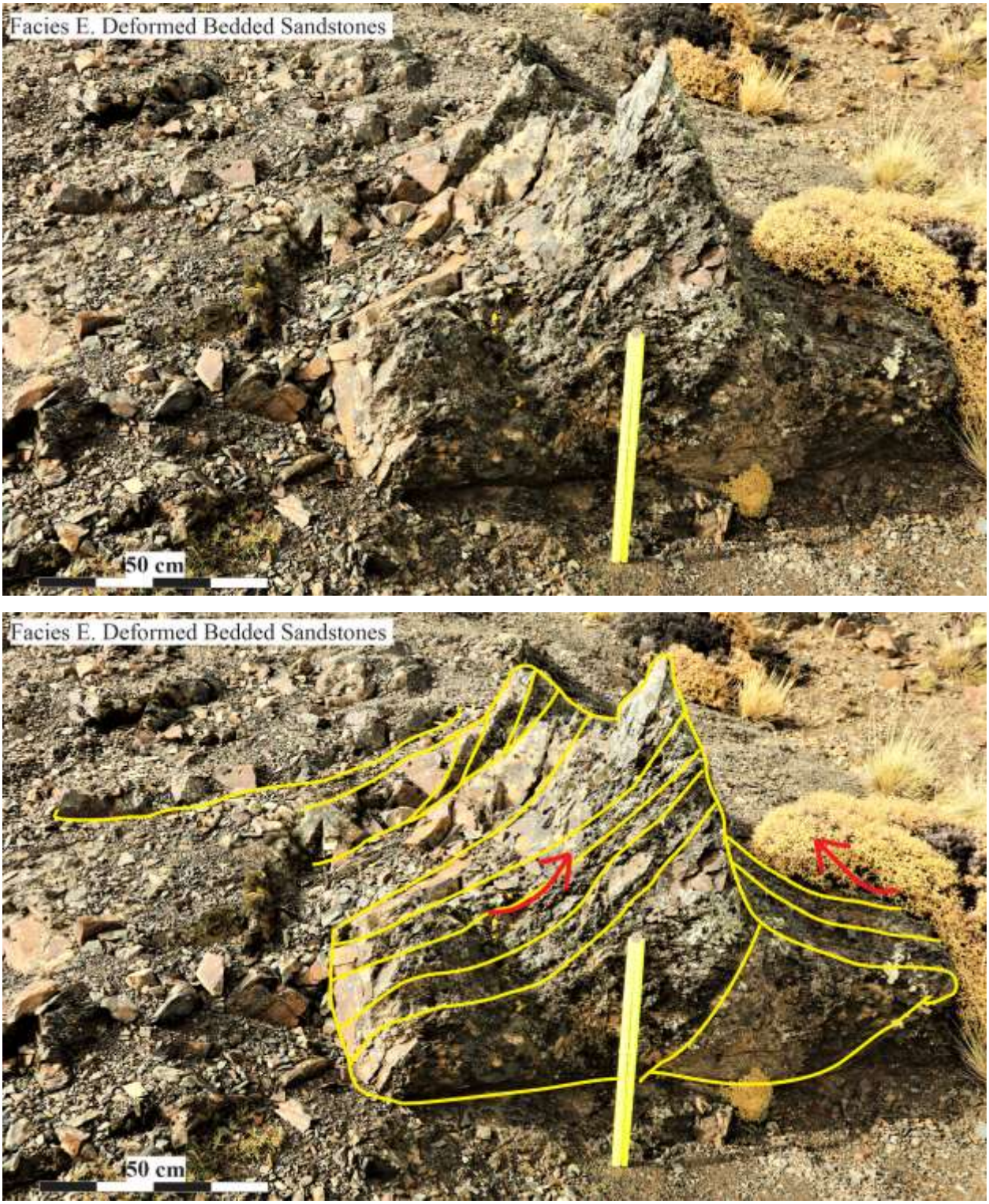

Figure 32 Facies Eb showing upturned edges, poorly preserved bedding and shearing of the interstratified Facies B, laminated mudrock with dispersed clasts.

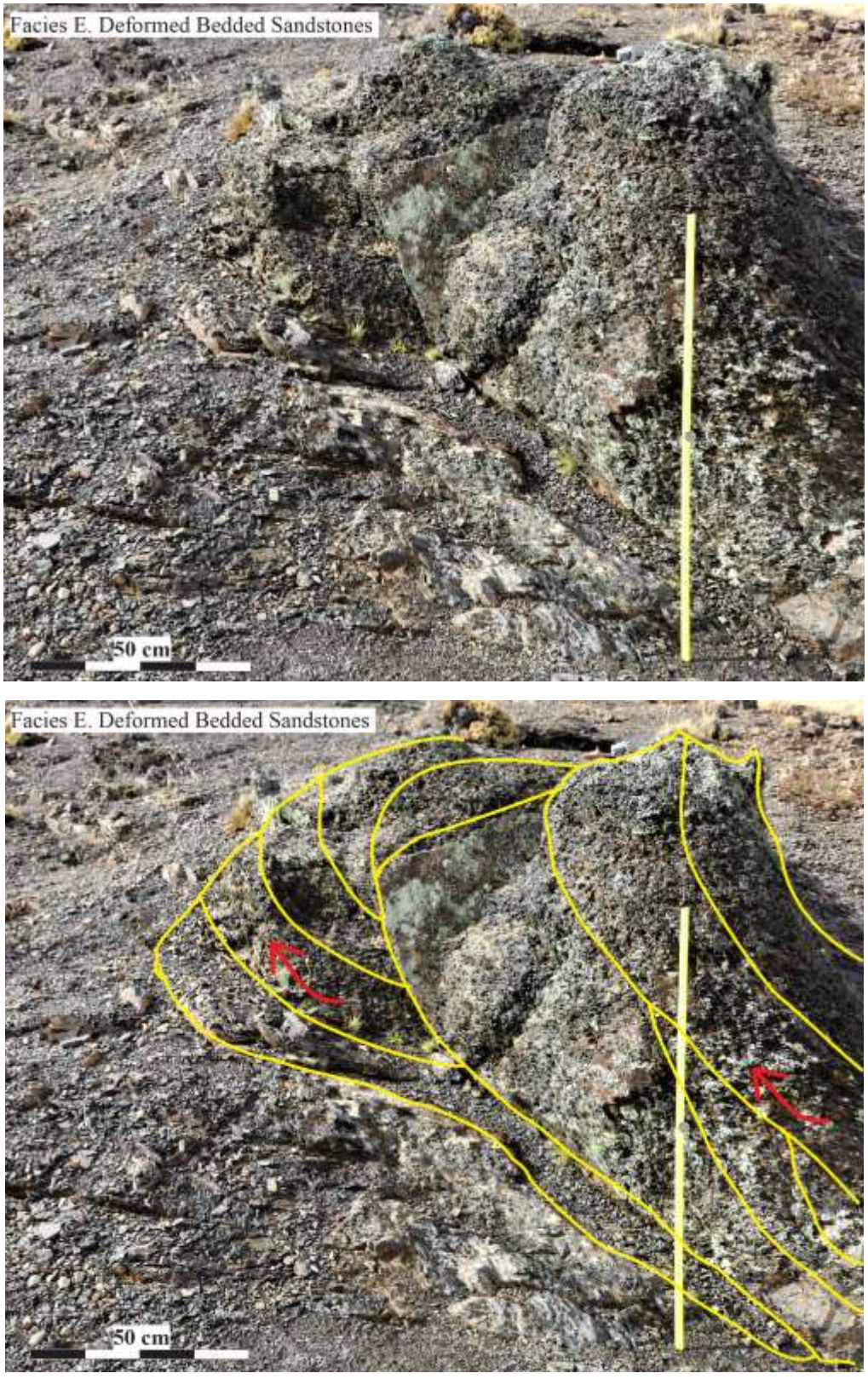

Figure 33 Facies Eb showing shearing with interstratified Facies B and thrusting deformation.

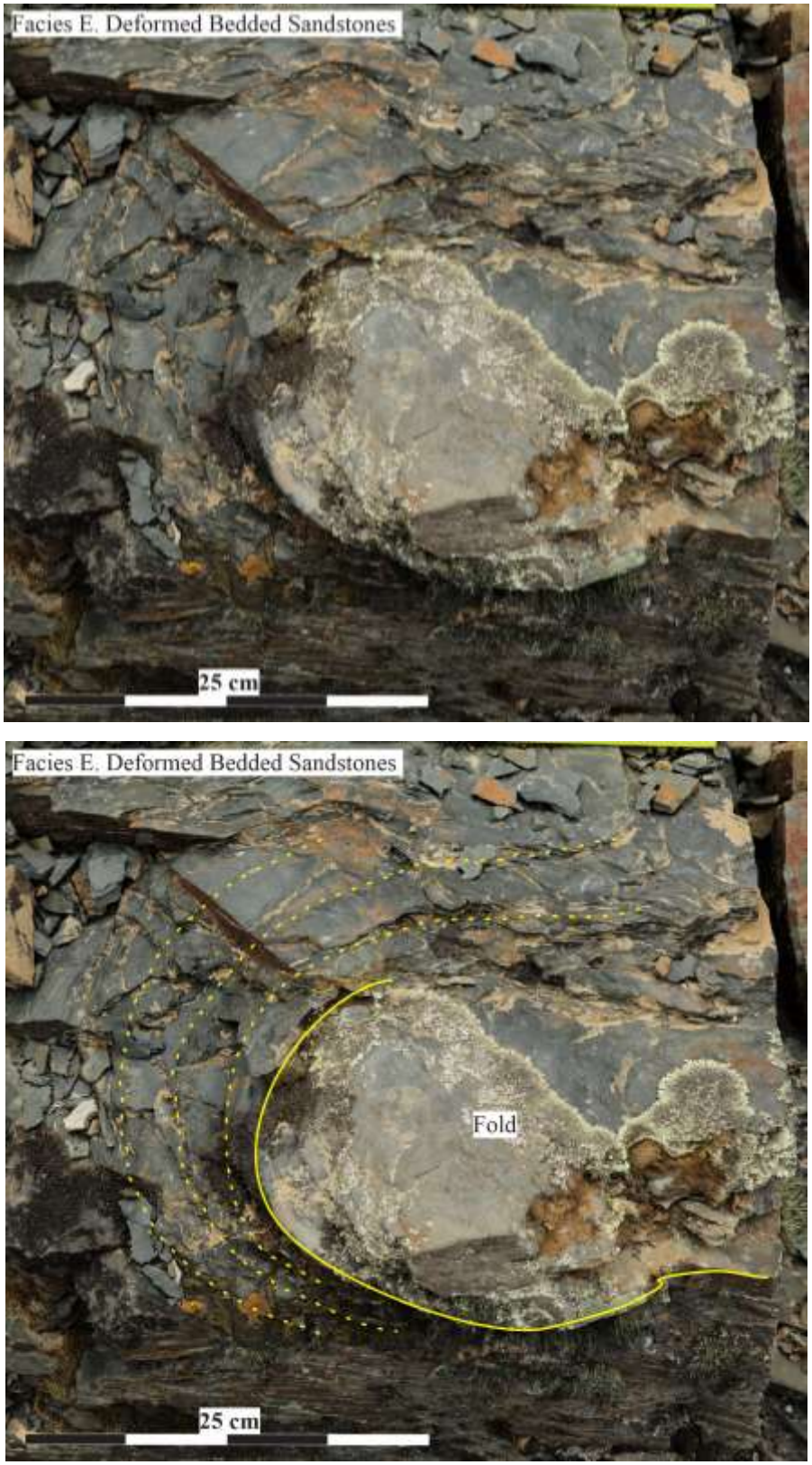

Figure 34 Facies Eb showing soft-sediment deformation, in the form of a fold nose and shearing, interstratified with Facies B.

6.E.2 INTERPRETATION: Facies E is interpreted as slide and slumped blocks (mass transport complexes) that formed from mass movement on an unstable dipping surface. The sand bodies rest on sheared surfaces that are represented by fissile shale and boudinaged sandstone. The upturned leading edge of these blocks suggest that they were emplaced by sliding over pre-existing strata (Woodcock, 1979; Martinsen, 1989, Posamentier & Martinsen, 2011).

The discontinuous nature of the bodies and their truncation by overlying bodies suggest that they formed as repeated episodic slide events where individual blocks were beginning to disaggregate (Pickering & Hiscott, 2016). Such blocks are termed slide blocks if they are relatively undeformed internally and are classified as slumps if internal deformation predominates (Shanmugan,1996). Both are forms of mass transport deposits and stacked bodies indicate the occurrence of mass transport complexes (Mulder & Alexander, 2001; Martinsen & Posamentier, 2006). Their occurrence suggests instability farther upslope due to influx of clastics to a shelf edge, oversteepening of a delta front, sedimentation in front of a glacial grounding line system and/or numerous other causes (Lee et al., 2007). As mass transport blocks disaggregate, they generate linked sediment gravity flows (debris flows, high density flows and turbidity currents; Martinsen, 1989, Posamentier & Martinsen, 2011, Pickering & Hiscott, 2016).

7. PALEO-SLOPE & PALEO-FLOW RESULTS & DISCUSSION

The orientation of listric-shaped thrust faults were measured within the mass transport deposits (Facies E, the deformed bedded sandstones facies) as well as deformation surfaces within the sediment gravity flows (Facies C, the graded sandstones, and D, the laminated and bedded diamictites) (Figure 11 & Figure 12). These surfaces represent the best general sediment transport directions for any strata within the basin. A total of 26 thrust fault/glide plane measurements obtained from sections AG1, AG2, AG4 and AG5. These were used for paleo-slope reconstruction. Within section AG1, seven thrust fault measurements were taken between a stratigraphic height of 12 – 20 m. In section AG2, eight thrust fault measurements were taken between a stratigraphic height of 5 – 10 m. Section AG4 had eight thrust fault measurements between a stratigraphic height of 13 – 22 m. Lastly, within section AG5, three thrust fault measurements were taken between a stratigraphic height of 5 – 9 m.

The measurements of the thrust faults (their dip and dip direction) created a series of points which then could be used to generate a rose diagram showing vergence to the N/NW at 297.4° (Figure 35, individual field measurements and corrections can be found in Appendix B). The vergence is the sliding direction, which is given by measurements displayed on the rose diagram (Figure 35). This represents the paleo-transport direction of the mass transport deposits. The paleo-slope direction verges to the north/northwest which suggests sediment was sourced from the southeast being transported to the northwest (Figure 35).

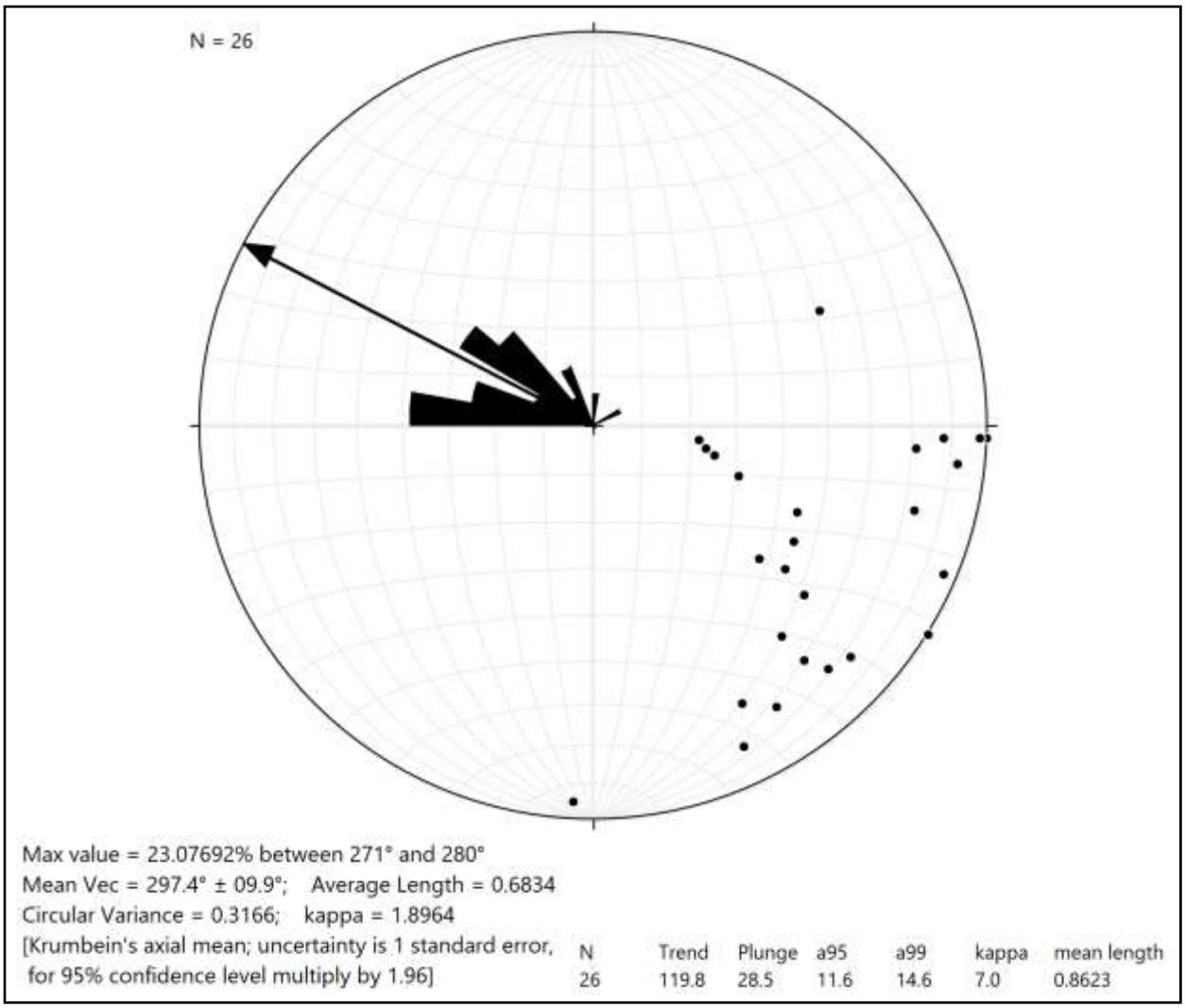

Figure 35 Stereonet showing the dip directions of dipping planes (dip of continental slope) and rose diagram showing the vergence, paleo-transport direction of sediment. Corresponding data and field measurements can be found in Appendix B.

Griffis et al. (2018) bases his hypothesis of a large ice sheet flowing east into and over the basin on a single paleo-flow direction which was measured in the underlying Pampa de Tepuel Formation (Gonzalez-Bonorino, 1992; Griffis et al., 2018) located 44 km to the east/northeast. The paleo-flow direction was taken from imbricated conglomeratic clasts. However, Gonzalez-Bonorino did not notice that these conglomerates were within a highly deformed set of beds (personal observation). The Pampa de Tepuel Formation is stratigraphically older than the Mojón

de Hierro Formation, which calls into question the use of the imbricated clast as representative for paleo-flow directions for the entire late Paleozoic Tepuel-Genoa Basin (Griffis et al., 2018). The data presented here indicates that the paleo-slope dipped towards the north/northwest at 297.4°. Such a paleo-slope is in a direct line with the Ellsworth Mountain block in the palinpastic maps shown in Figure 3 & Figure 4 (Lawver et al., 2008; Griffis et al., 2018).

8. LITHOFACIES DISCUSSION

Recognizing lithofacies and interpreting their depositional environment to develop conceptual models of deposition is fundamental to paleoenvironmental and palaeoclimatological reconstructions. Settling from suspension is the dominant form of sedimentation in the Mojón de Hierro Formation at Arroyo Garrido as indicated by the ubiquitous occurrence of mudrock (Facies A and B) (Freytes, 1971; Taboada & Pagani, 2010) both below and above the measured section. The absence of sandstones within the Facies A mudstones indicates long intervals when the basin was starved of coarse clastics (Figure 36). These conditions were interrupted by an interval of mass movement deposition during emplacement of Facies E slide and slump blocks. These blocks formed relief/topography on the depositional surface that influenced all subsequent sedimentation until the blocks were ultimately buried. This is indicated by onlap of all other facies (A through D) onto the edges and tops of Facies E bodies (Figure 36). This onlap also indicates that the sand blocks were emplaced prior to the deposition of the other facies (B, C, & D).

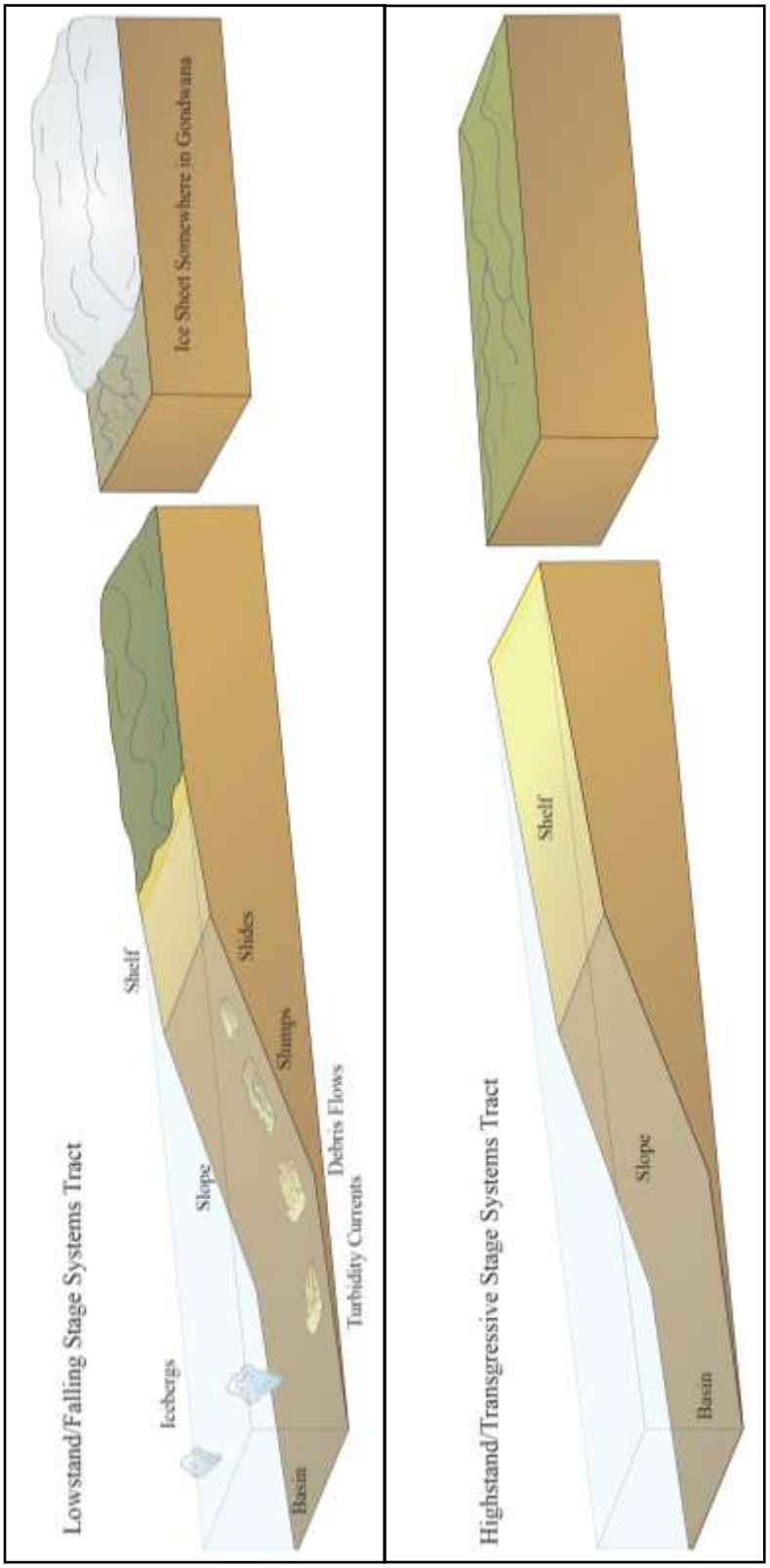

Figure 36 Schematic diagrams of the paleo-depositional environment of Arroyo Garrido. Left- represents a lowstand when Facies B, C, D & E were deposited. Right- represents a highstand when Facies A was deposited.

Sediment gravity flows (Facies C and D), along with hemipelagic sedimentation (Facies B), filled in the relief between these blocks. This suggests that these blocks formed small ponded basins on the slope and basin floor (cf. Posamentier, 2006; Artmitage et al., 2009). The laminated and bedded diamictites facies (D) and graded rhythmites facies (C) are in close proximity throughout the ponded stratigraphic interval (Figure 12) suggesting that they were spatially and temporally linked. Sediment gravity flows and mass transport deposits often occur in close proximity to each other (Carto & Eyles, 2012; Talling et al., 2012), and the onlap of Facies B, C and D onto Facies E mass transport blocks along with slump folds (Z folds) displaying apparent vergence opposite the regional slope and away from the sandstone block in section AG4 suggest that some of the sediment gravity flows could have been shed from these blocks of sediment (Armitage, 2009; Milana, 2019; Posamentier & Martinsen, 2011). Subaqueaous debris flows can transform into turbidity currents and turbidity currents can be shed due to the mixing of these flows with bottom waters (Hampton, 1972; Sohn et al., Haughton et al., 2003; Talling et al., 2012; Carto & Eyles, 2012). Following cessation of this interval of mass movement and sediment gravity flows, any relief on the depositional surface was passively filled in by deposition of Facies A as it onlapped and draped over remaining relief from the Facies E blocks.

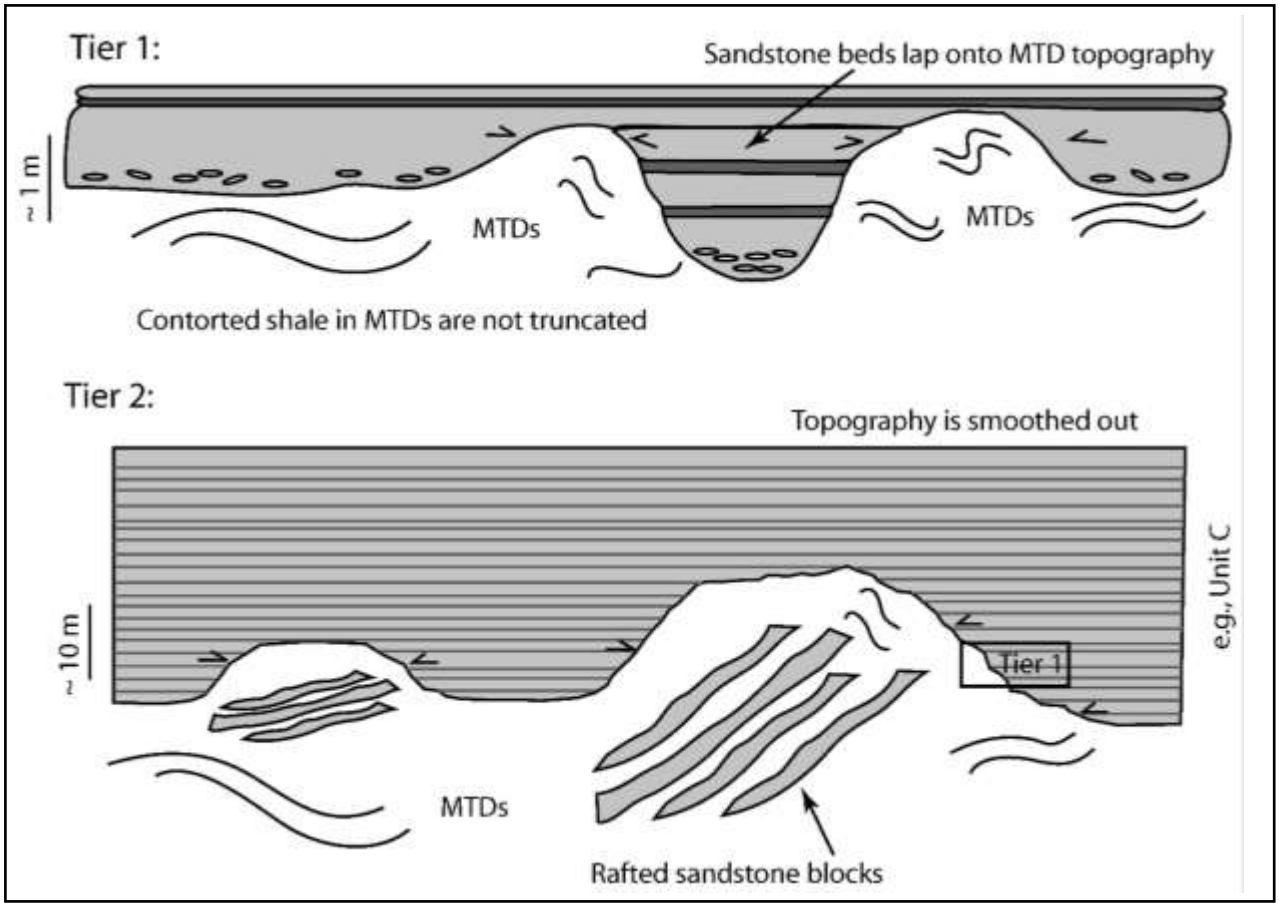

Figure 37 Schematic diagrams of mass transport deposits creating ponded mini basins. Tier 1 shows meter-scale and Tier 2 shows 10's of meters scale of mini basins ponded within mass transport deposits (modified from Armitage et al., 2009).

The depositional environments of the Arroyo Garrido strata are interpreted to be part of a marine basinal slope environmental system (Figure 36). Settling from suspension is the dominant form of sedimentation in the Mojón de Hierro Formation at Arroyo Garrido as indicated by the occurrence of thick mudstones (>100 m thick successions) throughout the succession (Figure 8; Freytes, 1971; Taboada & Pagani, 2010). The absence of any sedimentary structures produced by wave activity (hummocky cross stratification and asymmetrical ripples) within the entire measured outcrop indicates that sediment was deposited in deep-water well-below storm wave base and far from an active input of coarse clastics. Facies A mudstones suggest distal fine-grained deposition

during a relative sea-level transgression or highstand (transgressive and/or highstand systems tracts) when coarse clastics were trapped in nearshore environments high on the basinal shelf (cf. Catuneanu, 2006; Miall, 1997).

The occurrence of mass transport (Facies E) and sediment gravity flow deposits (Facies C and D) suggests that the introduction of coarse clastics into the distal basin occurred at a time when the shoreline had transited the shelf and deposited sediment at the shelf slope break. Mass movement in the form of slides and slumps (Facies E) and sediment gravity flows including debris flows (Facies D) and turbidity currents (Facies C) are triggered by a number of processes (e.g., seismic activity, rapid deposition on slopes, storm activity, liquefaction of over pressurized water-saturated sediment) that send unstable sediment down the slope into the deeper basin. Such deposits characterize times of falling relative sea levels (falling stage system tract) and or deposition during a relative sea-level lowstand (lowstand system tract; cf. Posamentier & Kolla, 2003; Posamentier and Walker, 2006; Lee et al., 2007).

The outsized clasts within Facies B through E (most noticeably in C and D) that bend and penetrate the underlying strata are interpreted as dropstones rafted by icebergs sourced from a distant ice front during glacial maximum and sea-level lowstand (Figure 36) (Thomas & Connell, 1985; Gilbert, 1990; Woodward, Lynas & Dowdeswell, 1994; Powell & Domack, 2002). The dropstones in these facies indicate that there was some glaciomarine influence at the time of deposition of Facies B through E. The size of the dropstones increases from Facies B to Facies C, which could mean more abundant and/or larger icebergs traveling and carrying a larger load of sediment. The roundness observed among the clasts could have resulted from glacial abrasion or reworking of pre-existing deposits by advancing ice. However, no striations were observed on any

of the outsized clasts. The absence of dropstones in Facies A suggests an absence of glaciers feeding sediment directly to the Tepuel-Genoa Basin during sea-level highstand.

The paleo-slope data indicates a paleo-flow direction towards the north/northwest (297.4°; Figure 35), and the lithofacies analysis does not indicate any evidence for a large ice sheet extending to the the Tepuel-Genoa Basin or the Panthalassan Margin during deposition of the Mojón de Hierro Formation as previously hypothesized. However, the ice rafted debris indicate that a distal glacier source is feeding icebergs that transited the basin. All of the characteristics of the Mojón de Hierro deposits indicate that strata at Arroyo Garrido study site were not deposited on a shallow-water shelf (cf. Taboada et al., 2009; González and Saravia, 2010), but instead were deposited beyond the shelf edge on the slope and basin floor (Figure 36).

9. MINERALOGICAL & GEOCHEMICAL ANALYSIS

9.1 X-RAY DIFFRACTION RESULTS:

XRD analysis was conducted on three samples (AG1-3, AG1-27, AG2-7) to determine the relative mineral abundances, summarized in Table 3 (complete XRD plots and information are in Appendix C). Sample AG1-3 (the stratigraphically oldest sample) has quartz (abundant), illite (present), albite (detected) and montmorillonite (detectable). Sample AG1-27 (the middle sample) has quartz (abundant), illite (present), and chlorite/serpentinite (present). Sample AG2-7 (the stratigraphically youngest sample) has quartz (abundant) illite (present), kaolinite (detectable), and montmorillonite (detectable).

XRD analysis indicated that quartz, albite and illite were present within each of the three samples. In all three samples quartz is abundant. Illite is abundant in one sample and present in the other two. Montmorillonite was detectable in two of the three samples. Chlorite/serpentinite was present in only one sample. Kaolinite was detectable in only one sample. Albite was detected in only one sample.

Table 3 X-ray diffraction results showing the samples and their mineralogical composition.

X-ray Diffraction Data						
Sample Name	**Quartz**	**Albite**	**Chlorite/ Serpentinite**	**Illite**	**Montmorillonite**	**Kaolinite**
AG1-3	Abundant	Detected	-	Present	Detectable	-
AG1-27	Abundant	-	Present	Abundant	-	-
AG2-7	Abundant	-	-	Present	Detectable	Detectable

9.2 X-RAY DIFFRACTION DISCUSSION:

XRD results indicate that the clays within the deposits are not highly altered. Quartz is the predominant mineral in all of the samples. There is no gibbsite, which is the final clay alteration mineral, present in the samples. Kaolinite is only present in one of the samples (AG2-7) which is stratigraphically the youngest sample. XRD information suggests moderate weathering.

9.3 X-RAY FLUORESCENCE RESULTS:

Major elements were analyzed by XRF on thirteen samples collected from the measured sections. The major oxide concentrations varied in the studied samples (Table 4). The samples contain 0.21-1.17 wt% Na_2O (with an average of 0.65 wt%), 1.49-2.17 wt% MgO (with an average of 1.90 wt%), 13.18-18.59 wt% Al_2O_3 (with an average of 15.74 wt%), 60.26-70.44 wt% SiO_2 (with an average of 65.36 wt%), 0.14-0.17 wt% P_2O_5 (with an average of 0.16 wt%), 2.72-4.49 wt% K_2O (with an average of 3.46 wt%), 0.29-0.46 wt% CaO (with an average of 0.38 wt%), 0.76-0.94 wt% TiO_2 (with an average of 0.86 wt%), and 4.62-7.82 wt% Fe_2O_3(with an average of 6.09 wt%).

The Arroyo Garrido mudstones were compared to Post-Archean Australian Average Shale (PAAS) and Upper Continental Crust (UCC) values (McLennan & Taylor, 1985), shown in Table 4 (and plotted on Figure 39). The major oxide sample average shows an overall elevations of SiO_2 (65.4%) compared to PAAS values (SiO_2; 62.8%). Concentrations of P_2O_5 (0.16%) were similar to the PAAS values (P_2O_5; 0.16%). The average oxide concentrations are only slightly reduced in TiO_2 (0.9%), K_2O (3.5%) and MgO (1.9%) compared to PAAS averages (K_2O; 3.7%, MgO; 2.2% and TiO_2; 1.0%). Average concentrations of Al_2O_3 (15.7%), Fe_2O_3 (6.09%), CaO (0.4%) and Na_2O

(0.6%) show more significant reductions compared to PAAS values (Al_2O_3; 18.9%, Fe_2O_3; 7.22%, CaO; 1.3% and Na_2O; 1.2%).

When average trace element concentrations are compared to the PAAS values (V; 150 PPM, Cr; 110 PPM; Zn; 85 PPM, Sr; 200 PPM, and Y; 27 PPM Zr; 210 PPM, and Ba; 650 PPM) elevation is seen in V (154 PPM), Zn (106 PPM), and Y (39 PPM), while reductions are seen with Cr (75 PPM), Zr (177 PPM), Sr (35 PPM), and Ba (542 PPM) when compared to PAAS values (Table 4). In addition, major and selected trace elements were compared to UUC values, which shows the average sample values have higher elevations in Al_2O_3 (15.7%), TiO_2 (0.9%), Fe_2O_3 (6.1%) and K_2O (3.5%), and show reduced values in SiO_2, MnO, CaO, MgO, and Na_2O.

Table 4 Table of XRF data, major oxide concentrations are expressed as weight percent (wt %) and trace element concentrations are expressed in parts per million (PPM), (*) indicates values that are just below twice the LLD.

Sample	AG1-1	AG1-3	AG1-LAM	AG1-6	AG1-8	AG1-9	AG1-27	AG2-2	AG2-3	AG2-4	AG2-5	AG2-6	AG2-7	Average	PAAS	UCC
SiO2 (%)	67.04	68.57	62.65	61.04	66.65	65.01	63.93	60.26	63.69	65.56	65.13	70.44	69.71	65.4	62.8	66
Al2O3 (%)	13.18	13.91	17.40	18.15	15.72	16.32	16.74	18.59	16.37	15.73	15.08	13.69	13.75	15.7	18.9	15.2
TiO2 (%)	0.80	0.76	0.89	0.94	0.83	0.92	0.85	0.90	0.89	0.91	0.89	0.81	0.81	0.9	1	0.5
Fe2O3 (%)	7.82	5.23	6.48	6.52	5.25	5.88	6.36	6.72	6.43	6.12	6.97	4.62	4.83	6.09	7.22	5
MnO (%)	0.08	0.08	0.07	0.07	0.04	0.07	0.06	0.07	0.08	0.05	0.07	0.04	0.03	0.06	0.11	0.08
CaO (%)	0.29	0.43	0.39	0.43	0.36	0.46	0.34	0.36	0.41	0.34	0.41	0.34	0.35	0.4	1.3	4.2
MgO (%)	1.49	1.63	2.17	2.16	1.74	1.98	2.13	2.15	2.14	1.99	1.93	1.58	1.60	1.9	2.2	2.2
Na2O (%)	0.78	1.17	0.61	0.73	0.53	0.69	0.50	0.21	0.48	0.66	0.97	0.80	0.32	0.6	1.2	3.9
K2O (%)	2.72	3.07	4.02	4.17	3.56	3.66	3.85	4.49	3.33	3.42	3.18	2.72	2.81	3.5	3.7	3.4
P2O5 (%)	0.15	0.14	0.16	0.16	0.16	0.19	0.16	0.16	0.14	0.17	0.17	0.17	0.17	0.16	0.16	
L.O.I.	3.58	3.27	4.04	4.29	3.73	3.63	3.66	4.32	4.30	3.53	3.65	3.36	3.60			
Total %	98.06	98.36	99.01	98.8	98.69	98.94	98.71	98.38	98.38	98.6	98.57	98.69	98.08			
V PPM	130	130	176	180	140	164	174	177	160	146	155	130	139	154	150	60
Cr PPM	58	50	100	88	58	71	70	88	80	84	79	70	81	75	110	35
Zn PPM	100	80	100	125	124	70	143	126	70	117	134	117	70	106	85	71
Y PPM	39	32	45	41	39	42	41	43	40	39	34	36	40	39	27	22
Zr PPM	221	219	165	176	216	223	154	140	135	151	163	173	166	177	210	190
Ce PPM	51	49	55	60	55	64	54	64	51	49	54	44	50	54		
Sr PPM	36	37	31	38	30	29*	30	35	27*	29*	43	38	35	35	200	350
Ba PPM	485	427	646	632	577	532	549	732	545	506	520	451	442	542	650	550
CIA %	73.4	69.8	74.2	73.7	74.5	73.3	74.9	76.0	76.1	74.4	72.3	73.7	76.6	74.1		
V/Cr	2.2	2.6	1.8	2.0	2.4	2.3	2.5	2.0	2.0	1.7	2.0	1.9	1.7	2.1		

9.4 X-RAY FLUORESCENCE DISCUSSION

CHEMICAL INDEX OF ALTERATION (CIA):

CIA results indicate that the degree of the sediment source weathering varies slightly in the thirteen samples analyzed ranging from 70 to 77, with an average of 74 (Figure 38), which falls in the range of average marine shale CIA values (70-75; Nesbitt & Young, 1985; Goldberg, 2001). Environments where mechanical weathering is dominant (arid settings) have lower ranges of CIA values between 50-70 (Goldberg & Humayun, 2010) and environments where chemical weathering is dominant (humid/tropical settings) have higher CIA values of 80-100. Average marine shale values range from 70-75 (Taylor & McLennan, 1985; Goldberg & Humayun, 2010).

CIA values from strata in the Mojón de Hierro Formation suggest that the mud is coming from a temperate terrestrial source that was not exclusively weathered by mechanical or chemical processes. These values are within associated values of average shale CIA values (Passchier, 2011). CIA values only show minor local variations within the section, but are still within the range of average marine shale CIA values (Figure 38). CIA values plotted on the A-CN-K (Al_2O_3, CaO^*+Na_2O & K_2O) ternary diagram (Figure 39) show that weathering has occurred and follows a similar trendline of granite weathering (Nesbitt & Young, 1989) and plot near PAAS values (Condie, 1995).

The data strongly suggest that the introduction of meltwater plumes emanating from glacial sources of meltwater were not a major influence of sedimentation in the basin at the time of deposition of the Mojón de Hierro Formation, otherwise, physical weathering of source rocks would have produced lower CIA values. However, ice rafted debris does occur with the measured

sections and the CIA analysis supports that the iceberg rafting was coming from a distant source and that no significant glacial source was directly influencing the basin.

The CIA data indicate that the muds did not have a source that was solely mechanically weathered. Mechanical weathered materials would be expected if there were glaciers present in the source area along the basin margins. The CIA data also indicate that the source area is not entirely originating from intense chemical weathering, which would be seen if the source area was in a humid environment. The CIA resemble temperate terrestrial sources producing and supplying muds to a marine basin. CIA does not show any apparent trends or flucuations throughout the 48 m of stratigraphic elevation (Figure 38) and the CIA values plot close to the PAAS values on the A-CN-K diagram (Figure 39) suggesting values similar to average marine shales with sediment sources that are of temporate terrestrial sources (Goldberg, 2001; Passchier, 2011).

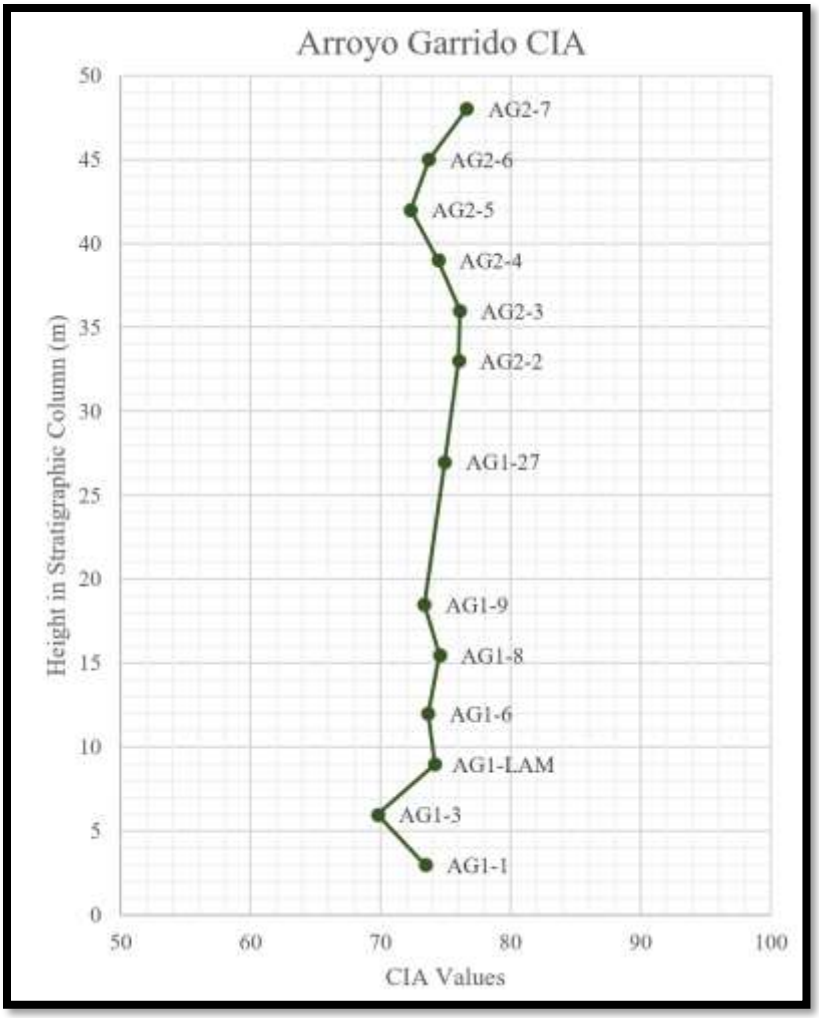

Figure 38 CIA values of the Mojón de Hierro Formation at from samples at Arroyo Garrido, with relation to stratigraphic elevation. Values range from ~70 to 77 which are similar to marine shale averages (Goldberg, 2001; Passchier, 2011).

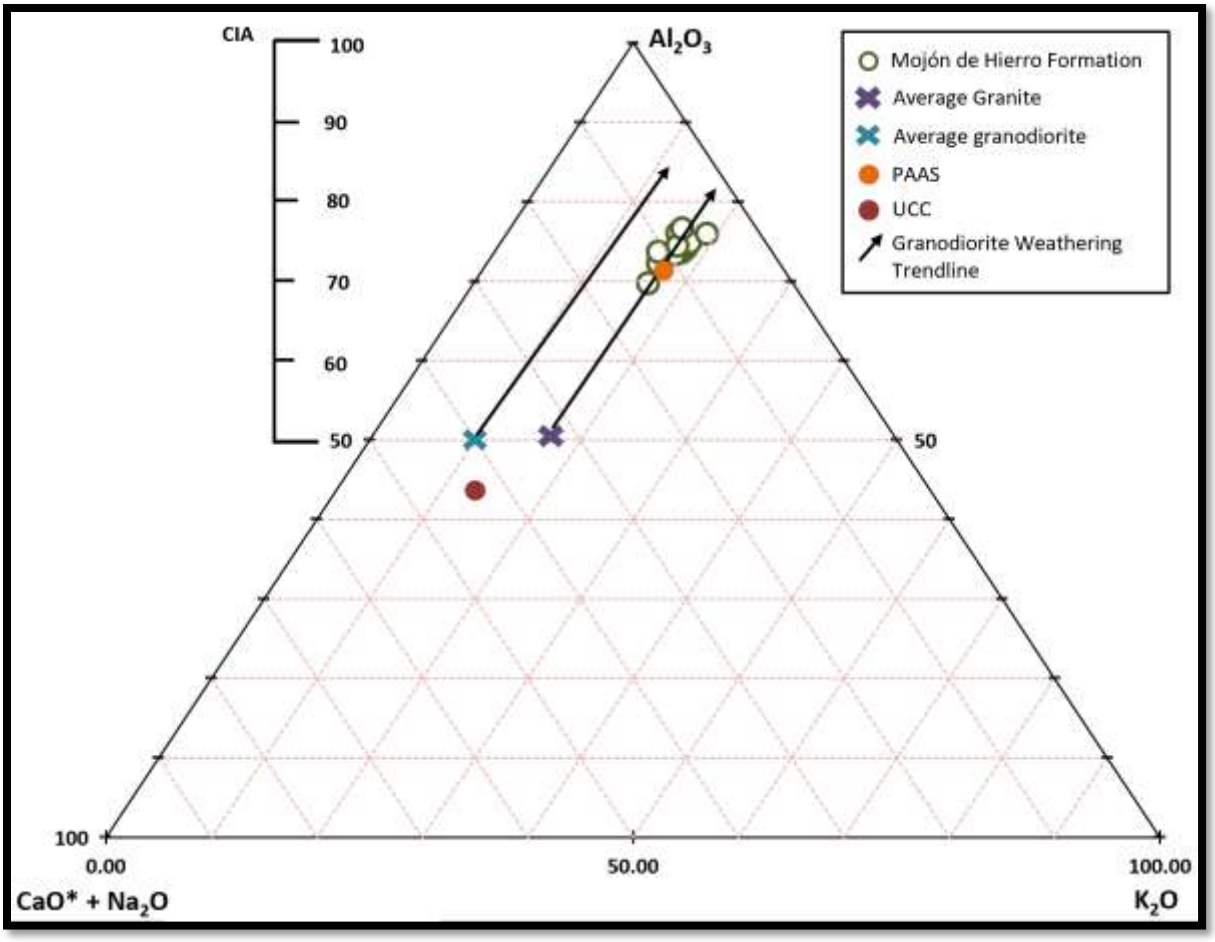

Figure 39 A-CN-K tertiary diagram indicating values of average granites and granodiorites, weathering trends of average granite and granodiorite (Nesbitt & Young, 1989), values of UCC and PAAS (McLennan & Taylor, 1985), and the Arroyo Garrido sample values. CIA is plotted on top left.

VANADIUM/CHROMIUM (V/CR):

Trace element concentrations were measured using XRF spectrometry and the results of the analyzed samples have only slight variations up the stratigraphic column (Table 4 & Figure 40). Trace element concentrations ranged: V from 127 to 180 PPM and Cr from 50 to100 PPM. The results of V/Cr ratios ranged from 1.7 to 2.6 (Figure 40), with an average of 2.1. The V/Cr ratios indicate oxic (<2) and dysoxic (2-4.25) waters (Figure 40; Jones & Manning, 1994).

Oxygen rich and dysoxic waters suggest that the depositional setting was an unrestricted marine environment with good circulation. The circulation and oxygenated water are interpreted to be brought in from general ocean circulation and perhaps through the introduction of mass transport deposits (slide/slump blocks) and sediment gravity flows (debris flows and turbidity currents; Figure 36). However, the V/Cr ratios display a slight increase in values for the samples collected at similar elevations to sandstones of Facies E. There is a slight decrease in values for the samples collected above the top of Facies E sandstone blocks. These local variations suggest that the sediment between the mass transport deposits (Facies E) was influenced by ponding of waters behind the block, which resulted from the mini basin created in the basinal slope environment by emplacement of the slide and slump blocks. The V/Cr variations indicate the ponding behind Facies E slightly influenced the circulation within the mini basin. Once the ponded mini basin was filled, regular patterns of circulation resume (Figure 40).

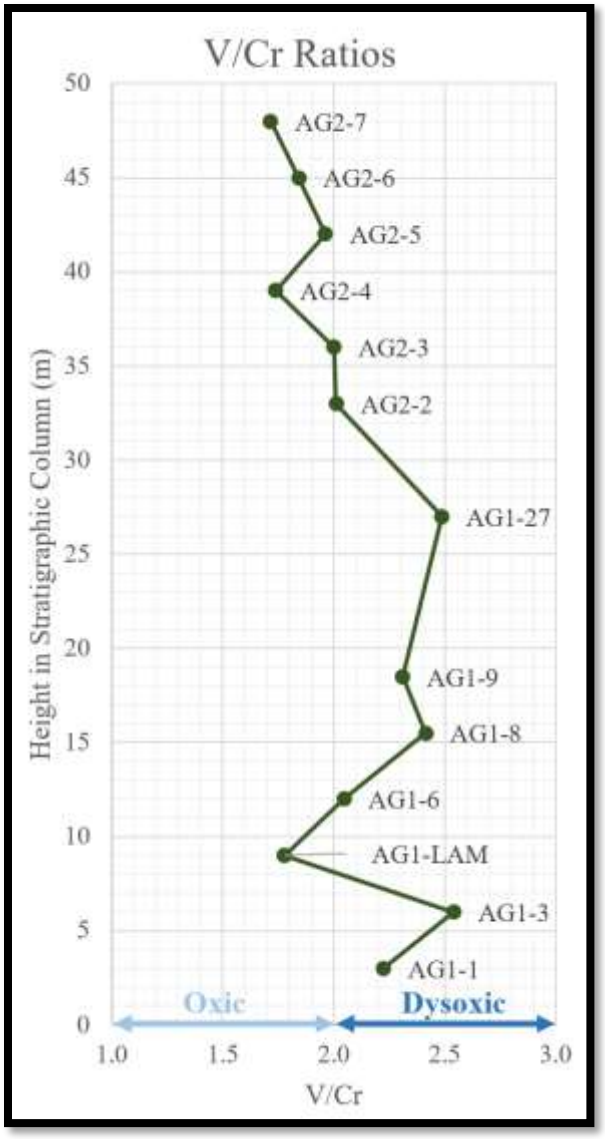

Figure 40 Vanadium/chromium ratios plotted against their stratigraphic elevation on the measured section. Values plot as oxic (<2) and dysoxic (2-4.25).

10. DISCUSSION OF GEOCHEMISTRY AND PALEOENVIRONMENT

The mud entering the basin is due to clastic influxes from terrestrial sources (i.e., prograding delta, prograding shelf). The Arroyo Garrido CIA values indicate average marine shale values and that the sediment source area was not exclusively being physically weathered nor chemically weathered, they indicate a temperate terrestrial source. This data does not present any evidence for large glaciers in the drainage basin directly supplying mud to the basin, lower CIA values would have been measured if there were. Therefore, ice-rafted debris in the sediment associated with the mass-transport and sediment gravity flows interval, deposited during either a forced regression or a relative sea-level lowstand, suggest that icebergs transiting the basin were far traveled from distal glaciers sourced from outside of the basin. Facies analysis plus CIA data do not indicate any evidence for a large glacier near the basin margin.

Overall the V/Cr ratios indicate the bottom waters were between oxic and dysoxic (Figure 40) (Ernst, 1970; Jones & Manning, 1994). There are minor local fluctuations in the V/Cr ratios values which varied due to the presence (and absence) of the deposits of Facies E being laterally adjacent to samples collected. Higher V/Cr values (dysoxic) are associated with the strata that are laterally adjacent to the mass transport deposits compared to strata sampled above the mass transport deposits (primarily oxic). This indicates that the sediment deposited after and ponded between Facies E blocks is more restricted (dysoxic) compared to the normal basin depositional conditions represented by Facies A (oxic).

Detailed facies analysis indicates a deep-marine basinal slope setting below storm wave base, which is indicated by the absence of wave produced sedimentary structures (hummocky cross stratification and asymmetrical ripples), the thickness of mudrocks, and the absence of shallow marine sands in the study area. The mud and fine-grained sediment settling from suspension are

background basin sedimentation conditions (highstand) and coarse clastic intervals in the basin were introduced by slide and slumped blocks, followed by sediment gravity deposits and ice rafted debris in a lower slope to basin floor setting (lowstand). Although the basin was not directly influenced by an adjoining ice front along the basin margin or up the drainage basin that supplied flowed into the basin, available data (facies analysis and CIA) does suggest that the Mojón de Hierro strata were influenced by distant ice (distal) in the form of ice-rafted debris and from the uptake of water by ice to cause a eustatic lowering of sea level. This data along with the bedded nature of the diamictites suggest that the diamictites were the result of mass transport deposits shed from a shelf edge and not from the advance of a glacier across the basin to the shelf edge as previously interpreted (Griffis et al., 2018). The outsized clasts that penetrate underlying stratification, interpreted as dropstones, were likely deposited by icebergs floating through the basin. The paleoenvironment is interpreted to be a basinal slope setting near an unstable shelf with distal glaciers in contact with water which is feeding icebergs that transited the basin. Paleo-flow indicates sediment transport direction is to the northwest (297.4°).

CIA results indicate average marine shale values and no evidence that they are highly physically weathered (characteristic of arid/glacial weathered muds) nor highly chemically weathered muds (characteristic of muds produced in humid/tropical settings). The absence of highly physical weathered muds indicates that there are no proximal glaciers feeding muds into the basin at the time the Arroyo Garrido strata were deposited. V/Cr ratios indicate oxic and dysoxic water conditions. Dysoxic values (slightly restricted) correlate to the deposition (and stratigraphic height) of the mass transport deposits and sediment gravity flows. Oxic (more open circulation) values correspond to Facies A, the normal basin conditions, prior to the burial of Facies E sandstone blocks and the smoothing of the seafloor.

In conclusion, there is no evidence that a large ice sheet reached the Panthalassan margin or of a proximal glacier to the Tepuel-Genoa Basin during the time the Arroyo Garrido strata were being deposited (Late Permian). However, there is evidence supporting distal ice as the source of icebergs that moved through the basin. This detailed sedimentological analysis opposes the detrital zircon analysis, which interprets a large ice sheet centered over the Ellsworth Mountains supplying sediment directly to the Tepuel-Genoa Basin and extending to the Panthalassan Margin. Icebergs can travel/deposit ice rafted debris thousands of kilometers away from glacial fronts, so glacially influenced does not necessarily mean nearby glaciers or the occurrence of a massive ice sheet.

11. CONCLUSION/SUMMARY

- Facies A, the laminated mudrock facies, represents normal basinal sedimentation conditions due to thickness and dominance of the mudrock units in the basin. Deposition occurred in deep water, below storm wave base, indicated by the absence of hummocky cross stratification and asymmetrical ripples.
- Facies E, deformed bedded sandstones, were deposited as mass transport deposits on a basin slope as slide and slumped blocks. These blocks were emplaced prior to the deposition of Facies B, C and D as these facies onlap the sides of the blocks.
- Facies B, the laminated mudrock with dispersed clasts facies, were deposited below storm wave base as evidenced by an absence of wave reworked features from the absence of hummocky cross stratification and asymmetrical ripples. Coarse clastics were introduced as ice rafted debris dropped into deep water from icebergs in a basinal slope environment.
- Facies C, the graded rhythmite facies were deposited in deep water below storm wave base. They were deposited from sediment gravity flows/turbidity currents. Outsized clasts that penetrate and bend underlain strata are interpreted as dropstones introduced by icebergs transiting the basin.
- Facies D, the laminated and bedded diamictites facies, were deposited as sediment gravity flows interpreted as debris flows. Facies C and D occur in close proximity and are commonly interstratified suggesting that they were spatially and temporally linked, which is common where there are unstable sediments nearby. Outsized clasts that penetrate and bend underlying strata are interpreted as dropstones.

- The paleo-depositional setting was a marine slope environment, near the toe of the slope-basin floor edge. No wave generated structures were observed throughout the entire measured section indicating deposition occurred below storm wave base.
- The deposition of the slide and slumped blocks created topography/relief on the slope-basin floor, resulting in a small ponded basin allowing for Facies B, C and D to be deposited within and eventually filled the depression. This coarse clastics interval indicates a sea-level lowstand during a glacial interval, which allowed coarse clastics from a nearby unstable shelf edge to be supplied to deeper water. This interval shows deposition was influenced by icebergs transiting the basin supplied from a distal ice margin.
- Once the ponded basin was filled, Facies A onlapped and draped over the relief/topography on the slope. This marks the return of normal basin conditions and sedimentation from settling from suspension and coarse clastics trapped in nearshore settings, during a sea level highstand.
- Paleo-flow direction was to the northwest at 297.4°.
- Mineralogy indicates the clays are moderately weathered.
- Major elemental data was applied to a paleo-weathering proxy, CIA, and indicate average marine shale values, showing that neither physical weathering nor chemical weathering was entirely dominant in the source sediment area. As well, CIA does not show any evidence of a large glacier or glacial meltwater plumes within the drainage basin that fed water or sediment directly into the depositional basin.
- Minor elemental data was applied to a paleo-oxygenation proxy using V/Cr ratios, and indicate dysoxic and oxic values. Results indicate the primarily dysoxic values are associated with the stratigraphic height of Facies E. The primarily oxic values are

associated with the deposition of Facies A. Linking the small ponded basin with a more restricted circulation compared to the open and leveled basin- conditions, suggesting that the relief/topography from the deposition of Facies E caused water circulation patterns to be temporarily restricted.

- This study shows no evidence of glacial activity within the basin or its related terrestrial drainage basin during deposition of the Mojón de Hierro Formation.

REFERENCES:

Allmendinger, R. W., Cardozo, N., & Fisher, D. M. (2011). *Structural geology algorithms: Vectors and tensors*. Cambridge University Press. http://www.geo.cornell.edu/geology/faculty/RWA/programs/stereonet.html

Andreis, RR, Archangelsky, S., González, CR, López Gamundi, O., Sabattini, N., Aceñolaza, G., ... & Cúneo, R. (1987). Cuenca Tepuel-Genoa. El Sistema Carbonífero en la República Argentina. Córdoba, Academia Nacional de Ciencias , 155-182.

Andreis, R. R., & Cúneo, R. (1985). Estratigrafía de la Formación Mojón de Hierro en Puesto Garrido, extremo sudoriental de la sierra de Tepuel, Chubut, Argentina. Reunión Anual Grupo Argentino de trabajo, Proyecto, 211, 22-24.

Andreis, R. R., & Cúneo, R. (1989). Late Paleozoic high-constructive deltaic sequences from northwestern Patagonia, Argentine Republic. Journal of South American Earth Sciences, 2(1), 19-34.

Andreis, R. R., Cúneo, R., Lopez Gamundi, O., Sabattini N & González, C., 1996. Cuenca Tepuel-Genoa. In: S. Archangelsky Ed, El Sistema Pérmico en la República Argentina y en la República Oriental del Uruguay. Academia Nacional de Ciencias, Córdoba, p. 65-91.

Azcuy, C. L., Beri, A., Bernardes-de-Oliveira, M. E. C., Carrizo, H. A., Di Pasquo, M., Díaz Saravia, P., & Pagani, A. (2007). Bioestratigrafía del Paleozoico Superior de América del Sur: primera etapa de trabajo hacia una nueva propuesta cronoestratigráfica. *Asociación Geológica Argentina, Serie D, Publicación Especial*, *11*, 9-65.

Bahlburg, H., & Dobrzinski, N. (2011). A review of the Chemical Index of Alteration (CIA) and its application to the study of Neoproterozoic glacial deposits and climate transitions. *Geological Society, London, Memoirs*, *36*(1), 81-92.

Benn, D., & Evans, D. J. (2014). *Glaciers and glaciation*. Routledge.

Bonorino, G. G. (1991). Late Paleozoic orogeny in the northwestern Gondwana continental margin, western Argentina and Chile. Journal of South American Earth Sciences, 4(1-2), 131-144.

Bradshaw, J. D., Vaughan, A. P., Millar, I. L., Flowerdew, M. J., Trouw, R. A., Fanning, C. M., & Whitehouse, M. J. (2012). Permo-Carboniferous conglomerates in the Trinity Peninsula Group at View Point, Antarctic Peninsula: sedimentology, geochronology and isotope evidence for provenance and tectonic setting in Gondwana. Geological Magazine, 149(4), 626-644.

Byers, H., McHenry, L.J., and Grundl, T.J. (2016) Forty-nine major and trace element concentrations measured in Soil Reference Materials NIST SRM 2586, 2587, 2709a, 2710a and 2711a using ICP-MS and Wavelength Dispersive-XRF. Geostandards and Geoanalytical Research, 40, 433–445.

Caputo, M. V., & Crowell, J. C. (1985). Migration of glacial centers across Gondwana during Paleozoic Era. Geological Society of America Bulletin, 96(8), 1020-1036.

Caputo, M. V., de Melo, J. H. G., Streel, M., Isbell, J. L., & Fielding, C. R. (2008). Late Devonian and early Carboniferous glacial records of South America. *Geological Society of America Special Papers*, *441*, 161-173.

Cardozo, N., & Allmendinger, R. W. (2013). Spherical projections with OSXStereonet. *Computers & Geosciences*, *51*, 193-205.

Carto, S.L., and Eyles, N., 2012, Identifying glacial influences on sedimentation in tectonically-active, mass flow dominated arc basins with reference to the Neoproterozoic Gaskiers glaciation (c. 580 Ma) of the Avalonian-Cadomian orogenic belt: Sedimentary Geology, v. 261-262, p. 1-14.

Ciccioli, Patricia & Limarino, Carlos & Taboada, Arturo & Isbell, John & Gulbranson, Erik. (2018). PETROLOGÍA Y MODAS DETRÍTICAS DE LAS SEDIMENTITAS NEOPALEOZOICAS DE LA PATAGONIA EXTRAANDINA, CHUBUT.

Clifton, H. E., Posamentier, H. W., & Walker, R. G. (2006). Facies models revisited. *SEPM Special Publication*, *84*, 293-337.

Condie, K. C. (1993). Chemical composition and evolution of the upper continental crust: contrasting results from surface samples and shales. *Chemical geology*, *104*(1-4), 1-37.

Crowell, J. C., & Frakes, L. A. (1970). Phanerozoic glaciation and the causes of ice ages. American Journal of Science, 268(3), 193-224.

Crowell, J. T., & Frakes, L. A. (1975). The late Paleozoic glaciation. In *Gondwana geology* (Vol. 3, pp. 313-331). Aust. Natl. Univ. Press Canberra.

Crowell, J. C. (1983). Ice ages recorded on Gondwanan continents. South African Journal of Geology, 86(3), 237-262.

Crowell, J. C. (1999). *Pre-Mesozoic ice ages: their bearing on understanding the climate system* (Vol. 192). Geological Society of America.

Cuneo, R. (1991). La tafoflora de la Formacion Mojon de Hierro (Grupo Tepuel) en la localidad Arroyo Garrido, Paleozoico Superior, Provincia de Chubut. *Ameghiniana*, *27*, 225-238.

Dalla Salda, L., Cingolani, C., & Varela, R. (1990). The origin of Patagonia. Comunicaciones, Una revista de geología andina, 41, 55-61.

DeConto, R. M., & Pollard, D. (2003). Rapid Cenozoic glaciation of Antarctica induced by declining atmospheric CO 2. *Nature*, *421*(6920), 245.

Ding, H., Ma, D., Yao, C., Lin, Q., & Jing, L. (2016). Implication of the chemical index of alteration as a paleoclimatic perturbation indicator: an example from the lower Neoproterozoic strata of Aksu, Xinjiang, NW China. *Geosciences Journal*, *20*(1), 13-26.

Dowdeswell, J.A., Whittington, R.J., and Marienfeld, P., 1994, The origin of massive diamicton facies by iceberg rafting and scouring, Scoresby Sund, East Greenland: Sedimentology, v. 41, p. 21-35.

Einsele, G. (2013). *Sedimentary basins: evolution, facies, and sediment budget*. Springer Science & Business Media.

Eyles, N., Eyles, C. H., & Miall, A. D. (1983). Lithofacies types and vertical profile models; an alternative approach to the description and environmental interpretation of glacial diamict and diamictite sequences. *Sedimentology*, *30*(3), 393-410.

Eyles, N., Bonorino, G. G., França, A. B., Eyles, C. H., & Paulsen, O. L. (1995). Hydrocarbon-bearing late Paleozoic glaciated basins of southern and central South America.

Fedo, C. M., Wayne Nesbitt, H., & Young, G. M. (1995). Unraveling the effects of potassium metasomatism in sedimentary rocks and paleosols, with implications for paleoweathering conditions and provenance. *Geology*, *23*(10), 921-924.

Fielding, C. R., Frank, T. D., & Isbell, J. L. (2008). The late Paleozoic ice age—a review of current understanding and synthesis of global climate patterns. Geological Society of America Special Papers, 441, 343-354.

Fielding, C. R., Frank, T. D., Birgenheier, L. P., Rygel, M. C., Jones, A. T., and Roberts, J. (2008b). Stratigraphic imprint of the late Palaeozoic ice age in eastern Australia: a record of alternating glacial and nonglacial climate regime. Journal of the Geological Society, London, 165, 129-140.

Folk, R. L. (1954). The distinction between grain size and mineral composition in sedimentary-rock nomenclature. *The Journal of Geology*, *62*(4), 344-359.

Frakes, L. A., Amos, A. J., & Crowell, J. C. (1969). Origin and stratigraphy of Late Paleozoic diamictites in Argentina and Bolivia. In Symposium Gondwana Stratigraphy, IUGS-Unesco(Vol. 2, pp. 821-843).

Freytes, E. "Informe geológico preliminar sobre la Sierra de Tepuel (Deptos. Languiñeo y Tehuelches, prov. de Chubut). Informe YPF, Buenos Aires, Inédito." Links (1971).

Freytes, E. "Informe parcil sobre los trabajos realizados en la zona Ch PGR-7 (Sierra de Tepuel, Chubut). YPF (Inf. Inedito)." Buenos Aires (1970).

Galloway, W. E. (1989). Genetic stratigraphic sequences in basin analysis I: architecture and genesis of flooding-surface bounded depositional units. AAPG bulletin, 73(2), 125-142.

Gamundi, O. R. L. (1987). Depositional models for the glaciomarine sequences of Andean Late Paleozoic basins of Argentina. Sedimentary Geology, 52(1-2), 109-126.

Gamundi, O. R. L. (1989). Postglacial transgressions in Late Paleozoic basins of western Argentina: a record of glacioeustatic sea level rise. *Palaeogeography, Palaeoclimatology, Palaeoecology*, *71*(3-4), 257-270.

Gastaldo, R. A., DiMichele, W. A., & Pfefferkorn, H. W. (1996). Out of the icehouse into the greenhouse: a late Paleozoic analogue for modern global vegetational change. Gsa today.

Glasser, N. F., Hambrey, M. J., Etienne, J. L., Jansson, P., & Pettersson, R. (2003). The origin and significance of debris-charged ridges at the surface of Storglaciären, northern Sweden. *Geografiska Annaler: Series A, Physical Geography*, *85*(2), 127-147.

Goldberg, Karin. *The paleoclimatic evolution of the Permian in the Paraná Basin in southern Brazil*. Diss. University of Chicago, Department of the Geophysical Sciences, 2001.

Goldberg, Karin, and Munir Humayun. "The applicability of the Chemical Index of Alteration as a paleoclimatic indicator: An example from the Permian of the Paraná Basin, Brazil." *Palaeogeography, Palaeoclimatology, Palaeoecology* 293.1-2 (2010): 175-183.

González-Bonorino, G. (1992). Carboniferous glaciation in Gondwana. Evidence for grounded marine ice and continental glaciation in southwestern Argentina. Palaeogeography, Palaeoclimatology, Palaeoecology, 91(3-4), 363-375.

Griffin, J. J., Windom, H., & Goldberg, E. D. (1968, August). The distribution of clay minerals in the world ocean. In *Deep Sea Research and Oceanographic Abstracts* (Vol. 15, No. 4, pp. 433-459). Elsevier.

Griffis, N.P., Mundil, R., Montañez, I.P., Isbell, J., Fedorchuk, N., Vesely, F., Iannuzzi, R. and Yin, Q.Z., 2018. A new stratigraphic framework built on U-Pb single-zircon TIMS ages and implications for the timing of the penultimate icehouse (Paraná Basin, Brazil). GSA Bulletin, 130(5-6), pp.848-858.

Hambrey, M. J., & Glasser, N. F. (2012). Discriminating glacier thermal and dynamic regimes in the sedimentary record. *Sedimentary Geology*, *251*, 1-33.

Hampton, M. A. (1972). The role of subaqueous debris flow in generating turbidity currents. *Journal of Sedimentary Research*, *42*(4).

Hand, S. J. (1993). Palaeogeography of Tasmania's Permo-Carboniferous glacigenic sediments. *Gondwana Eight: Assembly, Evolution and Dispersal*, 459-469.

Harnois, L. (1988). The CIW index: a new chemical index of weathering. *Sedimentary geology*, *55*, 319-322.

Hathaway, J. C. (1972). Regional clay mineral facies in estuaries and continental margin of the United States East Coast. In *Environmental framework of coastal plain estuaries* (Vol. 133, pp. 293-316). Boulder Colorado.

Haughton, P. D. W., Barker, S. P., and McCaffrey, W. D., 2003, 'Linked' debrites in sand-rich turbidite systems-origin and significance: Sedimentology, v. 50, p. 459-482.

Haughton, P.D.W., Davis, C., McCaffrey, W. and Barker, S., 2009, Hybrid sediment gravity flow deposits – classification, origin and significance: Marine Petroleum Geology, v. 26, p. 1900–1918.

Harrington, HJ, & Leanza, AF (1952). The classification of the "Olenidae" y de los Ceratopygidae "(Trilobita). Revista de la Asociación Geológica Argentina , 7 (3), 190-205.

Harrington, H. J. (1962). Paleogeographic development of South America. AAPG Bulletin, 46(10), 1773-1814.

Heckel, P. H. (2008). Pennsylvanian cyclothems in Midcontinent North America as far-field effects of waxing and waning of Gondwana ice sheets. Resolving the Late Paleozoic Ice Age in Time and Space; Fielding, CR, Frank, TD, Isbell, JL, Eds, 275-290.

Heckel, P. H. (1994). Evaluation of evidence for glacio-eustatic control over marine Pennsylvanian cyclothems in North America and consideration of possible tectonic effects. Tectonic and Eustatic Controls on Sedimentary Cycles: SEPM, Concepts in Sedimentology and Paleontology, 4, 65-87.

Henry, Lindsey C., et al. "Mid-Carboniferous deglaciation of the Protoprecordillera, Argentina recorded in the Agua de Jagüel palaeovalley." *Palaeogeography, Palaeoclimatology, Palaeoecology* 298.1-2 (2010): 112-129.

Horton, D. E., & Poulsen, C. J. (2009). Paradox of late Paleozoic glacioeustasy. Geology, 37(8), 715-718.

Ingersoll, R. V. (1988). Tectonics of sedimentary basins. *Geological Society of America Bulletin*, *100*(11), 1704-1719.

Isaacson, P. E., Diaz-Martinez, E., Grader, G. W., Kalvoda, J., Babek, O., & Devuyst, F. X. (2008). Late Devonian–earliest Mississippian glaciation in Gondwanaland and its biogeographic consequences. *Palaeogeography, Palaeoclimatology, Palaeoecology*, *268*(3-4), 126-142.

Isbell, J.L., P.A. Lenaker, R.A. Askin, M.F. Miller, L.E. Babcock. Reevaluation of the timing and extent of late Palaeozoic glaciation in Gondwana: role of the Transantarctic Mountains. Geology, 31 (2003a), pp. 977-980

Isbell, J.L., M.F. Miller, K.L. Wolfe, P.A. Lenaker. Timing of late Paleozoic glaciation in Gondwana: was glaciation responsible for the development of northern hemisphere cyclothems? M.A. Chan, A.W. Archer (Eds.), Extreme Depositional Environments: Mega End Members in Geologic Time, Geological Society of America, Special Publication, 370(2003b), pp. 5-24

Isbell, J. L., Koch, Z. J., Szablewski, G. M., & Lenaker, P. A. (2008). Permian glacigenic deposits in the Transantarctic Mountains, Antarctica. *Resolving the late Paleozoic ice age in time and space: Geological Society of America Special Paper*, *441*, 59-70.

Isbell, J.L., (2010). Environmental and paleogeographic implications of glaciotectonic deformation of glaciomarine deposits within Permian strata of the Metschel Tillite, southern Victoria Land, Antarctica. O.R. López-Gamundí, L.A. Buatois (Eds.), Late Paleozoic Glacial Events and Postglacial Transgressions in Gondwana, Geological Society of America, Special Publication, 468(2010), pp. 81-100

Isbell, J. L., Henry, L. C., Gulbranson, E. L., Limarino, C. O., Fraiser, M. L., Koch, Z. J., ... & Dineen, A. A. (2012). Glacial paradoxes during the late Paleozoic ice age: evaluating the equilibrium line altitude as a control on glaciation. Gondwana research, 22(1), 1-19.

Jones, B., & Manning, D. A. (1994). Comparison of geochemical indices used for the interpretation of palaeoredox conditions in ancient mudstones. Chemical Geology, 111(1-4), 111-129.

Krissek, L. A., & Kyle, P. R. (2000). Geochemical indicators of weathering, Cenozoic palaeoclimates, and provenance from fine-grained sediments in CRP-2/2A, Victoria Land Basin, Antarctica. *Terra Antartica*, *7*(4), 589-597.

Lawver, L.A., Dalziel, I.W.D., Norton, I.O., and Gahagan, L.M., 2011, The Plates 2011 Atlas of Plate Reconstructions (500 Ma to Present Day), Plates Progress Report No. 345-0811, University of Texas Technical Report No. 198, 189 pp.

Lee, H. J., Locat, J., Desgagnes, P., Parsons, J. D., McAdoo, B. G., Orange, D. L., Puig, 75 P., Wong, F. L., Dartnell, P., and Boulanger, E., 2007, Submarine mass movements on continental margins: Special Publication of the International Association of Sedimentologists, v. 37, p. 213-274.

Limarino, C. O., Césari, S. N., Spalletti, L. A., Taboada, A. C., Isbell, J. L., Geuna, S., & Gulbranson, E. L. (2014). A paleoclimatic review of southern South America during the late Paleozoic: a record from icehouse to extreme greenhouse conditions. Gondwana Research, 25(4), 1396-1421.

Limarino, C. O., & Spalletti, L. A. (2006). Paleogeography of the upper Paleozoic basins of southern South America: An overview. Journal of South American Earth Sciences, 22(3-4), 134-155.

Lopez Gamundi, O. (1994). Southern South America. Permian-Triassic Pangean basins and fold belts along the Panthalassan margin of western Gondwanaland.

López-Gamundí, O. R. (1997). Glacial-postglacial transition in the Late Paleozoic basins of southern South America. Late Glacial and Postglacial Environmental Changes-Quaternary, Carboniferous-Permian, and Proterozoic (Martini, IP, 147-168.

López-Gamundí, O. R. (2010). Transgressions related to the demise of the Late Paleozoic Ice Age: Their sequence stratigraphic context. *Late Paleozoic glacial events and postglacial transgressions in Gondwana*, *468*, 1-35.

Martinsen, O. J. (1989). Styles of soft-sediment deformation on a Namurian (Carboniferous) delta slope, Western Irish Namurian Basin, Ireland. Geological Society, London, Special Publications, 41(1), 167-177.

Martinsen, O. (1994). Mass movements. In The geological deformation of sediments (pp. 127-165). Springer, Dordrecht.

McHenry, L.J. (2009) Element mobility during zeolitic and argillic alteration of volcanic ash in a closed-basin lacustrine environment: Case study Olduvai Gorge, Tanzania. Chemical Geology, 265, 540–552.

Miller, W., de Wit, M. J., Linol, B., & Armstrong, R. (2016). New Structural Data and U/Pb Dates from the Gamtoos Complex and Lowermost Cape Supergroup of the Eastern Cape Fold Belt, in Support of a Southward Paleo-Subduction Polarity. In Origin and Evolution of the Cape Mountains and Karoo Basin (pp. 35-44). Springer, Cham.

Miall, A. D. (2010). *The geology of stratigraphic sequences*. Springer Science & Business Media.

Moncrieff, A. C. M. (1989). Classification of poorly-sorted sedimentary rocks. *Sedimentary Geology*, *65*(1-2), 191-194.

Montañez, I. P., & Poulsen, C. J. (2013). The Late Paleozoic ice age: an evolving paradigm. Annual Review of Earth and Planetary Sciences, 41, 629-656.

Mory, A. J., Redfern, J., & Martin, J. R. (2008). A review of Permian–Carboniferous glacial deposits in Western Australia. *Geological Society of America Special Papers*, *441*, 29-40.

Mulder, T., & Alexander, J. (2001). The physical character of subaqueous sedimentary density flows and their deposits. *Sedimentology*, *48*(2), 269-299.

Nesbitt, H. W., & Young, G. M. (1982). Early Proterozoic climates and plate motions inferred from major element chemistry of lutites. *Nature*, *299*(5885), 715.

Nesbitt, H. W., & Young, G. M. (1989). Formation and diagenesis of weathering profiles. *The Journal of Geology*, *97*(2), 129-147.

Nichols, G. (2009). *Sedimentology and stratigraphy*. John Wiley & Sons.

Pagani, M. A., & Taboada, A. C. (2010). The marine upper Palaeozoic in Patagonia (Tepuel–Genoa Basin, Chubut Province, Argentina): 85 years of work and future prospects. *Palaeogeography, Palaeoclimatology, Palaeoecology*, *298*(1-2), 130-151.

Page, R. F. N., Limarino, C. O., López Gamundi, O., & Page, S. (1984). Estratigrafía del Grupo Tepuel en su perfil tipo y en la región de El Molle, provincia de Chubut. In *San Carlos de Bariloche (1984), 9º Congreso Geológico Argentino* (Vol. 1, pp. 619-632).

Pankhurst, R. J., Rapela, C. W., Fanning, C. M., & Márquez, M. (2006). Gondwanide continental collision and the origin of Patagonia. Earth-Science Reviews, 76(3-4), 235-257.

Passchier, S., Bohaty, S. M., Jiménez-Espejo, F., Pross, J., Röhl, U., Flierdt, T., ... & Brinkhuis, H. (2013). Early Eocene to middle Miocene cooling and aridification of East Antarctica. *Geochemistry, Geophysics, Geosystems*, *14*(5), 1399-1410.

Pickering, K. T., & Hiscott, R. N. (2016). Deep Marine Systems. Processes, Deposits, Environments, Tectonics and Sedimentation, 657 pp., AGU and Wiley.

Posamentier, H. W., Martinsen, O. J., & Shipp, R. C. (2011). The character and genesis of submarine mass-transport deposits: insights from outcrop and 3D seismic data. Mass-transport deposits in deepwater settings. Tulsa: SEPM, Special Publication, 96, 7-38.

Posamentier, H.W., and Walker, R.G., 2006, Deep-water turbidites and submarine fans, in Posamentier, H. W., and Walker, R. G., eds., Facies models revisited: Tulsa, SEPM Special Publication 84, p. 397-520.

Powell, R., & Domack, G. W. (2002). Modern glaciomarine environments. In *Modern and past glacial environments* (pp. 361-389). Butterworth-Heinemann.

Ramos, V. A., Jordan, T. E., Allmendinger, R. W., Mpodozis, C., Kay, S. M., Cortés, J. M., & Palma, M. (1986). Paleozoic terranes of the central Argentine-Chilean Andes. Tectonics, 5(6), 855-880.

Ramos, V. A. (1988). Late Proterozoic-early Paleozoic of South America-a collisional history. Episodes, 11(3), 168-174.

Ramos, V. A. (2008). Patagonia: a Paleozoic continent adrift?. Journal of South American Earth Sciences, 26(3), 235-251.

Ramos, V. A., & Naipauer, M. (2014). Patagonia: where does it come from?.

Rapelini, A., Fantin, M., Sanchez, B., Rapela, C., Pazos, P., & Tarling, D. Paleo magnetic investigations in late Proterozoic rocks from the Rio de la Plata craton: a progress report.

Riccardi, A. C., & Sabattini, N. (1975). Cephalopoda from the Carboniferous of Argentina. *Palaeontology*, *18*(1), 117-136.

Rocha-Campos, A. C., dos Santos, P. R., Canuto, J. R., & Fielding, C. R. (2008). Late paleozoic glacial deposits of Brazil: Paraná Basin. *Resolving the late Paleozoic ice age in time and space: Geological Society of America Special Paper*, *441*, 97-114.

Rygel, M. C., Fielding, C. R., Frank, T. D., & Birgenheier, L. P. (2008). The magnitude of Late Paleozoic glacioeustatic fluctuations: a synthesis. Journal of Sedimentary Research, 78(8), 500-511.

Sabattini, N., Riccardi, A. C., & Pagani, M. A. (2006). Cisuralian cephalopods from Patagonia, Argentina. *Journal of Paleontology*, *80*(6), 1142-1151.

Scheffler, K., Hoernes, S., & Schwark, L. (2003). Global changes during Carboniferous–Permian glaciation of Gondwana: Linking polar and equatorial climate evolution by geochemical proxies. *Geology*, *31*(7), 605-608.

Scheffler, K., Buehmann, D., & Schwark, L. (2006). Analysis of late Palaeozoic glacial to postglacial sedimentary successions in South Africa by geochemical proxies–Response to climate evolution and sedimentary environment. *Palaeogeography, Palaeoclimatology, Palaeoecology*, *240*(1-2), 184-203.

Scotese, R. C., & Barrett, S. F. (1990). Gondwana's movement over the South Pole during the Palaeozoic: evidence from lithological indicators of climate. *Geological Society, London, Memoirs*, *12*(1), 75-85.

Scotese, C. R. (1997). *Paleogeographic Atlas: PALEOMAP progress report 90-0497*. PALEOMAP Project, University of Texas.

Scotese, C. R. (2014). Atlas of Permo-Carboniferous Paleogeographic Maps.

Scotese, C. R. (2014). Atlas of Plate Tectonic Reconstructions (Mollweide Projection).

Shanmugam, G. (1996). High-density turbidity currents; are they sandy debris flows. *Journal of sedimentary research*, *66*(1), 2-10.

Shanmugam, G., Lehtonen, L. R., Straume, T., Syvertsen, S.E., Hodgkinson, R. J., and Skibeli, M., 1994, Slump and debris-flow dominated upper slope facies in the Cretaceous of the Norwegian and northern North Seas (61-67 degrees N): implications for sand distribution: American Association of Petroleum Geologists Bulletin, v. 78, no. 6, p. 910-937.

Shanmugam, G., 2006, Deep-water processes and facies models: implications for

sandstone petroleum reservoirs, Amsterdam, Elsevier, 475 p.

Shipp, R. C., Weimer, P. A. U. L., & Posamentier, H. W. (2011). Mass-transport deposits in deepwater settings: an introduction. Mass-Transport Deposits In Deepwater Settings: Society for Sedimentary Geology (SEPM) Special Publication 96, 3-6.

Sohn, Y. K., Choe, M. Y., & Jo, H. R. (2002). Transition from debris flow to hyperconcentrated flow in a submarine channel (the Cretaceous Cerro Toro Formation, southern Chile). Terra Nova, 14(5), 405-415.

Soreghan, G. S. (2004). Deja-vu all over again: Deep time (climate) is here to stay. Palaios, 19(1), 1-2.

Soreghan, G. S., & Dickinson, W. R. (1994). Generic types of stratigraphic cycles controlled by eustasy. Geology, 22(8), 759-761.

Stow, D. A. V. (1994). Deep sea processes of sediment transport and deposition. Sediment transport and depositional processes., 257-291.

Strachan, L. J., 2002, Slump-initiated and controlled syndepositional sandstone remobilization: an example from the Namurian of County Clare, Ireland: Sedimentology, v. 49, no. 1, p. 25-41.

Strachan, L. J., 2008, Flow transformations in slumps: a case study from the Waitemata Basin, New Zealand: Sedimentology, v. 55, p. 1311-1332.

Sumner, E.J., Talling, P.J., Amy, L.A., Wynn, R.B., Stevenson, C.J., and Frenz, M., 78. (2012), Facies architecture of individual basin-plain turbidites: Comparison with existing models and implications for flow processes: Sedimentology, v. 59, p. 1850-1887.

Suero, T. (1958), "Datos geológicos sobre el Paleozoico superior en la zona de Nueva Lubecka y alrededores (Chubut extraandino, province de Chubut)." Revista Museo de La Plata (NS) 5 : 1 - 28.

Suero, T. (1948). *Descubrimiento de Paleozoico superior en la zona extraandina de Chubut*. R. Canals.

Survis, S. R. (2015). Sedimentology and Stratigraphy of High-latitude, Glacigenic Deposits from the Late Paleozoic Ice Age in the Tepuel-Genoa Basin, Patagonia, Argentina.

Taboada, A. C., M. A. Pagani, and P. Puerta. (2009) "An approach to the Carboniferous–Early Permian stratigraphy, paleontology, paleogeography and paleoclimatology of the Calingasta-Uspallata Subbasin (western Argentina) and Tepuel-Genoa Basin (Patagonia), Argentina: a fieldguide." Permophiles 53 : 11-48.

Taboada, A. C. (2010). Mississippian–Early Permian brachiopods from western Argentina: tools for middle-to high-latitude correlation, paleobiogeographic and paleoclimatic reconstruction. *Palaeogeography, Palaeoclimatology, Palaeoecology*, *298*(1-2), 152-173.

Talling, P. J., Amy, L. A., Wynn, R. B., Peakall, J. and Robinson, M., 2004, Beds comprising debrite sandwiched within co-genetic turbidite: origin and widespread occurrence in distal depositional environments: Sedimentology, v. 51, p. 163–194.

Talling, P. J., Amy, L. A., and Wynn, R. B., 2007, New insights into the evolution of large volume turbidity currents; comparison of turbidite shape and previous modelling results: Sedimentology, v. 54, p. 737-769.

Talling, P. J., Masson, D. G., Sumner, E. J., & Malgesini, G. (2012). Subaqueous sediment density flows: Depositional processes and deposit types. *Sedimentology*, *59*(7), 1937-2003.

Thomas, G. S., & Connell, R. J. (1985). Iceberg drop, dump, and grounding structures from Pleistocene glacio-lacustrine sediments, Scotland. *Journal of Sedimentary Research*, *55*(2), 243-249.

Veevers, J. J. (1994). Earth's paleoclimate and sedimentary environments. Pangea: Paleoclimate, tectonics, and sedimentation during accretion, zenith, and breakup of a supercontinent, 288, 13.

Veevers, J. T., & Powell, C. M. (1987). Late Paleozoic glacial episodes in Gondwanaland reflected in transgressive-regressive depositional sequences in Euramerica. Geological Society of America Bulletin, 98(4), 475-487.

Veevers, J. J., & Tewari, R. C. (1995). Permian-Carboniferous and Permian-Triassic magmatism in the rift zone bordering the Tethyan margin of southern Pangea. *Geology*, *23*(5), 467-470.

Visser, J. N. J. (1987). The palaeogeography of part of southwestern Gondwana during the Permo-Carboniferous glaciation. *Palaeogeography, Palaeoclimatology, Palaeoecology*, *61*, 205-219.

Visser, J. N. (1997). Deglaciation sequences in the Permo-Carboniferous Karoo and Kalahari basins of southern Africa: a tool in the analysis of cyclic glaciomarine basin fills. *Sedimentology*, *44*(3), 507-521.

Wanless, H. R., & Shepard, F. P. (1936). Sea level and climatic changes related to late Paleozoic cycles. *Bulletin of the Geological Society of America*, *47*(8), 1177-1206.

Young, G. M., & Nesbitt, H. W. (1985). The Gowganda Formation in the southern part of the Huronian outcrop belt, Ontario, Canada: stratigraphy, depositional environments and regional tectonic significance. Precambrian Research, 29(1-3), 265-301.

Ziegler, A.M., Hulver, M.L., and Rowley, D.B., (1997), Permian world topography and climate, in Martini, I.P., ed., Late glacial and post-glacial environmental changes—Quaternary, Carboniferous-Permian and Proterozoic: New York, Oxford University Press, p. 111–146.

https://geomag.nrcan.gc.ca/calc/mdcal-en.php : Magnetic Declination Calculator

APPENDIX A

MOJÓN DE HIERRO FORMATION
ARROYO GARRIDO STRATIGRAPHIC COLUMNS

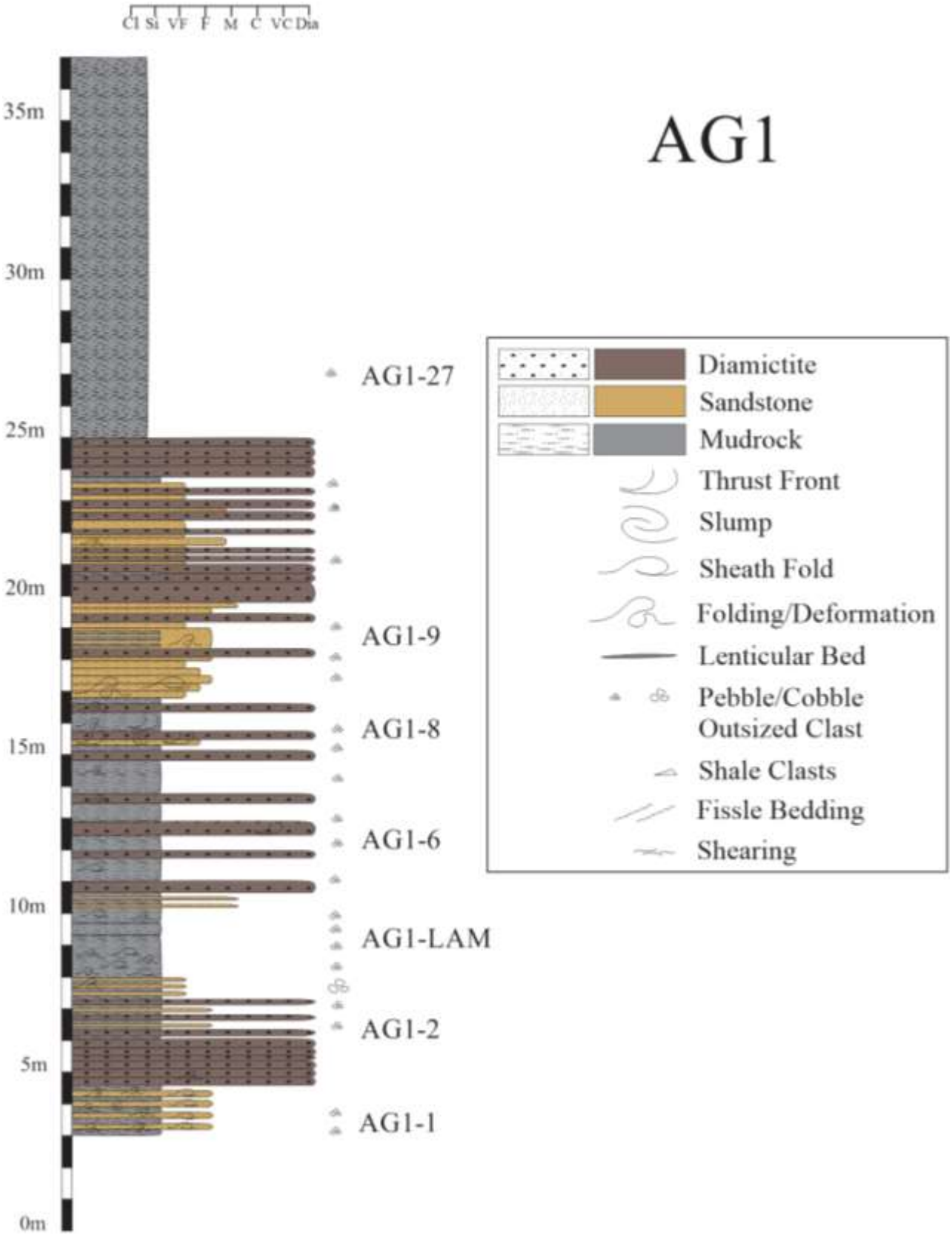
Cl Si VF F M C VC Dia
35m
30m
25m
20m
15m
10m
5m
0m
AG1
AG1-27
AG1-9
AG1-8
AG1-6
AG1-LAM
AG1-2
AG1-1
Diamictite
Sandstone
Mudrock
Thrust Front
Slump
Sheath Fold
Folding/Deformation
Lenticular Bed
Pebble/Cobble
Outsized Clast
Shale Clasts
Fissle Bedding
Shearing

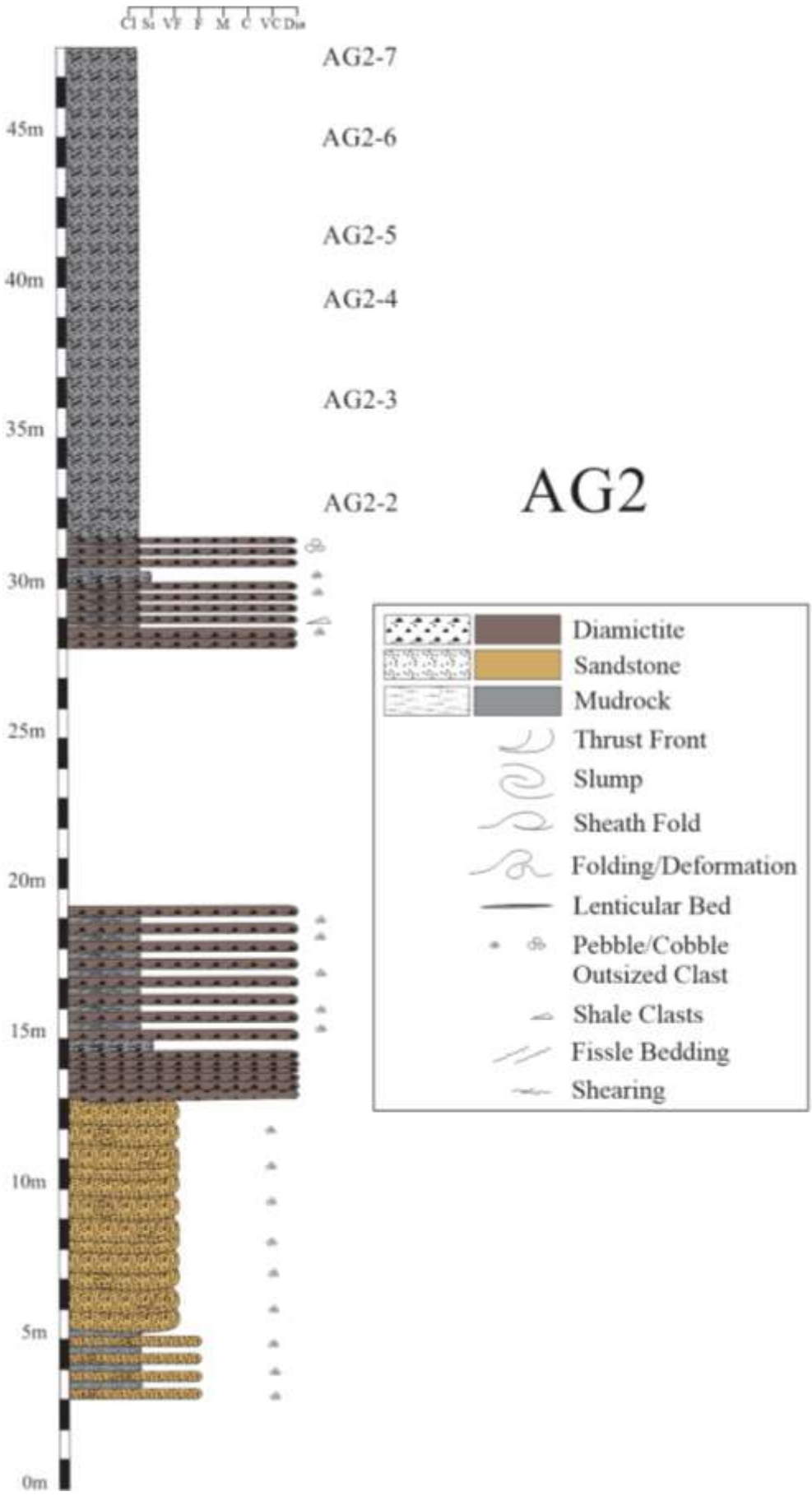
Cl Si VF F M C VC Dia
AG2-7
AG2-6
AG2-5
AG2-4
AG2-3
AG2-2
45m
40m
35m
30m
25m
20m
15m
10m
5m
0m
AG2
Diamictite
Sandstone
Mudrock
Thrust Front
Slump
Sheath Fold
Folding/Deformation
Lenticular Bed
Pebble/Cobble
Outsized Clast
Shale Clasts
Fissle Bedding
Shearing

AG3

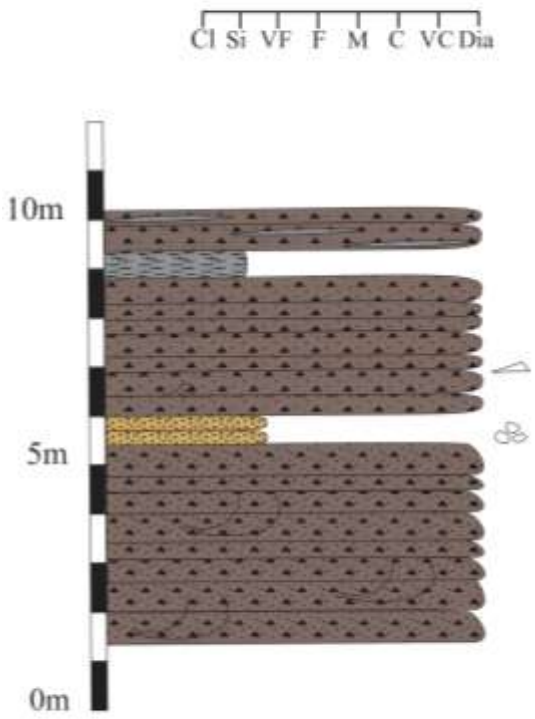
Cl Si VF F M C VC Dia
10m
5m
0m

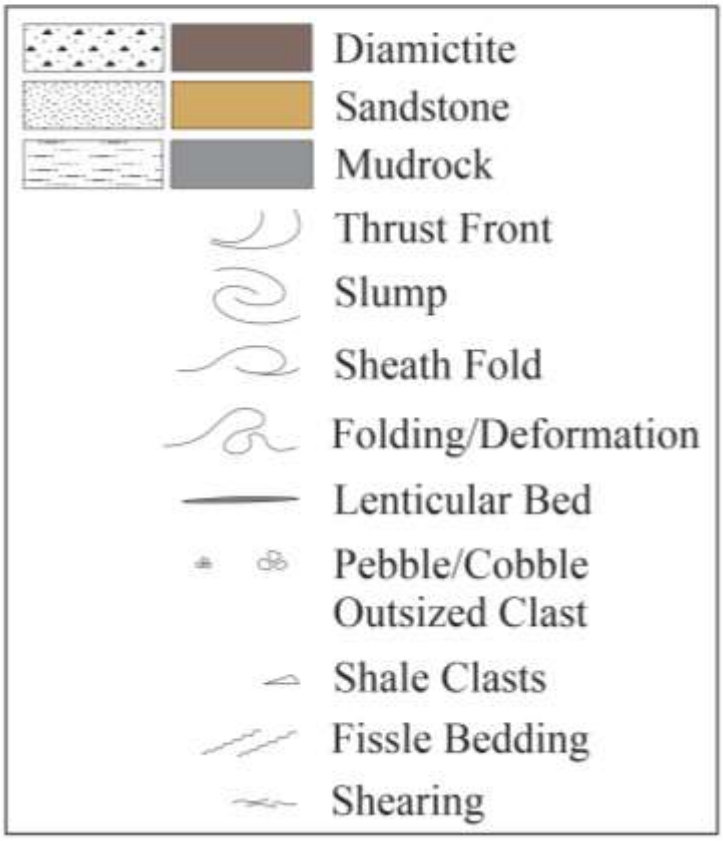
Diamictite
Sandstone
Mudrock
Thrust Front
Slump
Sheath Fold
Folding/Deformation
Lenticular Bed
Pebble/Cobble
Outsized Clast
Shale Clasts
Fissle Bedding
Shearing

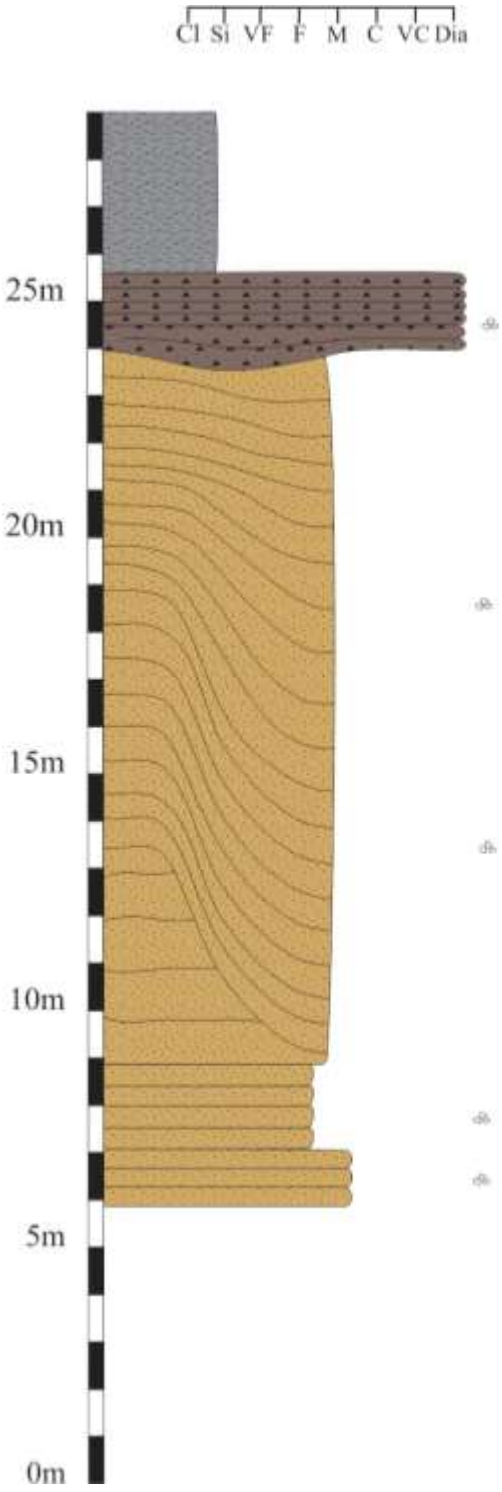
Cl Si VF F M C VC Dia
25m
20m
15m
10m
5m
0m

AG4

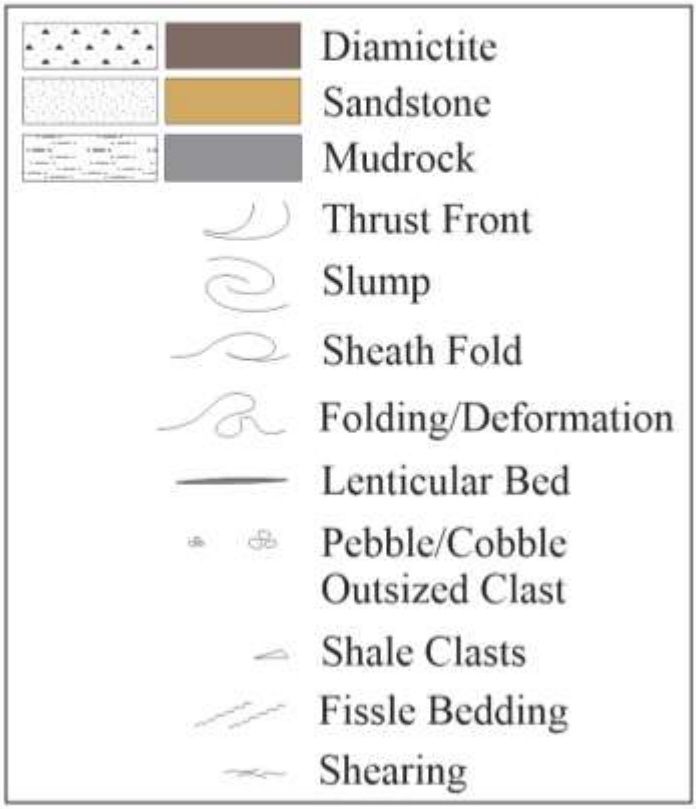
Diamictite
Sandstone
Mudrock
Thrust Front
Slump
Sheath Fold
Folding/Deformation
Lenticular Bed
Pebble/Cobble
Outsized Clast
Shale Clasts
Fissle Bedding
Shearing

AG5

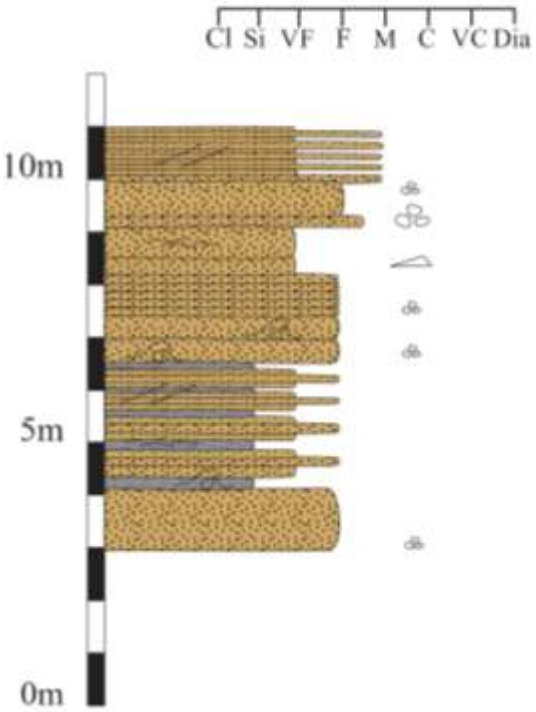
Cl Si VF F M C VC Dia
10m
5m
0m

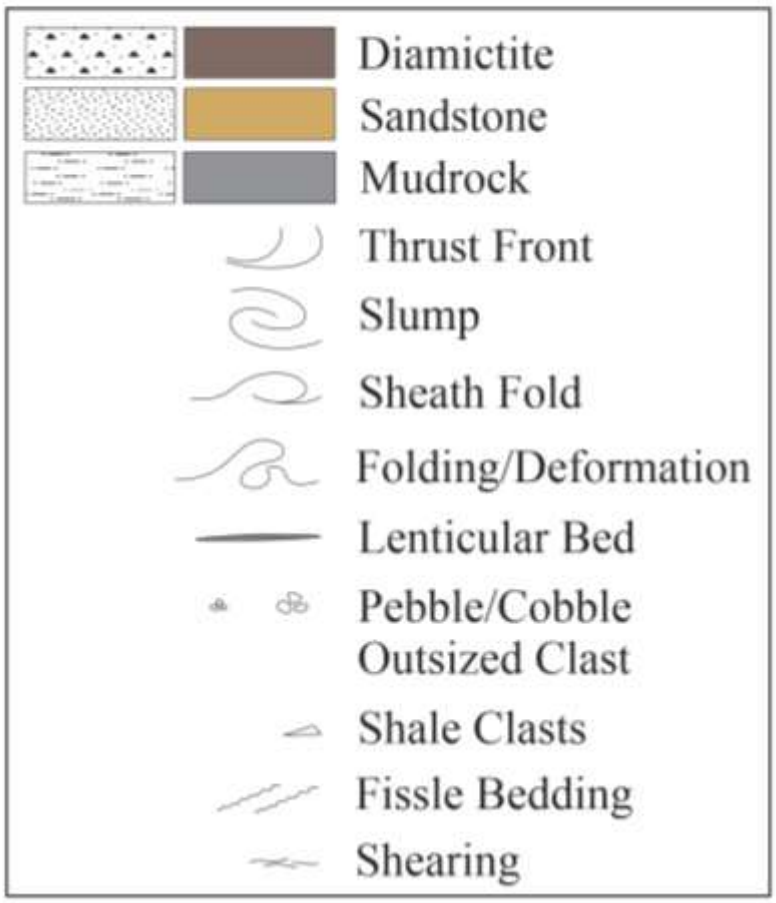
Diamictite
Sandstone
Mudrock
Thrust Front
Slump
Sheath Fold
Folding/Deformation
Lenticular Bed
Pebble/Cobble
Outsized Clast
Shale Clasts
Fissle Bedding
Shearing

APPENDIX B

ARROYO GARRIDO PALEO-FLOW MEASUREMENTS

Thrust Faults/Glide Planes				
Corrected Dip Direction (°)	Corrected Dip Angle (°)	Measured Dip Direction (°)	Measured Dip Angle (°)	Vergence
96	8	85	32	
94	19	80	42	
105	17	95	41	
92	0	80	25	
92	2	80	24	
92	12	80	35	
63	36	35	50	
183	5	170	15	N
138	21	125	43	N
127	39	125	62	N
136	15	125	37	N
152	21	145	35	N
104	64	145	87	
102	66	235	90	SW
98	68	355	88	SW
113	43	120	67	N/NW
129	45	135	67	N/NW
129	32	140	52	N/NW
155	11	155	26	N/NW
109	58	140	80	N/NW
147	16	150	32	N/NW
122	0	115	22	N/NW
138	29	150	47	N/NW
113	4	105	28	
132	13	130	34	
120	41	135	63	

APPENDIX C

X-RAY DIFFRACTION PLOTS

AG1-3

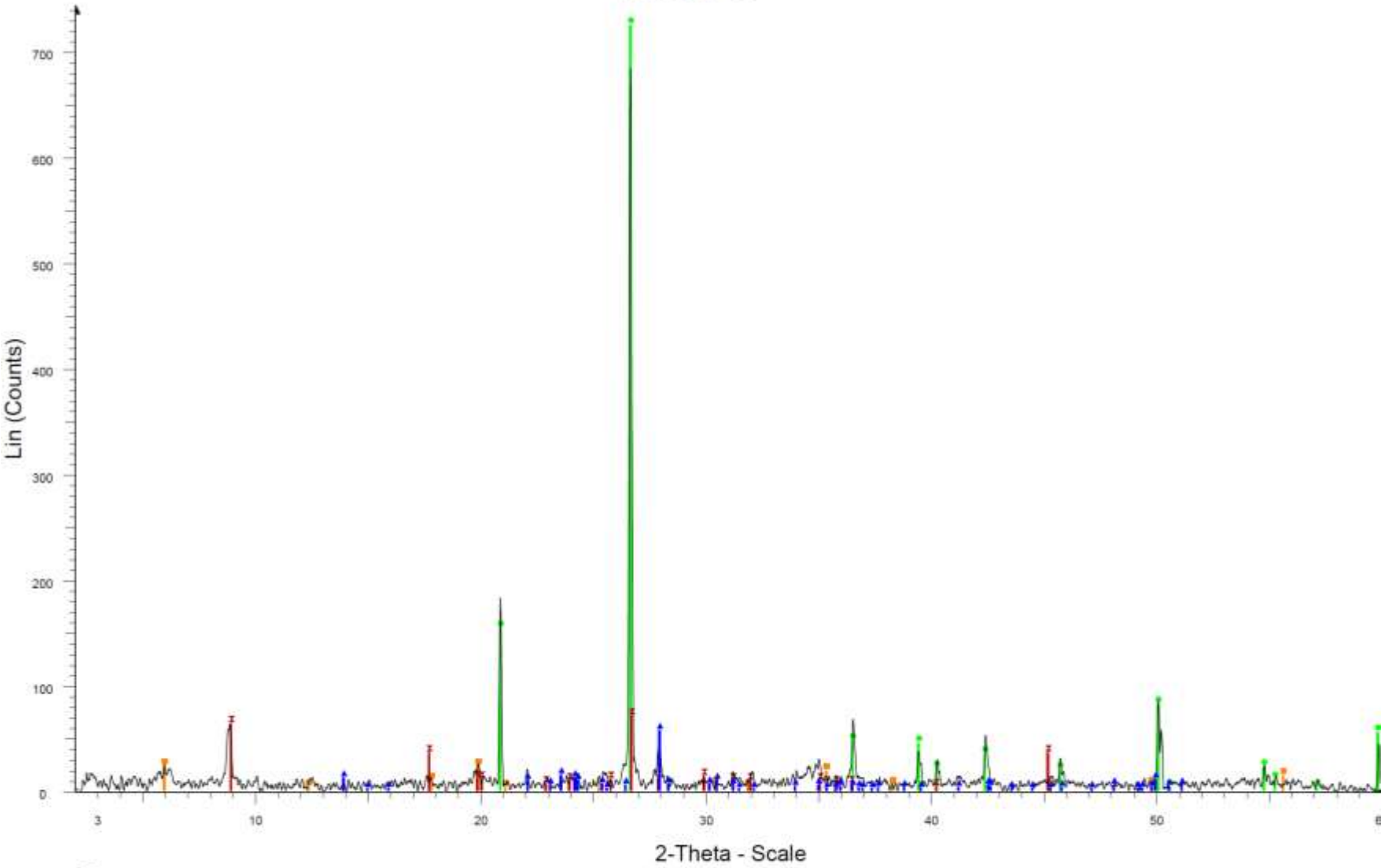

AG1-3 - File: AG1-3.raw - Type: 2Th/Th locked - Start: 2.000 ° - End: 60.000 ° - Step: 0.020 ° - Step time: 1. s - Temp.: 25 °C (Room) - Time Started: 12 s - 2-Theta: 2.000 ° - Theta: 1.000 ° - Chi: 0.00 ° - Phi: 0.00 ° - Operations: Bezier Background 1.000,1.000 | Smooth 0.080 | Import

01-089-8935 (*) - Silicon Oxide - SiO2 - Y: 85.14 % - d x by: 1. - WL: 1.5406 - Hexagonal - a 4.92090 - b 4.92090 - c 5.40910 - alpha 90.000 - beta 90.000 - gamma 120.000 - Primitive - P3221 (154) - 3 - 113.434 - I/I

00-009-0466 (*) - Albite, ordered - NaAlSi3O8 - Y: 6.60 % - d x by: 1. - WL: 1.5406 - Triclinic - a 8.14400 - b 12.78700 - c 7.16000 - alpha 94.260 - beta 116.600 - gamma 87.670 - Base-centered - C-1 (2) - 4 - 664.83

00-003-0014 (D) - Montmorillonite - MgO·Al2O3·5SiO2·xH2O - Y: 2.63 % - d x by: 1. - WL: 1.5406 -

00-026-0911 (I) - Illite-2M1 (NR) - (K,H3O)Al2Si3AlO10(OH)2 - Y: 8.20 % - d x by: 1. - WL: 1.5406 - Monoclinic - a 5.19000 - b 9.00000 - c 20.16000 - alpha 90.000 - beta 95.180 - gamma 90.000 - Base-centered - C2

AG1-27

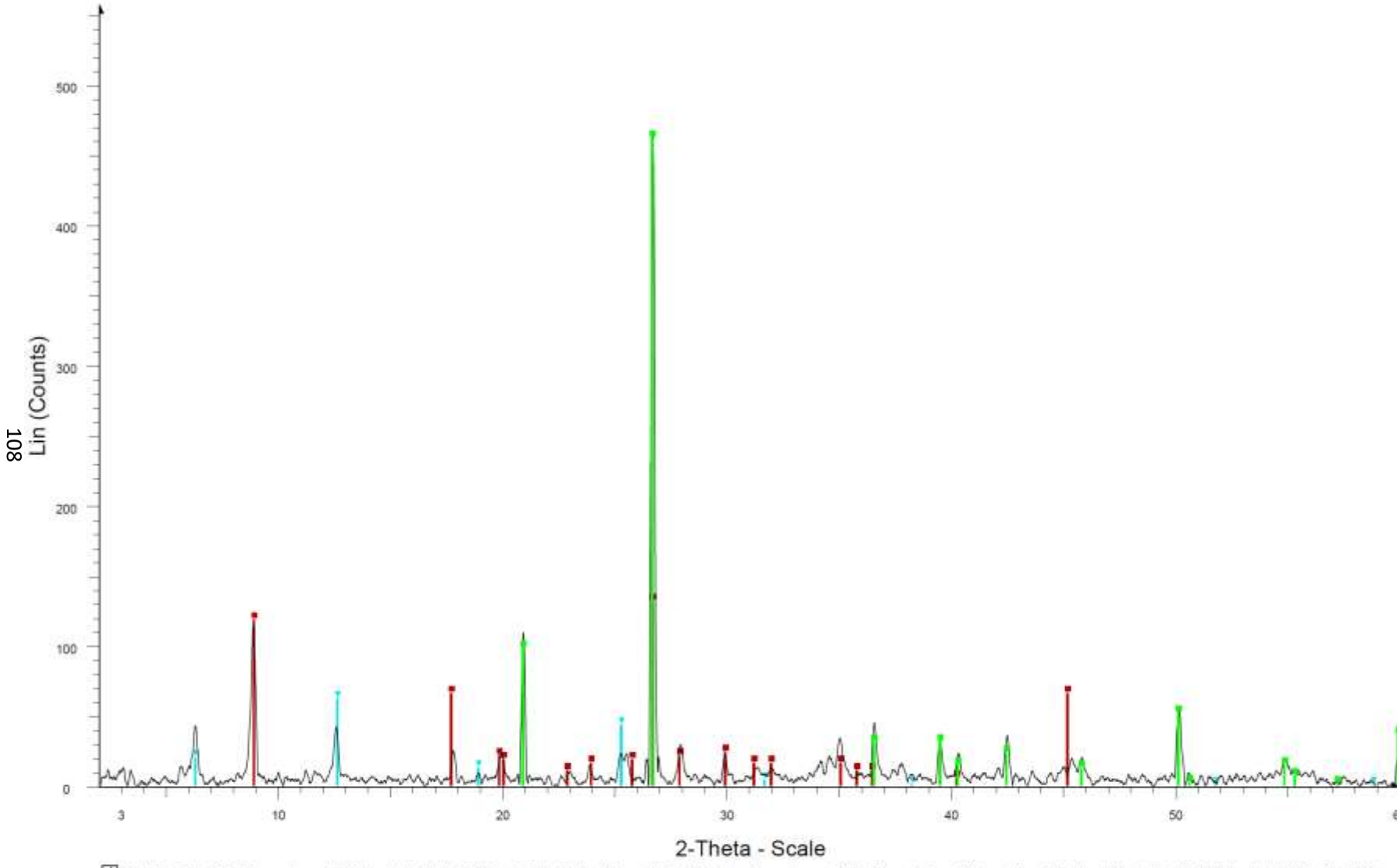

AG1-27 - File: AG1-27.raw - Type: 2Th/Th locked - Start: 2.000 ° - End: 60.000 ° - Step: 0.020 ° - Step time: 1. s - Temp.: 25 °C (Room) - Time Started: 12 s - 2-Theta: 2.000 ° - Theta: 1.000 ° - Chi: 0.00 ° - Phi: 0.00 °
Operations: Bezier Background 1.000,1.000 | Smooth 0.150 | Import
01-089-8934 (*) - Silicon Oxide - SiO2 - Y: 60.17 % - d x by: 1. - WL: 1.5406 - Hexagonal - a 4.91370 - b 4.91370 - c 5.40470 - alpha 90.000 - beta 90.000 - gamma 120.000 - Primitive - P3221 (154) - 3 - 113.011 - I/I
00-052-1044 (I) - Chlorite-serpentine - (Mg,Al)6(Si,Al)4O10(OH)8 - Y: 8.04 % - d x by: 1. - WL: 1.5406 - Hexagonal - a 5.34000 - b 5.34000 - c 14.10900 - alpha 90.000 - beta 90.000 - gamma 120.000 - Primitive - P (
00-026-0911 (I) - Illite-2M1 (NR) - (K,H3O)Al2Si3AlO10(OH)2 - Y: 17.11 % - d x by: 1. - WL: 1.5406 - Monoclinic - a 5.19000 - b 9.00000 - c 20.16000 - alpha 90.000 - beta 95.180 - gamma 90.000 - Base-centered - C

AG2-7

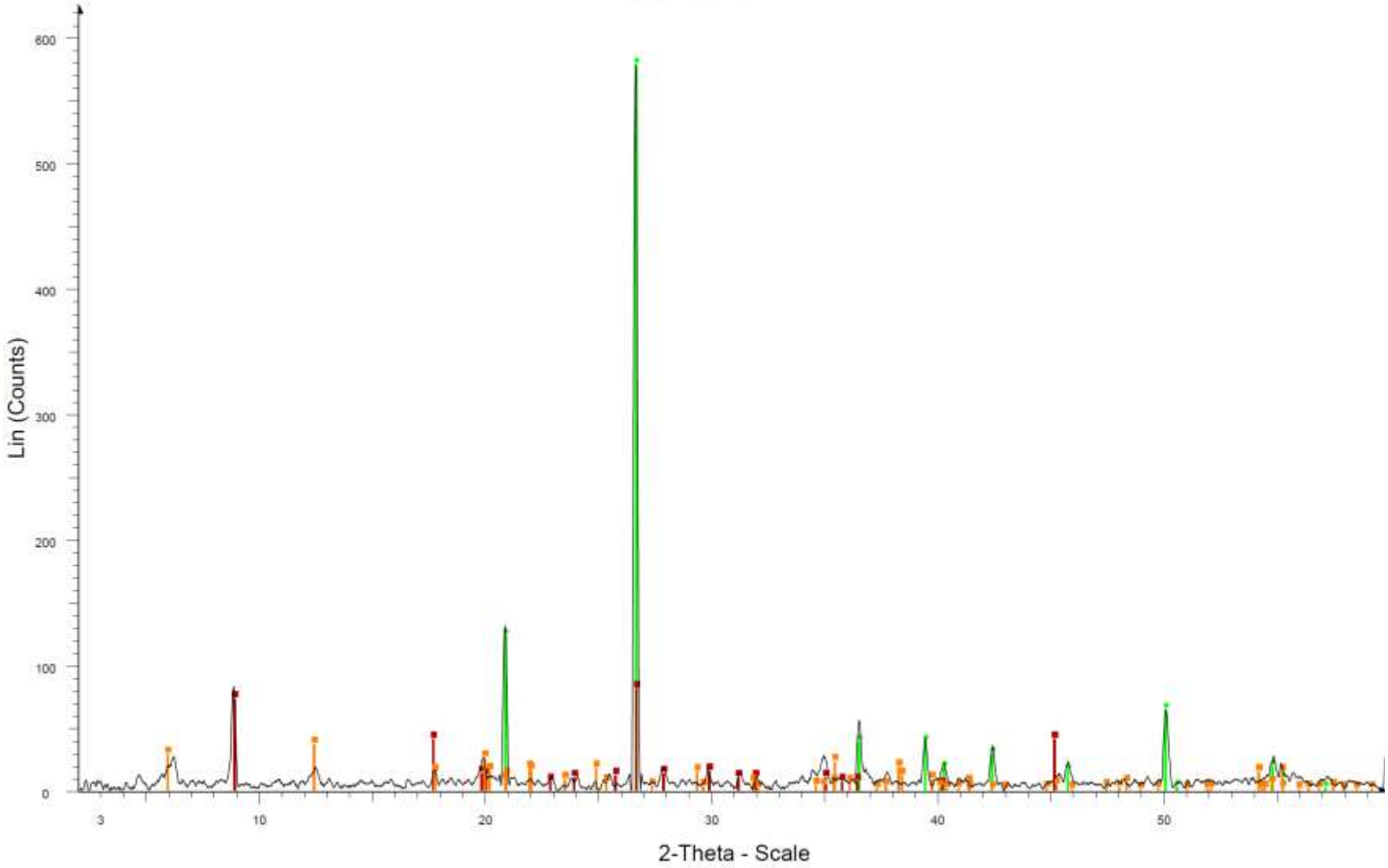

AG2-7 - File: AG2-7.raw - Type: 2Th/Th locked - Start: 2.000 ° - End: 60.000 ° - Step: 0.020 ° - Step time: 1. s - Temp.: 25 °C (Room) - Time Started: 12 s - 2-Theta: 2.000 ° - Theta: 1.000 ° - Chi: 0.00 ° - Phi: 0.00 ° - Operations: Bezier Background 1.000,1.000 | Smooth 0.150 | Import

01-086-1560 (*) - Quartz - SiO2 - Y: 61.26 % - d x by: 1. - WL: 1.5406 - Hexagonal - a 4.91600 - b 4.91600 - c 5.40540 - alpha 90.000 - beta 90.000 - gamma 120.000 - Primitive - P3221 (154) - 3 - 113.131 - I/Ic PDF

00-026-0911 (I) - Illite-2M1 (NR) - (K,H3O)Al2Si3AlO10(OH)2 - Y: 8.53 % - d x by: 1. - WL: 1.5406 - Monoclinic - a 5.19000 - b 9.00000 - c 20.16000 - alpha 90.000 - beta 95.180 - gamma 90.000 - Base-centered - C2

00-002-0014 (D) - Montmorillonite (Clay) - NaMgAlSiO2(OH)H2O - Y: 2.97 % - d x by: 1. - WL: 1.5406 -

01-075-0938 (I) - Kaolinite 2M - Al2Si2O5(OH)4 - Y: 3.82 % - d x by: 1. - WL: 1.5406 - Monoclinic - a 5.14800 - b 8.92000 - c 14.53500 - alpha 90.000 - beta 100.200 - gamma 90.000 - Base-centered - Cc (9) - 4 - 656